INFORMATION TO USERS

This manuscript has been reproduced from the microfilm master. UMI films the text directly from the original or copy submitted. Thus, some thesis and dissertation copies are in typewriter face, while others may be from any type of computer printer.

The quality of this reproduction is dependent upon the quality of the copy submitted. Broken or indistinct print, colored or poor quality illustrations and photographs, print bleedthrough, substandard margins, and improper alignment can adversely affect reproduction.

In the unlikely event that the author did not send UMI a complete manuscript and there are missing pages, these will be noted. Also, if unauthorized copyright material had to be removed, a note will indicate the deletion.

Oversize materials (e.g., maps, drawings, charts) are reproduced by sectioning the original, beginning at the upper left-hand corner and continuing from left to right in equal sections with small overlaps.

Photographs included in the original manuscript have been reproduced xerographically in this copy. Higher quality 6" x 9" black and white photographic prints are available for any photographs or illustrations appearing in this copy for an additional charge. Contact UMI directly to order.

Bell & Howell Information and Learning
300 North Zeeb Road, Ann Arbor, MI 48106-1346 USA

UMI®
800-521-0600

PROCESSING AND CREEP BEHAVIOUR OF SILICON CARBIDE-PLATELET REINFORCED ALUMINA

By

ROSAURA HAM-SU, B.Eng.

A Thesis
Submitted to the School of Graduate Studies
in Partial Fulfilment of the Requirements
for the Degree
Doctor of Philosophy

McMaster University

CREEP OF SILICON CARBIDE-PLATELET REINFORCED ALUMINA

DOCTOR OF PHILOSOPHY (1997)
(Materials Science and Engineering)

McMaster University
Hamilton, Ontario

TITLE: Processing and Creep Behaviour of Silicon Carbide-Platelet Reinforced Alumina.

AUTHOR: Rosaura Ham-Su, B.Eng. (Universidad Iberoamericana)

SUPERVISOR: Professor D.S. Wilkinson

NUMBER OF PAGES: xiii, 150

ABSTRACT

The creep rates of SiC whisker reinforced Al_2O_3 have been found to be one or two orders of magnitude lower than the creep rate of unreinforced alumina. However, whiskers are a serious health hazard due to their asbestos-like geometry, they are expensive (thousands of dollars per kilogram), and they tend to get damaged during processing. Platelets have been proposed as an alternative to whiskers due to their reinforcement potential comparable to that of whiskers, forgiving geometry (with respect to safety), better thermal stability, lower price (hundreds of dollars per kilogram) and ease of processing. Up to now, research in platelet reinforced ceramics has concentrated mainly in room temperature properties and little is known about their high temperature mechanical properties. The aim of this work was to study the way in which different reinforcement network morphologies affect the creep behaviour of SiC-platelet/Al_2O_3 composites and to determine the important deformation mechanisms at the studied temperature (1250°C). To this end, composites with different platelet volume fractions (0 to 30%) and orientation distributions were fabricated. The samples were subjected to flexure and compression creep tests and characterized using optical and electron microscopy, dilatometry, and neutron diffraction. The analysis of the creep behaviour was found to be complicated by the differences in impurity content in the samples and the increase in glass content with the platelets volume fraction. However, the results clearly indicate a strong influence of the reinforcement morphology on the creep properties. Special attention was given to an unusual time-dependent transition from high to low creep strain rate in some of the composites. The phenomenon was ascribed to the possible relief of bending strains in the platelets. In addition, some of the possible main mechanisms responsible for the increased creep resistance in SiC-whisker reinforced ceramics were found not be operative in platelet-reinforced ceramics.

ACKNOWLEDGEMENTS

I would like to thank my supervisor Professor D.S. Wilkinson for his patience, guidance and help throughout this thesis. Professors P.S. Nicholson and R. Pelton kindly accepted to be part of my Ph.D. committee and provided valuable guidance. Professor J.D. Embury was always a source of enthusiasm and encouragement through all of my thesis topics. He also makes great seafood soup.

Connie Barry somehow managed to keep everything in the ceramics lab working, even the hot press. She let me try everything and anything, was always willing to give advice, and didn't even get too upset when I tried hot pressing in air.

Thanks to Dr. John Root for teaching me how to do neutron diffraction, and for helping me figure out the difference between reality and artifacts in my results. He was always available, even at ungodly hours.

Professors W. Pompe and W. Kreher kindly helped in interpreting some of the data, and were always willing to take the time to answer my questions.

Ed McAffrey provided invaluable guidance in modernizing the creep lab. Thanks to John Hudak for his help in using the SEM, and in preparing samples.

David Bloyce was a great help in preparing the tape-cast samples. He was always there to provide encouragement, even through the e-mail. Dr. Kevin Plucknett was always willing to discuss ideas and results. His constant enthusiasm was contagious. Veronika Czerneda was always helpful in all my dealings with the McMaster administration.

The grad students in A206 and A204 were always fun to be with. I would like to thank them for making my experience at Mac a very.pleasant one.

The Ontario Centre for Materials Research is to be thanked for providing much of the funding for this research.

A very special thanks to Ali, my ever-present companion for many years, always there during those after school evenings.

Whatever I do well would not be possible without the cheers and love from Michael, Sui-chi, Papá y Mamá. My debt is beyond words. This thesis is dedicated to them.

TABLE OF CONTENTS

LIST OF FIGURES

LIST OF TABLES

1. INTRODUCTION.

Current interest in the high temperature mechanical behaviour of ceramic/ceramic composites derives from the potential use of these materials in high temperature structural applications, such as heat engines. The mechanical properties of the composites at elevated temperatures depend, among other factors, on the distribution and morphology of the constitutive phases, the nature of the interface between the phases and the impurities present. Before ceramic composites can be used reliably in structural applications at elevated temperatures, their creep response must be understood.

One of the most widely studied ceramic composites consists of an alumina matrix reinforced with silicon carbide whiskers. Commercial applications of these materials include cutting tools, valve and pump components, and extrusion dies (Lieptzky et al 1988). The composites exhibit three- to fourfold increases in fracture toughness at room temperature (Becher and Wei 1984) and show increased resistance to erosion and thermal shock (Tiegs and Becher 1987) as compared with the monolith. In addition, the creep rates of SiC whisker reinforced Al_2O_3 have been found to be one or two orders of magnitude lower that the creep rate of unreinforced alumina (Becher and Wei 1984). The mechanisms by which whiskers decrease the creep rates are believed to be related to their high aspect ratio. However, whiskers are a serious health hazard due to their asbestos-like geometry (Birchall et al. 1988), they are expensive (thousands of dollars per kilogram), and they tend to get damaged during processing. This has encouraged research into other types of reinforcement. Platelets have been proposed as an alternative to whiskers due to their reinforcement potential comparable to that of whiskers (Claussen 1990, Baril and Jain 1991, Wilkinson and Pompe 1997), forgiving geometry (with respect to safety), better thermal stability, lower price (hundreds of dollars per kilogram) and ease of processing (as they do not fracture as readily as whiskers during green processing operations such as ball milling). Up to now, research in platelet reinforced ceramics has concentrated mainly on room temperature properties. Little is known about the high temperature mechanical properties of platelet reinforced ceramics. The aim of this work was to study the way in which different reinforcement network morphologies affect the creep behaviour of SiC-platelet/Al_2O_3 composites and to determine the important deformation mechanisms at the studied temperature (1250°C).

The thesis is organized as follows:

-Chapter 2, Literature Review, contains the background material for the work presented in later chapters. This chapter is divided in two main sections. The first section constitutes the background material necessary to understand the materials fabrication. The second section deals with creep of SiC reinforced Al_2O_3.

-Chapter 3, Materials Development, describes the relevant characteristics of the commercial powders used, the development of different green fabrication procedures, and the sintering of the ceramic samples.

-Chapter 4, Experimental Methods, describes the procedure followed to prepare the samples for microscopy and the experimental setups used in the microstructural and mechanical characterization of the samples.

-Chapter 5, Results, is divided according to the experimental techniques employed to obtain the results presented.

-Chapter 6, Discussion, is divided in smaller specific discussion topics which mostly follow the Results chapter sequence. Some of the modeling presented uses relatively elaborate calculations. These calculations are then shown in the Appendix so as to not distract from the main purpose of the discussion.

-Chapter 7 contains the summary of the experimental observations, the conclusions derived from this work and some suggestions for future research.

2. LITERATURE REVIEW.

2.1. Introduction.

This chapter is divided in two sections. The first, Processing, constitutes the background material for Chapter 3 (Materials Development) and deals with the consolidation of ceramic powders. A general description of the main physical aspects of the stability of colloidal dispersions is given, followed by a brief introduction to the fundamentals of rheology and its use to optimize slurry formulations. In addition, a review on the two consolidation methods used (tape casting and slip casting) is given. These are well known techniques, thus only some of the particulars will be discussed. The review is somewhat general with strong emphasis on SiC (-whisker or -platelet) reinforced Al_2O_3.

The second section, on Creep of SiC Reinforced Al_2O_3, is centred in silicon carbide whisker reinforced alumina. The title would suggest the inclusion of nanocomposites and platelet-reinforced ceramics. However, 1) the probable creep mechanisms (Todd 1995) relevant to SiC/Al_2O_3 nanocomposites seem not to be directly relevant to platelet-reinforced ceramics, 2) the literature on the creep behaviour of platelet reinforced ceramics is limited, and 3) there are important similarities between whisker- and platelet-reinforced ceramics. Thus a review mainly on SiC-whisker reinforced alumina is the most appropriate to our topic.

2.2. Processing.

The mechanical behaviour of ceramics, at high and low temperatures, is affected by the processing route used to fabricate them. Creep deformation of ceramic/ceramic composites, among other characteristics, depends on the reinforcement morphology, volume fraction and distribution, and diffusivity and diffusion path length of atomic species. The morphology and distribution of the reinforcement network can be tailored to a certain extent during processing. The diffusion characteristics are affected by the presence of glassy phases and impurities which tend to facilitate diffusion in ceramics. In particular, the impurities type and quantity will be dependent on the processing route used to fabricate the ceramic. Thus, the high temperature behaviour is better studied when the fabrication conditions are also considered. It is only natural to start the next section by explaining the general concepts used in processing to attain the different microstructures. To a great extent, it was during the green processing that the characteristics of the composites were determined. Different microstructures in the end-product can be obtained by colloidal routes as they enable and facilitate the manipulation of interparticle forces (Lange 1989). Thus, colloidal processing was used to produce powder compacts that were later made dense by heat treatment.

2.2.1. Particle Dispersions.

The behaviour of a colloid depends on all the surface forces present in the system (Horn 1990). An attractive van der Waals force acts at all separations between like particles; it arises from the interaction of atomic and molecular electric dipoles. This is manifested in practice by the coalescence of fine powders. If the space between the surfaces is filled with a pure liquid[1] the force between them is reduced but the surfaces still attract each other. Colloid stability arises by inserting an energy barrier between the states of separation and contact. If the medium between the two surfaces is no longer a pure liquid, new phenomena may arise leading to a repulsive force between the surfaces. The repulsive forces between particles can arise from the presence of surface charges (electrostatic forces) and/or by steric hindrance from adsorbed long chain polymer molecules. It is usually assumed that the contributions to the total free energy from attractive and repulsive forces are additive, so that depending on the range and relative strengths of these two contributions a variety of total free-energy curves may result. For convenience, the state of infinite separation is usually chosen as that of energy zero.

A colloidal dispersion represents a state of higher free energy than that corresponding to an agglomerate. Passage to a state of lower free energy will tend to occur spontaneously unless there is a substantial energy barrier preventing the elimination of the colloidal state. In the presence of such a barrier the system will be metastable and may remain in that state for a very long time. On the other hand, if conditions are adjusted so that the energy barrier becomes small, or disappears, then the colloidal state becomes unstable. Thus, the question of the preparation and stability of colloidal systems is closely tied up with the factors that give rise to free energy barriers of adequate height to prevent the breakdown of the colloidal state.

---

[1] By 'pure liquid' is meant a liquid that is not a miscible mixture or has been adulterated in any way i.e. it is a pure substance.

In most colloidal dispersions the energy necessary to carry a system over the energy barrier comes from the Brownian motion of the particles (or gravity for larger particles), which results from the random bombardment of the surface of the particles by molecules of the medium. The average translational energy of colloidal particles undergoing Brownian motion is of the order of (3/2)kT per particle, where k is Boltzmann's constant and T is the absolute temperature. At 300°K two particles bring into a collision an energy of 10^{-20}J. However, there is a finite probability that at a given moment a particle may have a larger or smaller energy. The chances of a collision involving a total energy of several times kT (say 10kT) become very small, so that, provided the free energy barrier is sufficiently high, the dispersion will remain infinitely in a metastable state: it is colloidaly stable. Instability will ensue if the barrier height is reduced to say 1-2kT. In practice, the barrier height is found to be a sensitive function of several factors including the composition of the medium, temperature and pressure. Instability and flocculation are often caused by the reduction in the height of the barrier resulting from a change in one or more of these factors (Everett 1988).

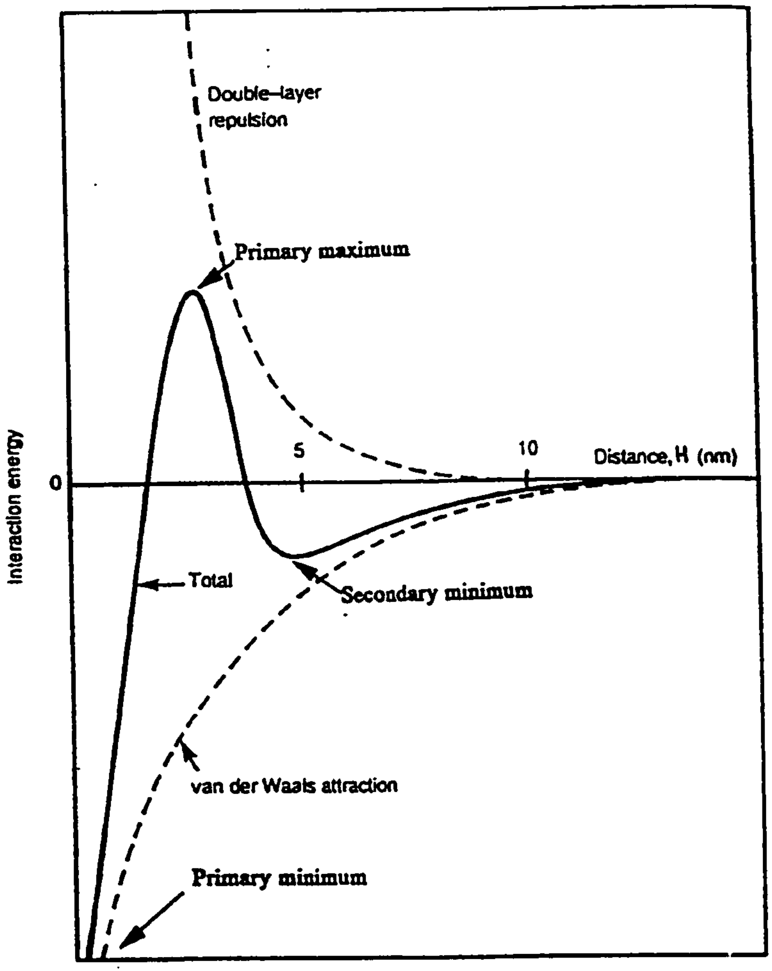

Figure 2.1. Potential energy curve showing primary and secondary minimums (Israelachvilli 1992).

Figure 2.1 shows schematically how aggregation is prevented by a high energy barrier, but preceding this is a relatively shallow minimum. If the depth of the secondary minimum is of the order of a few kT, then small, relatively weakly bound aggregates (flocs) can form. Although the flocs are sufficiently stable not to be completely dissociated by Brownian motion, they may disintegrate under externally applied hydrodynamic forces, such as stirring. The force acting between two bodies results from a summation of all the interatomic forces acting between all of the atoms of the materials involved. The van der Waals forces exist between molecules, varying as r^{-7} where r is the intermolecular distance.

$$F^{att} = -\frac{A}{r^7} \qquad (2.1)$$

Thus,

$$\Delta G^{att} = -\Delta W = -\int_d^\infty F^{att} dr = A\int_d^\infty \frac{1}{r^7} dr = \frac{A}{6d^6} = \frac{A'}{d^6} \qquad (2.2)$$

which is the work done in separating reversibly a pair of atoms or molecules from a distance d to infinity. A' is related to the nature of the individual molecules,through their polarisability and a characteristic frequency (identified with that corresponding to the first ionisation potential). For two like molecules or atoms in vacuum,

$$A' = \frac{3}{4} h\nu\alpha^2 \qquad (2.3)$$

where, h is Planck's constant, ν is a characteristic frequency and α is the polarisability.

The attractive force increases and the free energy becomes increasingly negative as the atoms approach one another. However, at close distances their electronic clouds begin to interact. If the electrons are in non-bonding orbitals, this gives rise to a repulsive force and an increase in free energy which becomes effectively infinite when the electronic clouds interpenetrate. This is known as Born repulsion.

One method of calculating the potential energy of interaction between two particles is to assume that every molecule in one particle interacts with each molecule in the other according to a Lennard-Jones potential and that the total free energy of interaction is obtained by summing all possible pairs of molecules. The repulsive contribution can be neglected except for those molecules on opposing surfaces. Hamaker (1937) made a pair wise summation over all the atoms in two spherical bodies of radius R_S and showed that the attractive force between them is given by:

$$F(r) = -\frac{A_H R_s}{12D^2} \qquad (2.4)$$

where D is the distance between spheres and A_H is the Hamaker constant which depends on the polarisabilities and the number densities of the atoms in the two bodies. From the last equation:

$$\Delta G^{att} = -\frac{A_H R_S}{12D} \qquad (2.5)$$

It is important to note that the energy of attraction between particles falls off much more slowly than that between single molecules: the long range interactions between colloid particles plays a crucial role in determining their properties (Horn 1990). As mentioned before, an intervening medium such as a liquid will decrease the magnitude of the interaction (i.e. decrease A_H).

In the case of electrostatic forces, surfaces may become electrically charged by a variety of mechanisms, some of the most important ones are the following (e.g.Everett 1988, Hiemenz 1977):

i) *Ionisation of surface groups.* If the surface contains acidic groups, their dissociation gives rise to a negatively charged surface, as shown in Figure 2.2.

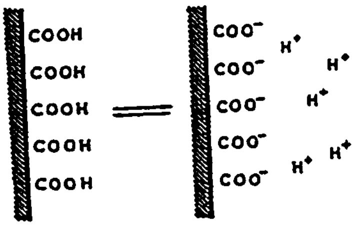

Figure 2.2. Acidic surface. The magnitude of the surface charge depends on the acidic or basic strengths of the surface groups and on the pH of the solution. The surface charge can be reduced to zero by suppressing surface ionisation by decreasing the pH. Many metal oxides exhibit amphoteric behaviour in that both positively and negatively charged surfaces can be obtained by varying the pH (Everett 1988).

ii) *Differential solution of ions from the surface of a sparingly soluble crystal.* For example, when a silver iodide crystal is placed in water, solution occurs until the product of ionic concentrations equals the solubility product, e.g. $[Ag^+][I^-] = K_s = 10^{-6} mol/dm^3$. If equal amounts of Ag^+ and I^- were to dissolve then there would be no surface charge. However, silver ions dissolve preferentially leaving a negatively charged surface. If Ag^+ ions are now added to the solution (in the form say of silver nitrate solution), the preferential solution of silver ions is suppressed and the charge may fall to zero. Further additions may lead to a positively charged surface, since it is now iodide ions that are preferentially dissolved.

iii) *Isomorphous substitution.* A clay may exchange an adsorbed, intercalated or structural ion with one of the lower valency, producing a negatively charged surface. Al may replace Si in the surface producing a negative surface charge. In this case a zero surface charge can be obtained by reducing the pH, the added H^+ ions combining with the negative charges on the surface to form OH groups.

iv) *Specific ion adsorption.* Surfactant ions may be specifically adsorbed, leading, in the case of cationic surfactants to a positively charged surface and in the case of anionic surfactants, to a negatively charged surface.

In the case of colloids, we are particularly interested in the ionic atmosphere which is developed around a charged colloid particle. It is usual to call this ionic atmosphere an electrical double layer. The charge on the particle surface is balanced by the total charge in the double layer in which there is an excess of oppositely charged ions (counter ions). An electrical double layer consists of an arrangement of charges in two parallel planes. Thermal motion causes the counter-ions to be spread out in space, forming a diffuse double layer. The electrical potential Ψ falls off exponentially with the distance d, for a planar surface (Everett 1988):

$$\Psi = \Psi^{o} \exp(-\kappa d) \qquad \text{(2.6)with}$$

$$\frac{1}{\kappa} = \left(\frac{\varepsilon k T}{e^{2} \sum c_i z_i^{2}} \right)^{1/2} \qquad (2.7)$$

where, c_i is the concentration of ions, z is the valency of the ions, ε is the dielectric constant of the medium, e is the elementary charge and $1/\kappa$ is the Debye length. All distances within the double layer are judged large or small relative to this length. This is illustrated on Figure 2.3. The distance away from the wall that an electrostatic potential persists may be comparable to the dimensions of colloidal particles themselves (Hiemenz 1977). It is important to note that the distance over which significant potentials exist decreases with increasing electrolyte concentration and the range of the electrostatic potential decreases as the valence of the ions in solution increases.

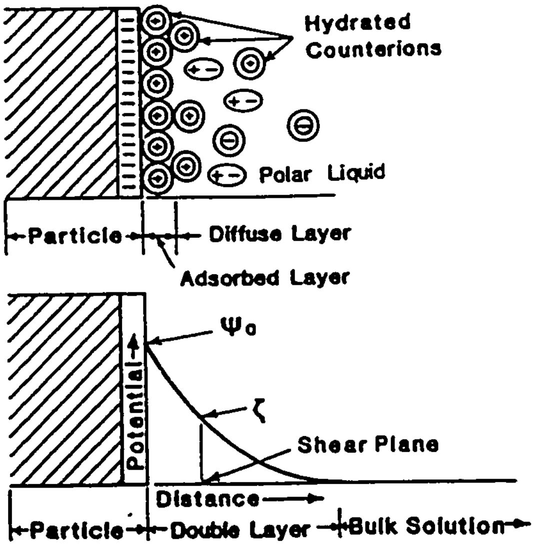

Figure 2.3. Double layer, the potential decreases exponentially with distance. The zeta potential, ζ, is determined by the shear plane (Reed 1988).

When two similarly charged colloid particles, with their associated double layers, move toward one another they will begin to "feel" one another's presence as soon as any appreciable overlap on the tails of the charge distributions occurs, the two ionic charge clouds will repel each other. At a distance the particles are "seen" by the others as neutral uncharged identities. At closer separations each particle "sees" each other as partially charged particle of the same sign. This distance dependens on the charge of the particle and the electrolyte concentration. This was modeled by Derjaguin and Landau (1941) and Verwey and Overbeek (1948) and is known as the DLVO theory.

When a DC electric field is applied to a dispersion of charged particles, the double layer is polarised but not permanently stripped off the particle, the particles move with a velocity proportional to a so-called zeta potential ζ associated with the ions that remain well attached to the particle's surface when moving in a fluid. A physical mental picture can formed by dividing the aqueous part of the double layer with a hypothetical boundary known as the Stern surface (Hiemenz 1977). The Stern surface is drawn through the ions which are assumed to be adsorbed on the charged particle wall. As the particle moves inside the fluid, part of its double layer gets sheared-off and only the Stern layer remains, associating an apparent charge to the particle (Figure 2.3). The particle movement due to the imposed external potential is called electrophoresis. For the electrophoretic transport of non-conducting particles (Reed 1988),

$$\zeta = \frac{f_H \eta v_e}{\varepsilon E} \qquad (2.8)$$

where η is the viscosity of the medium, v_e is the electrophoretic velocity for an imposed electric field E and f_H is the Henry constant whose value is close to 1. The electrophoretic mobility of particles in dilute suspension may be determined by measuring the migration velocity of individual particles in a known potential gradient as a function of the pH of the suspension. Then, the average zeta potential can be calculated from the average mobility using equation 2.8. The pH at which the zeta potential is zero is termed the isoelectric point (IEP), raising or lowering the pH form the IEP will increase the absolute value of the zeta potential. A typical zeta potential curve is shown on Figure 2.4.

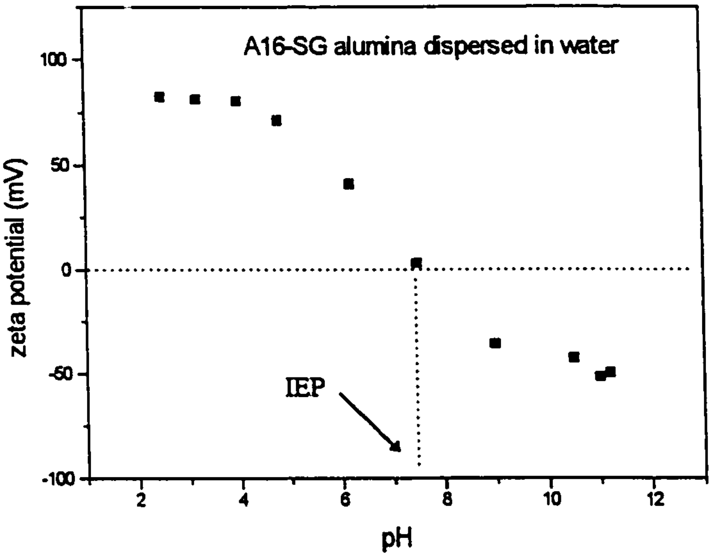

Figure 2.4. Typical variation of zeta potential with pH.

The addition of surface active agents is perhaps the simplest method of modifying surface forces. In general, surfactant molecules consist of a polar (hydrophilic) head and a non-polar (hydrophobic) tail. In a solution of hydrophilic particles in a non-polar solvent, or vice versa, the surfactants will readily adhere to particle surfaces, preferring hydrophilic-hydrophilic (polar) and hydrophobic-hydrophobic (non-polar) contacts (Horn, 1990). For example, an ionic surfactant could be used to disperse non-polar particles in water. The hydrophobic end of the surfactant would cover the particle's surface leaving the ionic end towards the solvent, effectively creating an electrical double-layer. The same type of phenomenon can occur with polar particles in non-polar solvents. In this case, the surfactant layer can prevent agglomeration by preventing the surfaces from coming into close contact (steric stabilisation) where the van der Waals attraction is strong.

Polymers in colloidal systems function in a variety of ways depending on their molecular structure and concentration, the nature of the solvent and the characteristics of the particles. In considering forces between surfaces separated by a polymer solution, it is important to know whether or not polymer molecules adsorb to the surfaces, which depends on whether segments of the polymer prefer to be in contact with the particle's surface or with the solvent. If the polymer is adsorbed the particles get coated with a polymer layer giving rise to steric stabilisation. If enough polymer is adsorbed, the thickness of the coating is sufficient to keep particles separated and at those separations the van der Waals forces are too weak to cause the particles to adhere. However, the adsorbed layer of polymer is not usually dense enough to enable it to behave as a hard surface. The polymer chains will extend out into the medium to an extent which depends on how they interact with the medium: the more affinity between the polymer segment and the medium the more open the structure (Horn 1990, Ploehn and Russel 1990).

On collision between particles, the chains will interpenetrate. This has two consequences (Everett 1988):

1) The local density of polymer segments increases (fluid will diffuse into the region between the surfaces to reduce the segment concentration and so to drive the surfaces apart).

2) Because the segments are linked together in a polymer chain, the increased concentration will constrain the chains, leading to a reduction in the number of configurations they can adopt. This implies a reduction in the entropy and, therefore, an increase in free energy.

The magnitude of the repulsion arising from the presence of the adsorbed layer clearly depends on the density with which it covers the surface. As the density decreases, the total-interaction potential curve changes as depicted in Figure 2.5 (Everett 1988).

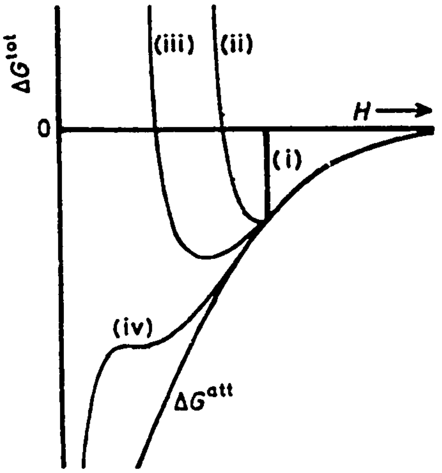

Figure 2.5. Changes of interaction potential with polymer density: (i) hard surface, (ii)-(iv) decreasing density of the layer. H is distanc. from the particie surface (Everett 1988).

Reduction in the range of the repulsive forces may be also achieved by changing the nature of the fluid, for example by adding a non-solvent for the polymer. Polymer segment-medium interactions are decreased and at some concentration of additive the segment-segment interactions dominate. When in solution, a polymer assumes the shape of a random coil in the absence of segment-segment interactions. The mean configuration of a random coil is illustrated in Figure 2.6. In a "good" solvent there is a repulsion between the segments, having a more extended chain. A more compact configuration would be achieved in a poor solvent where the segments attract each other and the coil shrinks.

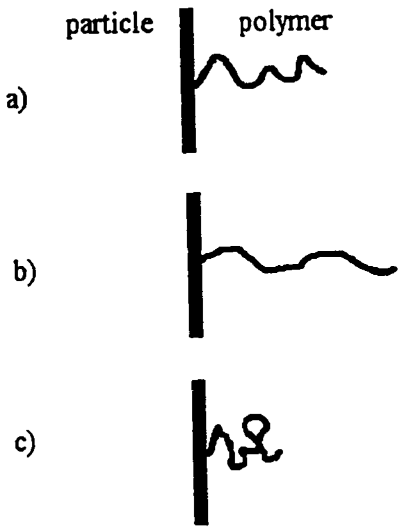

Figure 2.6. a) Random coil, b) good solvent, c) poor solvent.

The way in which the interaction potential varies as one passes through this configurations is illustrated in Figure 2.5. Curve ii refers to the situation where segment-segment interactions rapidly increase the free energy (dislike each other). The rise in the free energy is due to entropy effects. In iii the segments prefer to be near segments, therefore, the curve minimum is closer to the particle surface. Entropy effects make the curves rise steeply (Everett 1988).

If high molecular weight molecules are added to a dispersion, bridging flocculation may occur. In this, different segments of a polymer chain adsorb on separate particles and draw them together. The use of block copolymers can overcome this problem. These molecules consist of two different polymer chains grafted together end-to-end. if a block copolymer is dissolved in a liquid which is a good solvent for one of its ends but a poor solvent for the other the latter will have a strong tendency to adsorb to particles, while the remainder of the molecule remains extended into the solvent. As with surfactants, a coat of non-adsorbing and non-bridging polymer is attached to the particle, effectively preventing other particles from approaching (Horn 1990).

There is another effect. Consider again simple polymers (i.e. homopolymers), this time dissolved in a good solvent so that they are non-adsorbing. In this case two competing effects arise as two surfaces approach. On the one hand, a polymer chain in solution between the surfaces will be compressed into a smaller volume, decreasing the configurational entropy of the chain, therefore raising the free energy; this results in a repulsive force between the surfaces (depletion stabilisation). On the other hand, the system may loose less entropy if the polymer chain is evicted from the region between the surfaces: this costs translational (or mixing) entropy but no configurational entropy. With more polymer chains outside the region of solution between surfaces and fewer inside, there is an osmotic pressure difference which results in an attractive force. This phenomenon is known as depletion flocculation (Horn 1990).

According to the DLVO theory two identical particles must always attract each other at surface separations below 2-4 nm. This final adhesion would be strong and irreversible and the particles would be at the pirimary minimum (see Figure 2.1). However, there are observations which are not consistent with the DLVO theory in this short range regime (Pashley and Israelachvili 1984). For example silica particles cannot be coagulated in concentrated salt solutions even at zero charge, also clay platelets can swell spontaneously in aqueous solutions (DLVO predicts overall attractive forces). In these examples a short-range repulsive force must be operating and must extend at least 2 nm to remove the primary minimum. When a simple liquid of spherical molecules is confined to a narrow region between two flat plates, the molecules prefer to lay parallel to the surfaces (Pashley and Israelachvili 1984, Horn 1990). Presumably this is a lower free energy state as the molecules can pack more efficiently (Vellamakanni et al. 1990). When the separation between surfaces does not allow an integral number of layers, the packing is innefficient and the free energy increases. When two smooth solid surfaces are forced together in such a liquid, closer than a few molecular diameters, the force of interaction alternates between maxima and minima. The spacing between the maxima and minima being approximately equal to the molecular diameter of the liquid. If the liquid is a solution, there is the added possibility that the finite size of solute species will affect the forces. This force is usually called a "hydration force" since most studies have been done with water.

In summary, the total interaction potential curve is given by the following contributions:

$$\Delta G = \Delta G^{att}\ \text{(van der Waals)} + \Delta G^{rep}\ \text{(short range)} + \Delta G^{rep}\ \textit{(electrostatic)} + \Delta G^{rep}\ \textit{(steric)} + \Delta G\ \textit{(other effects)} \quad\ldots\ldots\ldots\ldots (2.9)$$

which will determine the stability of the dispersion.

2.2.2. Rheology of Particulate Dispersions.

Rheology plays an important role in most aspects of ceramic processing, including preforming operations (e.g. mixing and milling), shape-forming operations (e.g. extrusion, slip casting and tape casting), drying (e.g. liquid transport in pores) and densification (e.g. liquid-phase sintering) (Sacks et al. 1987). The interest on rheology in this research is for slip control. In particle/liquid systems, rheological properties are especially sensitive to the state of particulate dispersion thus, enabling the assessment of interparticle forces. There are four basic classifications of rheological behaviour for dispersions (Ring 1987), as shown in Figure 2.7.

A) A Newtonian fluid, in which the shear stress is proportional to the strain rate[2]. The slope of the curve shown in Figure 2.7 represents the viscosity.

B) A Bingham plastic, in which a yield stress, τ_0 , occurs at zero strain rate, followed by a linear relationship as for a Newtonian fluid.

C) A pseudoplastic fluid with a non-linear shear stress-strain rate relationship in a shape roughly similar to a Bingham plastic.

D) A shear thickening fluid, in which the shear stress increases with strain rate with an increasing slope.

---

[2] For a Newtonian fluid the shear stress on an interface tangent to the direction of flow is proportional to the distance rate of change of velocity, where the differentiation is taken in a direction normal to the interface (e.g. Shames 1982, Reed 1988). As illustrated in FIgure 2.8, this is,

$$\tau = \eta \frac{\mathrm{dv}}{\mathrm{dn}}$$

where the coefficient of proportionallity is the coefficient of viscosity η, τ is the shear stress, n the distance normal to the interface and v the velocity.

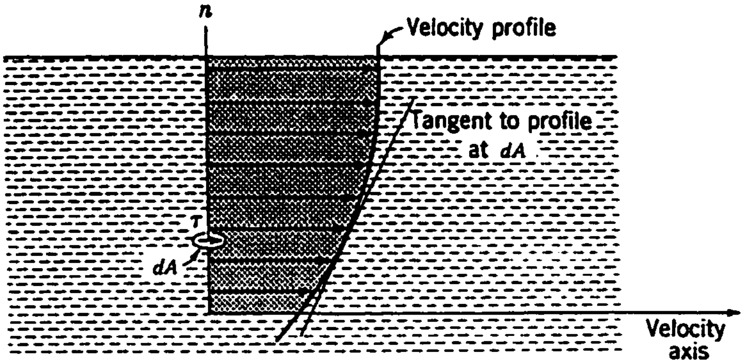

Figure 2.8. Well ordered parallel flow (Shames 1982).

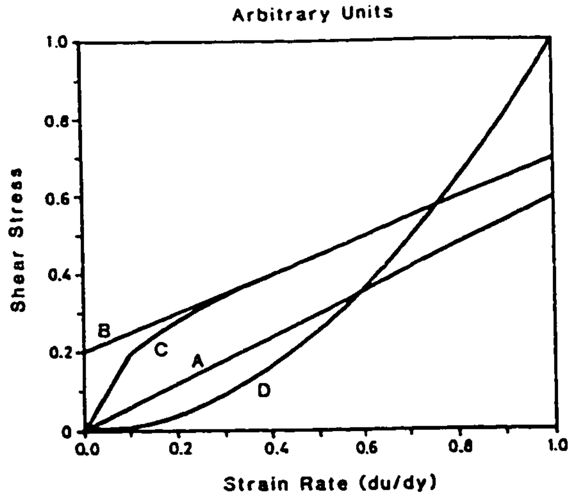

Figure 2.7. Rheological behaviour of ceramic powder dispersions: (A)Newtonian, (B)Bingham plastic, (C)pseudoplastic, and (D)shear thickening (Ring, 1987).

Dilute dispersed slurries exhibit Newtonian behaviour i.e. the viscosity is independent of the shear rate. At high volume fractions the dispersed slurries become dilatant i.e. shear thickening. The viscosity increases with the shear rate because the system must increase its volume to allow closely spaced, repulsive particles to slip past one another. Flocced slurries exhibit pseudoplastic, thixotropic rheology (viscosity decreases with increasing shear rate and is history-dependent) because the applied forces separating attractive particles depend on the differential acceleration rate i.e. shear rate. Once particles are separated, flocculation and network formation are time dependent. Pourable, dispersed slurries can contain up to 60 vol% solids, whereas the volume fraction of pourable, flocced slurries is much lower (between 5 and 20 vol%) and depends on the particle mass (size), which governs the forces separating particles during flow (Lange 1989). The state of a dispersion can be evaluated from the suspension relative viscosity as a function of shear rate (Sacks et al. 1987). In general, the lower the viscosity the better dispersed the system. From this, it is evident why viscosity is considered the best parameters to measure for slip control (Mistler 1990).

2.2.3. Tape Casting.

The tape casting process begins with the forming of a slurry by the dispersion of inorganic ceramic powders in a fluid that contains a surfactant to produce interparticle repulsive forces, followed by the addition of organic binders and plasticity modifiers that will give strength and flexibility to the consolidated body. The slurry is cast onto a plane surface by passing it beneath the edge of a blade that levels it into a layer of controlled thickness and width as the blade advances along the casting surface (Shanefield and Mistler 1974, Williams 1976, Mistler et al. 1978). When the solvents evaporate the solid particles coalesce into a relatively dense, flexible sheet kept together by the organic binders. Tape casting can be performed using either aqueous or non-aqueous systems. Nonaqueous solvents have a lower latent heat of evaporation so that drying is rapid without requiring significant heat flux to the evaporation interface. It has been suggested (Shanefield, 1986) that to achieve the highest green densities, fine powders and non-aqueous solvents should be used since aqueous systems provide hydrogen bond-linkages which can form agglomerated flocs. Also, the use of an aqueous solvent might hydrate certain constituents (Williams 1976). However, aqueous systems are more environmentally friendly which might outweight any of the advantages of nonaqueous solvents in most industrial applications.

The rheology of the tape casting slurry is of major importance for the success of the process. Firstly, as mentioned in the previous section, the lower the viscosity of the slurry the better the dispersion of the particles (for the same quantity of liquid), which results in good particle packing, high densities and homogeneous microstructures. Secondly, a shear-thinning behaviour is desirable. During tape casting a velocity gradient exists in the liquid underneath the doctor blade, extending with decreasing intensity back into the recevoir. In a pseudoplastic slurry the viscosity decreases under the blade. After the blade passes, the shear rate decreases rapidly and the viscosity increases. This restricts the flow of the suspension, 'freezing' the particles in place and thus enabling an homogeneous distribution of particles. This effect is particularly important when segregation and sedimentation are to be avoided as when tape casting particles of different sizes and/or densities.

If the tape casting slurry contains anisotropic particles, such as platelets, a preferred orientation or texture can be achieved due to the flow forces exerted by the blade (Roosen 1988, Dayton et al. 1984, Watanabe et al. 1989). The mechanism likely to contribute to grain orientation during tape casting is the shear produced in the liquid between the doctor blade and the glass (Dayton et al. 1984). The differential flow rate will tend to flip and hold tabular particles in the slurry in an orientation parallel to the direction of laminar flow. As before, if the slurry is pseudoplastic, after it passes through the doctor blade, the apparent viscosity of the slip will naturally increase in the absence of shear and the particles will tend to be held in position until drying commences. It has been found (Dayton et al. 1984) that grain orientation and green density tend to show an inverse relationship. This would indicate that the rheology of the slurry is important for the grain orientation process. Orientation might be incomplete in the green tape due to the high viscosity of the slurry, but lamination can also contribute to the aligning process, since it permits lateral tape flow during pressing. This promotes better alignment of the anisotropic particles in the green body.

In practical terms, the shear rate can be changed/calculated with the casting speed and the blade height. Assuming a constant shear rate in the slurry between the blade and the casting surface (Dayton et al. 1984):

$$\dot{\gamma} = \frac{dv}{dx} \cong \frac{\text{carrier speed}}{\text{blade height}} \qquad (2.10)$$

Drying of the tapes should be controlled such that the difference in solvent content between the air and the slip is never large ensuring that drying is gradual and uniform. This allows the remaining solvent, in the bulk of the tape, time to redistribute in the drying tape. Excessively fast evaporation can cause a skin of dried slurry at the surface while liquid slurry remains underneath hence retarding the overall drying process (Roosen 1988, Plucknett et al. 1994b). Also, the skin inhibits bubbles of vapour floating to the surface and creates voids in the finished product. As the solvent evaporates during drying, the ceramic particles and plastics form a flexible, leather-like sheet of sufficient strength to allow the tape to be peeled from the glass casting surface after most of the solvent has evaporated.

After removing the dry tape it can be cut or punched into the desired shapes and can then be thermocompressed to produce laminates. Pressure has to be applied at a sufficient temperature to facilitate a short range redistribution of particles embedded in the secondary organic phase so that the adjacent layers bind together. This should be done under vacuum to eliminate any entrapped air between the tape layers. Pressures ranging form 1.38 to 138MPa are commonly used for lamination (Ettre and Castles 1972, Mistler 1990, Plucknett et al. 1994b).

The last stage before sintering is the binder removal from the greenbody. It constitutes an important step in the production of high quality ceramic components. As the green body is heated, volatile species evaporate, polymers decompose and combustion may occur in an oxidising environment. Binder removal is often associated with the production of cracks, voids and delamination. For the temperatures at which the binder volatisation is greatest the heating rate must be slowest (Roosen 1988) to allow time for the gaseous species to go through the channels without damaging the greenbody. Thermal gravimetric analysis (TGA) can be used to determine the burn out behaviour of the ceramic components to ensure a controlled removal of the binder. As the bodies are relatively compact the heating rate must be slow to prevent cracking of the body. The binder removal rate becomes more critical when dealing with smaller particles, as the pore channels decrease in size and the relative quantity of binder increases (Roosen 1988, Plucknett et al. 1994b).

2.2.4. Slip casting .

In slip casting, a slurry is formed with inorganic particles dispersed in a liquid (generally water), the slurry is poured or pumped into a permeable mold having a particular shape; capillary suction and filtration concentrate the solids into a cast adjacent to the wall of the mold. Permeable molds for casting are commonly made from gypsum with 40-50% porosity. Gypsum ($CaSO_4\ 2H_2O$) is formed from the reaction between plaster of Paris and water; $CaSO_4 \cdot 0.5H_2O + 1.5H_2O \rightarrow CaSO_4 \cdot 2H_2O$. The motivating force for the separation of the liquid may also be increased by pressure applied to the slurry, vacuum applied to the mold or centrifugal pressure. The casting time can range from a few minutes to weeks depending on the viscosity of the slurry and the end-thickness of the cast (Reed 1988). A slurry that is only partially deflocculated will cast more rapidly, but the cast will be more porous. A deflocculated slurry, in general, will take longer to cast but produce an homogeneous piece with a narrow range of pore sizes and adequate green strength to be handled with care. Additives and agglomerates can be controlled to a certain extent in the slurry, thus enabling the use of slip casting for high performance ceramics. Upon drying of the cast, capillary forces are produced when the water vapor condenses at particle contacts, bringing the particles closer together. After the liquid has been removed by evaporation, particles can be cemented together with previously soluble salts (e.g. with hydroxides) left at contact positions (Lange 1989). Separation of the piece from the mould normally occurs due to shrinkage during drying.

2.2.5. Sintering.

Sintering is the consolidation of the green body during exposure to relatively high temperatures. Solid state sintering does not usually begin until the firing temperature exceeds two-thirds of the melting temperature of the material, which is sufficient to cause atomic diffusion. The driving force for sintering is the reduction in the total free energy of the system mainly due to the reduction in surface area of the grains (Reed 1988). A uniform green density distribution will result in uniform shrinkage that will lead to an homogeneous structure (Roosen 1988). The sintering of ceramics containing reinforcing phases such as whiskers and platelets is complicated by the incorporation of these inclusions as they can form skeletal networks and hinder densification (Porter et al. 1987). This constrained sintering (Lange 1987, Porter et al. 1987) can lead to the necessity of using pressure during densification such as in hot-pressing or hot isostatic pressing.

2.3. Creep of SiC reinforced Al_2O_3.

In general, whisker reinforced ceramic composites have a better fracture toughness and an increased resistance to thermal shock, erosion and creep when compared with monolithic materials (e.g. Becher and Wei 1984, Tiegs and Becher 1987, Lipetzky et al. 1991). At high temperatures, previous studies (e.g.Chokshi and Porter 1985, Becher et al. 1990) have found that the addition of 15-20 vol% SiC whiskers to an alumina matrix reduced the creep rates by up to two orders of magnitude. The mechanisms by which whiskers decrease the creep rates are believed to be related to their high aspect ratio. However, whiskers have some drawbacks. They constitute a serious health hazard (Birchall et al. 1988) due to their asbestos-like geometry; they are expensive (thousands of dollars per kilogram) and they are likely to get damaged during processing. This has encouraged research into other types of reinforcement. Platelets have been proposed as an alternative to whiskers due to their reinforcement potential comparable to that of whiskers (Claussen 1990, Baril and Jain 1991, Wilkinson and Pompe 1997), forgiving geometry (with respect to safety), better thermal stability, lower price (hundreds of dollars per kilogram) and ease of processing (as they do not fracture as readily as whiskers during green processing operations such as ball milling). Ceramic/ceramic composites with various types of platelets (e.g. alumina, silicon carbide and boron carbide) have been developed (e.g. Claussen 1990, Zheng 1990, Janssen and Heussner 1991, Nischik et al. 1991, Baril and Jain 1991, Liu et al. 1992, Tuffe et al. 1993, Huang and Nicholson 1993, Bloyce 1993, Chou and Green 1993, Mitchell et al. 1995). Up to now, research has concentrated mainly in room temperature properties. Little is known about the high temperature mechanical properties of platelet reinforced ceramics. However, one can expect similitudes in high temperature behaviour between whisker- and platelet-reinforced ceramics.

A typical creep curve, illustrated in Figure 2.9, can be seen as possesing four main features; an initial elastic extension, a period during which the deformation rate decreases (primary or transient creep), a period of constant deformation rate (secondary or steady-state creep), and finally a period of increasing deformation rate (tertiary or accelerating creep). The primary stage is due to structural changes that provoke hardening and the tertiary stage is usually caused by damage leading to failure. However, the shape of a creep curve can have considerable variations, depending on the particular material studied, the temperature and the stress (Kingery et al. 1976, Cannon and Langdon 1983, Wilkinson 1994). Nevertheless, a steady-state or near steady-state creep regime is often established during deformation. Creep data is usually analyzed with the Norton power law steady-state creep empirical equation:

$$\dot{\varepsilon} = A\sigma^{n}e^{-Q/RT} \qquad (2.11)$$

where $\dot{\varepsilon}$ is the steady state strain rate, σ is the far-field stress, and A is a parameter that depends, among other things, on the grain size of the polycrystal (Cannon and Langdon 1983), for a given material at a given temperature. The deformation is characterized by the stress exponent n, and a creep activation energy Q, that arises from the Arrhenius dependence of the diffusion coefficient on temperature. These creep parameters are related to plastic deformation mechanisms based on monolithic materials. The relations between stress exponents, other creep parameters, and plastic deformation mechanisms are well documented for monolithic materials (Cannon and Langdon 1983).

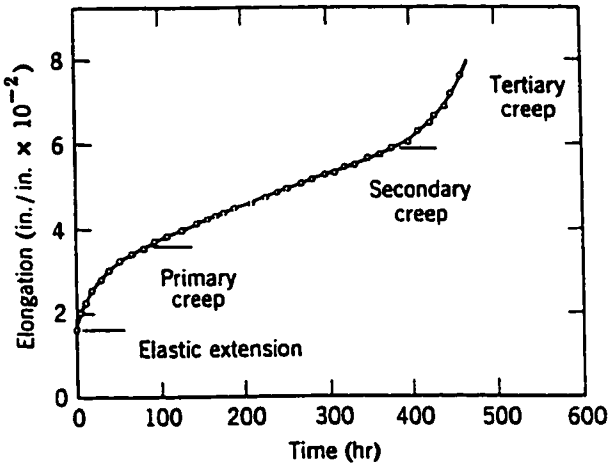

Figure 2.9. Typical creep curve for a monolithic material (Kingery et al. 1976).

The relations between deformation mechanisms and creep parameters have not yet been clearly established for multiphase ceramics (Arellano-Lopez et al. 1993). Moreover, often the time vs strain plots obtained for SiC-whisker reinforced alumina composites exhibit a continuous decrease in creep rate (e.g. Porter 1988, Lin and Becher 1990), showing primary, non-steady-state creep behaviour. Thus it is important to be careful when interpreting results based on Equation 2.11.

2.3.1. Creep of SiC-whisker reinforced Al_2O_3.

The creep behaviour of alumina composites reinforced with SiC whiskers has been reported in the literature numerous times since the 1985 study by Chokshi and Porter (e.g. Porter and Chokshi 1987, Porter et al. 1987, Porter 1988, Xia and Langdon 1988, Lipetzky et al. 1988, Becher and Tiegs 1988, Donaldson et al. 1989, Routbort et al. 1990, Nutt et al. 1990, Lin and Becher 1990, Jakus and Nair 1990, Arellano-Lopez et al. 1990, Lin and Becher 1991, Swan et al. 1992, Arellano-López et al. 1993, Lin et al. 1996). The characteristics of the materials and the testing conditions vary, making a straight comparison between results impossible. Differences in processing parameters (the kind of whiskers and alumina, the sintering aids used, the processing temperature and atmosphere, etc.) lead to different values of creep exponents and activation energy (Lin and Becher 1991). However, there are resemblances and tendencies that can be noted.

Creep exponents.

In general, when the composites are tested in flexure and at temperatures higher than 1400°C (e.g.Chokshi and Porter 1985, Porter et al. 1987, Xia and Langdon 1988) the creep exponents found are between 4 and 7. Porter et al. (1987) found a creep exponent of $n=5$ for flexure creep of 5, 15 and 20 vol% SiC-whisker reinforced alumina (the percentage of the reinforcing phase will always refer to volume percent, unless stated differently) tested in air at 1500°C. Transmission electron microscopy (TEM) characterization of the deformed composite revealed the presence of dislocation networks. From this and the obtained creep exponent, it was concluded that the results were consistent with a dislocation creep mechanism. Similar observations were made by Xia and Langdon (1988). However, these dislocation networks have also been detected in the as-processed matrix and have been ascribed to internal micromechanical stresses. The networks are stable and seem to either remain unchanged by creep deformation (Nutt 1984, Arellano-Lopez et al. 1990) or the after creep dislocation density is negligible and it is unlikely that dislocation glide plays a significant role in the deformation (Lipetzky et al. 1991). Thus, more recent studies tend to conclude (Lipetzky et al. 1991, Lin and Becher 1991, Arellano-Lopez et al. 1993) that the dislocation creep hypothesis is wrong. Instead they suggest that the higher creep rates and exponents are attributed to damage, mainly cavitation. This is supported by microstructural observations by scanning electron microscopy (SEM) and TEM (Lin and Becher 1990). Compressive creep experiments at temperatures higher than 1400°C (Arellano-Lopez et al. 1990) found stress exponents between 1 and 2. Since cavitation is enhanced in flexure as compared to compression, this supports the relationship between high creep exponents and damage accumulation in these type of composites.

At temperatures lower than 1400°C, both compressive and flexural experiments agree on the existence of two stress dependent plastic deformation mechanisms: one at low stresses characterized by stress exponents between 1 and 2, and another at higher stresses characterized stress exponents larger than 2 (Lipetzky et al. 1988, Arellano-Lopez 1993). The low stress exponent regime ($1<n<2$) has been ascribed to diffusion controlled mechanisms like in monolithic materials. There is general agreement, as before, in that the change in n is attributable to cavitation and other forms of damage[3]. Samples crept in the $n>2$ regime suffer important cavitation and cracking, even for small strains, suggesting that the large stress exponents obtained at high stresses are the result of accelerated strain rate values caused by irreversible damage accumulation (Lipetzky et al. 1991, Arellano-Lopez et al. 1993).

Reinforcement loading.

Porter et al. (1987) concluded that the whisker loading (5, 15 and 20%) does not seem to significantly affect the creep rates at 1500°C. However, they do not mention the grain sizes of the different composites. The composites were all densified at 1500°C to full density with a pressure of 24MPa. However there is no mention of the length of sintering time. It is very likely that the matrix grain size in the different composites was different, perhaps in such a way that the creep rates ended up being the same at 1500°C.

In other works, the reinforcement volume fraction influence can be roughly divided into two regimes: low (less than 10%) and high (more than 15%).

Low whisker loadings (≤10%). In some cases, the shape of the strain vs time curves would suggest that true steady-state conditions are reached, as they show a clearly linear regime (Porter 1988). The stress exponent tends to be higher and the strain to fracture lower than in pure alumina (Porter et al. 1987, Lin and Becher 1991, Arellano-Lopez et al. 1993). Damage has been detected in the form of triple point cavities near whisker sites attributed to stress concentrations in the vicinity of the whiskers. However, the creation of damage is sufficiently slow to permit the achievement of quasi-constant strain rate for each stress. The

---

[3] The role of the Al_2O_3/SiC interface and the oxidation reactions are discussed in a later section.

higher stress exponents have been attributed to damage inducing accelerated creep rates (Lin and Becher 1991, Arellano-Lopez et al. 1993). The effect on the strain rates is not clear. They are found to be sometimes lower (Porter 1988, Arellano-Lopez et al. 1993) and sometimes higher (Arellano-Lopez et al. 1990 and 1993) than in pure alumina. In any case, the strain rates do not change (lower or higher) by more than a factor of 4 with respect to the monolith. The lower creep rates have been attributed to inhibition of grain boundary sliding by the whiskers and the rotation of whiskers within the matrix (Porter 1988, Wilkinson and Pompe 1997). The observed higher creep rates in the low volume fraction composites have been rationalized by a larger diffusion path due to a larger average grain size in the alumina matrix (Arellano-Lopez et al. 1990) or by an increase in the diffusivity due to glass formation.

Higher whisker loadings (≥15%). The composites lead to continuously decreasing creep rates with time (i.e., the composites become stiffer with deformation), they have lower failure strains and consistently achieve lower strain rates (up to 2 orders of magnitude) than those of the unreinforced alumina (Chokshi and Porter 1985, Lin and Becher 1990, Arellano-Lopez et al. 1993). The absolute creep rate is found not to be strongly dependent on whisker concentration (Arellano-Lopez et al. 1993). Some studies (Lin and Becher 1991) have even found that 30 and 50%-whisker reinforced aluminas exhibit essentially identical creep properties. These observations suggest that the factors controlling the creep rates are independent of whisker content above a certain critical volume fraction. As mentioned before, the existence of two stress regimes is often found: consisting of a changing stress exponent from n=1-2 at low stresses, to n=2.5-7 (Nutt et al. 1990, Lin and Becher 1990, Arellano-Lopez et al. 1993) for stresses larger than a critical stress, σ_c which appears to depend on the origin of the sample, the temperature and the testing atmosphere. Cavity nucleation and growth start to be important at stresses near σ_c. Also, the values of σ_c tend to be lower in tests performed in air than in tests in an inert atmosphere probably because of degradation of the SiC whiskers (Arellano-Lopez et al. 1993).

The general consensus (Liu and Parvizi-Majidi 1990, Lipetzky et al. 1991, Swan et al. 1992, Arellano-Lopez et al. 1993) is that the creep mechanism at low stress level is due to diffusional creep and grain boundary sliding. However, the precise deformation mechanisms are not fully understood. The reinforcing effect of the whiskers has been attributed to pinning of the grain boundaries and, therefore, inhibition of grain boundary sliding, the principal plastic deformation mechanism in fine grained alumina at low stresses.

Arellano-Lopez et al. (1993) characterized the n=1 regime. On a compression test at 1400°C, a 20% SiC reinforced alumina sample the stress was increased and then decreased from one apparent steady state to another. These results are shown in Figure 2.10, the loading sequence is numbered and could be fitted to a single straight line, thus providing evidence that true steady state was achieved. No cavities or damage were observed in a sample deformed only in the n=1 regime (tested in flowing argon). The hypothesis is that the whiskers impede the sliding of the grains. The sliding becoming slow as to have a change in the creep mechanism from grain boundary sliding to pure diffusion. Supporting this idea was the study of the evolution of the grain form factor: 4π(grain area)/(grain perimeter)^2. A reduction of 13% of the mean value of the form factor was detected with no change in the average grain size in a sample deformed 15%. Since the stress exponent, n=1, in this sample (20% SiC) was different than the one obtained for the 5% SiC one, n=2, it was concluded that sufficiently high concentrations of whiskers can reduce creep rates in compression and can cause the creep mechanism at low stresses to change from grain boundary sliding to pure diffusional creep of the grains. A similar result was found by Lin and Becher (1991), at 1300°C a 10% SiC composite had a stress exponent n=4 whilst the 20% composite stress exponent was n=2.

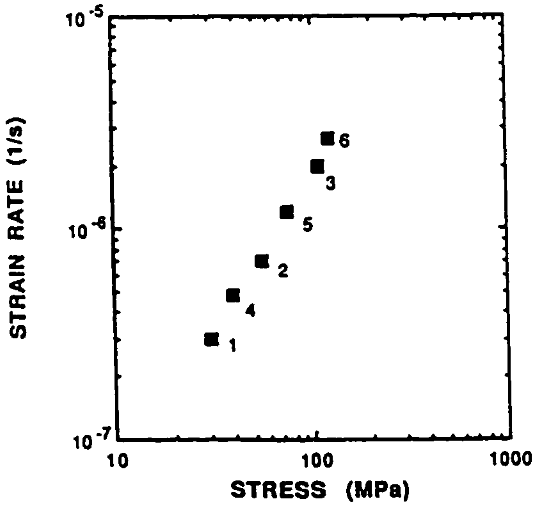

Figure 2.10. From Arellano-Lopez et al. (1993). Shows strain rate vs stress for the same sample. The loading sequence is numbered.

In general, the SiC whiskers can be considered stiff with respect to the alumina matrix at the testing temperature (Arellano-Lopez et al. 1993, Wilkinson and Pompe 1997). The assumption of stiff whiskers is based on the stress levels, the diffusion coefficients, and partly on the structure that has been reported for SiC whiskers (Arellano-Lopez et al. 1993). Whiskers are highly defective, containing immobile partial dislocations, systematic stacking faults, and core inclusions (Nutt 1984) making plastic deformation unlikely. Also, microstructural observations (Lipetzky et al. 1991, Arellano-Lopez et al. 1993) have not detected evidence that would suggest that SiC whiskers undergo plastic deformation. Thus the plastic response of the composite is mainly controlled by the alumina.

Porter (1988) has suggested that the additional creep resistance in the composites may result, at least in part, from the development during processing of a network of SiC whiskers. This network must be deforming in parallel with the matrix during creep. In high reinforcement loadings (>15%) the whiskers are not free to rotate, as a result of entanglement, and the network and can deform elastically upon loading. The hypothesis that the creep response is controlled in part by the formation of a whisker network was tested by Gu et al. (1994). They conducted anelasticity experiments using monolithic alumina and alumina/silicon carbide composites reinforced with 15% whiskers with different aspect ratio. At 1500°C, a load was applied for a selected period of time, then removed for an a additional period of time, and then reloading to the original level three or four times. Their results are shown in Figure 2.11.

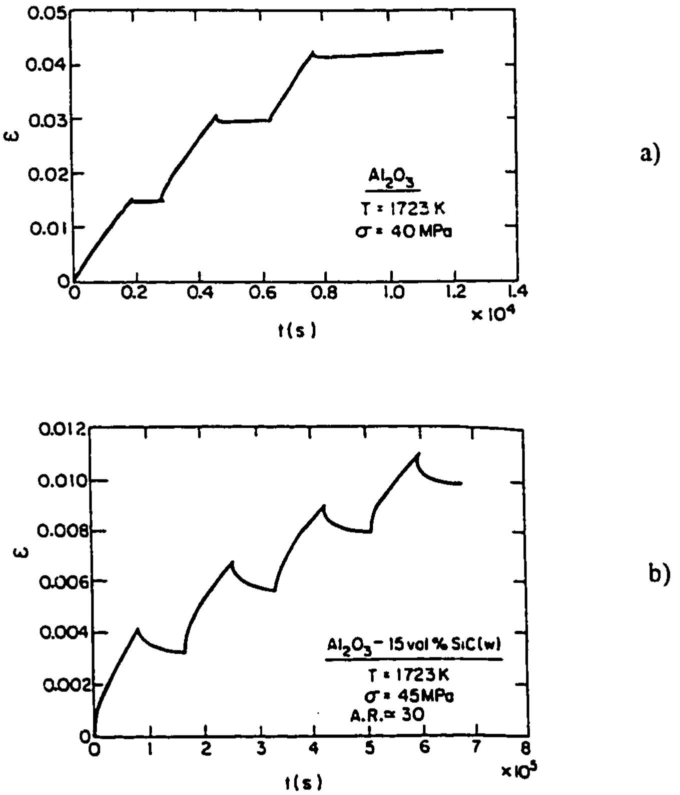

Figure 2.11. Strain vs time plats for a)monolithic alumina and b) alumina/SiC-w composite (high aspect ratio whiskers) (Gu et al. 1994).

The monolithic alumina exhibited no anelastic recovery, while a very similar anelastic response was found in the composite having whiskers with the smaller aspect ratio (10). However, there was a significant anelastic recovery following load removal in the composites reinforced with the higher aspect ratio (30) whiskers. The magnitude of the anelastic recovery was essentially independent of the total creep strain at which the load was removed. These results are consistent with the hypothesis that an interconnecting network of whiskers develops during processing and that the strain recovery observed on load removal had to be accumulated in the whisker network by the elastic bending of whiskers.

Since preferential orientation of the whiskers on planes perpendicular to the direction of compression occurs during hot-pressing, the elastic response of the whisker network must be different parallel to the hot pressing axis (HPA) than perpendicular to the same axis. If the elastic loading of the whisker network is an important part of the creep response, then there must be a different creep response according to the orientation of the samples. However, no significant effect of orientation has been detected for creep properties (Swan et al. 1992). Obviously, this does not prove that the network elastic loading is not an important part of the creep rate decrease. It could be that the whisker network in the experiments of Swan et al. (1992) with 30% whiskers is well developed parallel and perpendicular to the HPA and no difference in creep response might be expected.

Role of interface and oxidation.

Under creep conditions, the mechanical response of ceramic composites is strongly affected by the strength of the interfacial bond between reinforcement and matrix and the chemical stability of the interface. The presence of glass films, in particular, weaken the internal boundaries and increase grain boundary diffusion rates, which contribute to accelerated creep rates. Possible sources of the amorphous phase observed in crept samples include redistribution of residual sintering aids (such as MgO, Y_2O_3, and CaO) and native oxide surface films on the SiC whiskers. However, the amount of glass arising from these sources is apparently much smaller than the amount formed by thermal oxidation of SiC whiskers (Lipetzky et al. 1991). Thus, it is mainly the oxidation reactions which occur during creep, primarily in air ambient, that degrade the interface properties, leading to cavitation and damage (Nutt et al. 1990).

When an alumina-silicon carbide composite is exposed to an oxidizing environment, SiC will oxidize. The oxidation reaction can be expressed as follows (Luthra and Park 1988):

$$\mathrm{SiC(s)} + \frac{3}{2}\mathrm{O_2(g)} \rightarrow \underline{\mathrm{SiO_2}}\mathrm{(s,l)} + \mathrm{CO(g)} \qquad (2.12)$$

The underline beneath SiO_2 indicates that it can exist as either mullite or an aluminosilicate liquid. The formation of mullite can be expressed as:

$$\mathrm{2SiC(s)} + \mathrm{3Al_2O_3(s)} + \mathrm{3O_2(g)} \rightarrow \mathrm{3Al_2O_3 \cdot 2SiO_2(s)} + \mathrm{2CO(g)} \qquad (2.13)$$

The reactions are written in terms of O_2(g) and CO(g). It does not mean that they are present as gaseous species at the reaction site or that oxygen diffuses as a molecular species (Luthra and Park 1988). Oxidation can occur either by inward diffusion of oxygen through the oxide or by outward diffusion of aluminum or silicon. If the reaction occurs by oxygen diffusion, carbon present will oxidize, forming CO, which can migrate out through the reaction products as CO gas bubbles. If the reaction occurs by the outward diffusion of aluminum or silicon, deposition of carbon could occur. As has been observed in Al_2O_3/SiC composites (Lin et al. 1988). If the reaction was occurring by the outward diffusion of aluminum, the oxidation product would be enriched in silicon at the interface between the reaction product and the unreacted composite. No such enrichment was observed (Luthra and Park 1990). It is interesting to note that oxygen permeabilities through alumina, mullite and an alumino-silicate liquid are greater than through fused silica. Therefore, the rate of oxidation of a SiC particle in an alumina matrix is very fast compared with that of a SiC particle directly exposed to oxygen (Luthra and Park 1988). In the experiments performed by Porter et al. (1987), at 1500°C on 15wt% SiC-whisker reinforced alumina, the reaction kinetics (reaction layer thickness as a function of time) were parabolic, indicating that diffusion across a mullite reaction layer was rate-controlling. Lin and Becher (1990) observed that during long term exposure to air at elevated temperatures, the glassy phases formed on exposed surfaces could migrate to near surface grain boundaries of alumina composites. This was particularly important above 1400°C.

Lipetzky et al. (1991) made a comparison of creep data acquired in nitrogen and in air at 1300 and 1400°C. They showed that, although the stress exponents were similar, the strain rates were significantly higher for tests conducted in the oxidizing ambient. The stress vs strain curves that they obtained are shown in Figure 2.12.

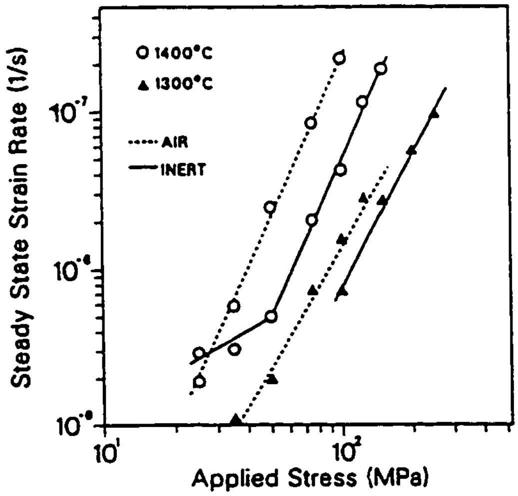

Figure 2.12. Effect of an oxidizing environment on the creep strain rate (Lipetzky et al. 1991).

The strain rates increased by factors of three for tests performed at 1300°C, while specimens tested at 1400°C in air showed a five-fold increase in strain rate compared with those crept in nitrogen. The primary microstructural difference between specimens crept in air and those tested in nitrogen was the quantity of glass phase, being more abundant in the air-tested samples. Cavities were detected at the same type of locations, at triple grain junctions and at sites of whisker-whisker contact, in both air-tested and nitrogen-tested samples. However, when the glass phase was far more prevalent the cavities were larger. Lipetzky et al. (1991) suggest that the most important effect of the oxidizing ambient on creep was the role of the vitreous phase in facilitating diffusion and cavitation. The formation of cavities at grain-boundary-interface junctions and at triple grain junctions allowed matrix grains to partly overcome the pinning effect of the whiskers and thus slide without accommodation. The widespread cavitation enhanced by the abundance of glass phase accounted for the increase in strain rates in air. It was concluded that the air-tested samples deformed by diffusional creep and that the boundary sliding was frequently unaccomodated, resulting in extensive cavitation.

Wilkinson-Pompe model for particulate-reinforced ceramic/ceramic composites.

The addition of second phase particles to a ceramic matrix will alter the creep response of a material. The scale of the effect depends on characteristics such as the volume fraction and morphology of the reinforcing phase (Wilkinson, 1997). Wilkinson and Pompe (1997) developed a series of models for the creep and anelastic recovery of whisker- and platelet-reinforced ceramics. These models help to explain the increase in creep resistance and the anelastic recovery observed in whisker-reinforced ceramics.

At low volume fractions, the particles behave essentially independent of each other and their effect can be mainly due to the local increase in effective diffusion path. Thus a disturbance of the flow field around the particles occurs (Wilkinson, 1997). Wilkinson and Pompe (1997) modelled the mechanism responsible for the decrease in creep rate based on the unconstrained rotation of particles (whiskers or platelets) in a viscous matrix. The creep rate of the composite is then limited by the slow rotation of the particles. The particle reinforced solid is considered as a two phase material formed by:

1) The matrix far from the particles, which exhibits a relatively small viscosity η_o.

2) The regions near the particles which are constrained locally, leading to a higher viscosity. In other words, a rotating particle and its associated matrix region with viscosity η_f are treated as larger particles with an associated volume fraction v_{con}.

The relationship between the constrained volume fraction v_{con} and the particle volume fraction ϕ is given by,

$$v_{con} = \left(\frac{\lambda}{2} \langle \sin 2\theta \rangle + \langle \cos^2 \theta \rangle \right) \cdot \phi \tag{2.14}$$

where θ is the angle between the particle's long dimension and the far-field stress Σ and λ is the particle's aspect ratio. This is depicted in Figure 2.13.

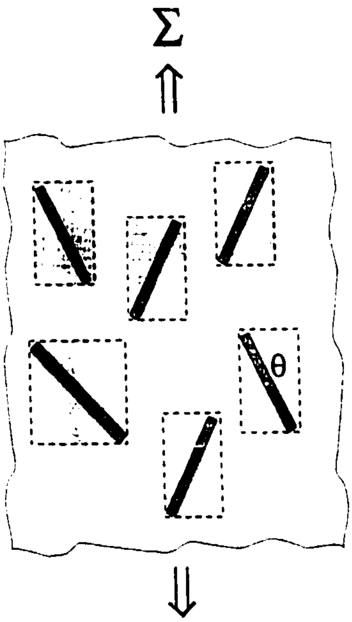

Figure 2.13. Schematic of low volume fraction composite (Wilkinson and Pompe 1997).

The creep strain rate, the far-field stress Σ, and the viscosity η, are related with

$$\eta = \frac{\Sigma}{3\dot{\varepsilon}} \tag{2.15}$$

The system is then described using a composite sphere model. The model predicts the effective viscosity of the composite to be

$$\frac{\eta_{reff}}{\eta_0} = 1 + 2.5 \frac{v_{con}}{1 - v_{con}} \tag{2.16}$$

The predicted increase in viscosity in the composite with respect to the monolith is never larger than a factor of two, which is consitent with the experimental results for low volume fractions summarized in previous sections.

At higher volume fractions, inter-particle interactions occur. When the particles are touching and form a continuous network, assuming that no significant damage occurs, then creep requires the deformation of the particle network in accord with the matrix. The creep was modeled by viscoplastic creep, in which the matrix material is squeezed from within regions of near contact; and viscoelastic creep in which the particles bend in response to the non-uniform loading applied by contacting particles. This predicts substantial anelastic effects whenever viscoelastic creep is the dominant mechanism, which has been observed in previous studies e.g. Gu et al. (1994). Assuming that the particles lie on, or close to, a set of parallel planes forming a regular network, for viscoplastic creep the viscosity is given by

$$\frac{\eta_{vp}}{\eta_o} = \frac{2(1+f)}{k_p \lambda^2 f}\left[\left(\frac{f^2}{\phi}\right)^{1/3} - 1\right]^{-3} \qquad (2.17)$$

where f is the packing efficiency of the particles (for f=1 the spacing between particles is proportional within and between layers, i.e. ideal) and k_p is a stress concentration factor. For viscoelastic creep matters are complicated by the time dependence. But the average viscosity at zero strain is found to be

$$\frac{\eta_{ve}}{\eta_o} = \frac{16}{\pi^4 k_p (f\phi)^{1/3}} \qquad (2.18)$$

These results are summarized in Figure 2.14 where the normalized viscosity is plotted as a function of the volume fraction and the packing efficiency for the three mechanisms. The model predicts more modest decreases in viscosity than those found in the experimental data for SiC-whisker reinforced Al_2O_3. Nevertheless, it predicts the changes in creep resistance as the structure changes (with the parameter f); and thus the evolution of contacts and constrains as the deformation increases; which stiffen the composite as the strain increases.

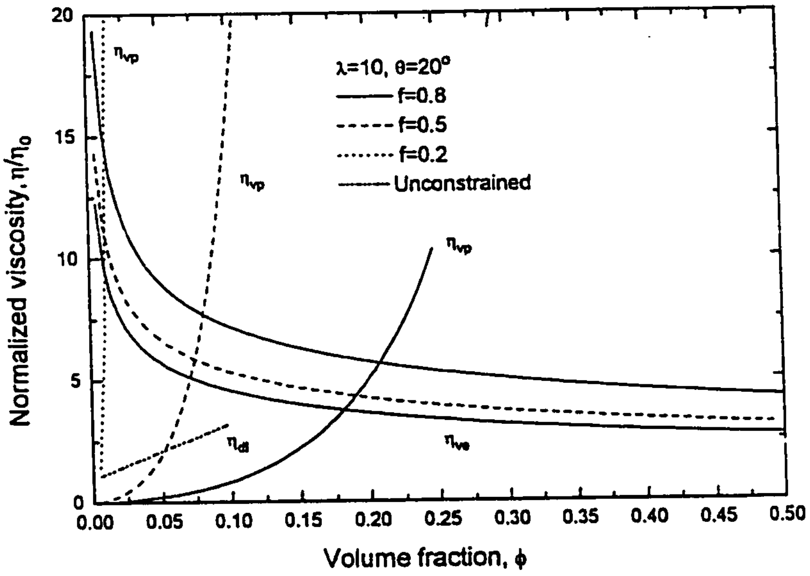

Figure 2.14. Normalized viscosity as a function of volume fraction and packing efficiency (Wilkinson and Pompe 1997).

2.4. Summary.

The Literature Review covers the main background material for this work. It was divided in two parts. In the first one, Processing, a general physical description of colloidal dispersions, an introduction to the fundamentals of rheology and its use to optimize slurry formulations, and a review on tape and slip casting techniques were given. These topics are relevant to the fabrication of the composites and monolithic materials. The second section, Creep of SiC reinforced Al_2O_3, principally gives an overview of the creep behaviour of SiC-whisker reinforced ceramics. It contains the topics that are often addressed to later on in the present work. Not all the utilized literature has been mentioned here as it was felt it would deter from the main purpose of the chapter. Rather, that literature is mentioned or summarized when it is immediately relevant in subsequent chapters.

3. MATERIALS DEVELOPMENT.

3.1. Introduction.

This chapter describes the relevant characteristics of the commercial powders used, the four different green fabrication procedures, and the sintering of the ceramic samples. The materials' characteristics were tailored to study the influence of platelet additions to alumina on the creep behaviour. With the desire to minimize doping, no sintering additives were used. Normally, MgO additions to monolithic polycrystalline Al_2O_3 prevent abnormal grain growth, in the case of Al_2O_3/SiC-whisker composites, the whiskers perform a similar function (Porter 1988) and it was expected that the platelets would perform the same role in the high SiC volume fraction composites. The following volume fraction composites were fabricated: *0 vol%* as control, i.e. for comparison purposes, *5 vol%* -a low volume fraction where interactions between particles would be minimized, *15 vol%* where particle-particle interactions were likely to happen, and *30 vol%* for which strong interaction between reinforcement particles were expected. Composites with different platelet textures were fabricated as the matrix-particle and particle-particle interactions will change depending on the orientation of the platelets with respect to the applied stress and on the morphology of the particle network.

3.2. Powder characterization.

A commercial α-alumina from Alcoa[1] and commercial silicon carbide platelets from C-axis Technology[2] were used in this work. The Al_2O_3 powder was used for the preparation of the monolithic samples as well as the composites matrix, the SiC platelets were used as the reinforcing phase. The particle size distribution in the alumina powder was measured by an optical transmission method[3] (OTM). The distribution is shown in Figure3.1. The alumina exhibits a relatively narrow size spread although it is bimodal, likely due the presence of hard agglomerates (2-4μm in diameter). In the case of the silicon carbide platelets, the OTM was not used. The analysis assumes spherical particles thus the method does not

---

[1] Alcoa-A16SG, Alcoa, Pittsburgh, Pennsylvania, USA.
[2] SiC-SF, C-axis Technology Ltd, Montreal, Quebec.
[3] CAPA-700, HORIBA particle size analyzer, SSCAN, Richmond Hill, Ontario.

yield reliable results for very anisotropic particles, such as platelets and whiskers. The average SiC platelet diameter and aspect ratio (AR) were estimated from SEM images such as the one shown in Figure 3.2. The specific surface area of the alumina and silicon carbide powders were measured by the BET (Brunnauer-Emmet-Teller) nitrogen gas absorption method[4] These results, along with the theoretical density are given in Table 3.1. The manufacturers' reported compositions for the powders as well as the results of the composition analysis of the platelets performed at McMaster University are shown in Table 2. The amount of SiO_2 present in the platelets was estimated from the measured oxygen content, via a LECO[5] analysis, assuming that all of it is forming silica on the platelets' surface. This is not strictly correct as the other impurities could be in oxide form, thus the silica amount must be somewhat overestimated. The rest of the composition was determined by x-ray fluorescence analysis.

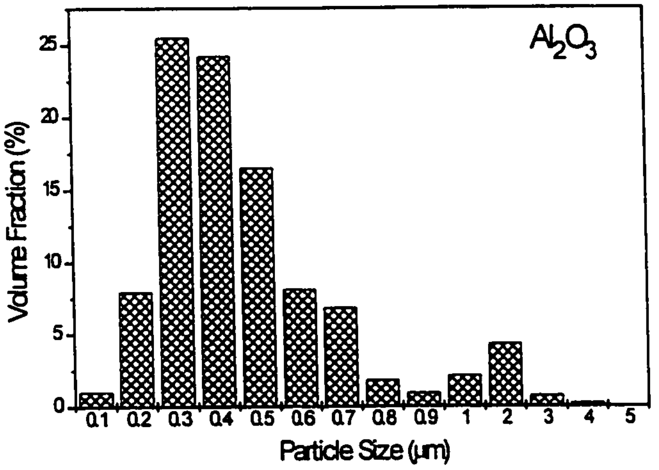

Figure 3.1. Alumina particle size distribution.

---

[4] Autosorb-1, Quantachrome Co. Syosset, New York, USA.

[5] N_2/O_2 determinator, TC-136, LECO Instruments Ltd, St Joseph, Michigan, USA.

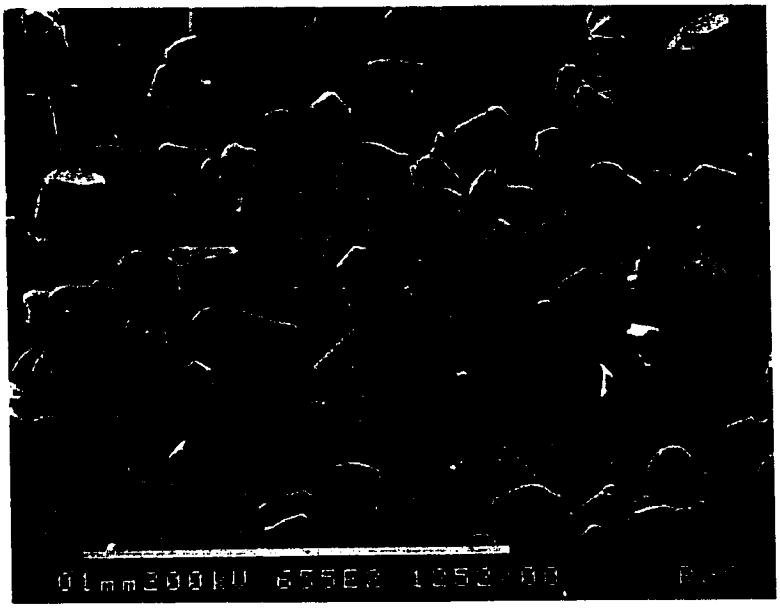

Figure 3.2. SiC platelets micrograph.

Powders	Theoretical density (g/cm^3)	Average particle size (µm)	Surface Area (m^2/g)
Al_2O_3 (Alcoa A16-SG)	3.98	0.37	10.17
SiC (C-Axis Tech. SF)	3.21	14* diameter 20#, aspect ratio 10#	0.43

* Manufacturer's value.

\# Estimate from SEM micrographs.

Table 3.1. Physical characteristics of starting powders.

	Alumina powder*	Silicon carbide platelets*	Silicon carbide platelets[#]
Al_2O_3	99.95		
O_2		0.183	0.187 ±0.012
SiO_2	0.025	~0.50[@]	~0.52[@]
Mg		<0.005	0.011 ±0.003
Al		0.62	0.20 ±0.02
P			0.26 ±0.03
Cl			0.017 ±0.003
Ca		0.011	0.17 ±0.02
Fe		0.018	-----
Ti		0.001	-----
Ni		0.004	0.008 ±0.003

* Manufacturer's data.
[#] Data obtained at McMaster University.
[@] Estimate from oxygen content.

Table 3.2. Composition of starting powders (wt%).

At high temperatures, a layer of glass at the alumina/SiC interfaces is very likely to promote cavitation and provide a rapid diffusion path for atomic species making it detrimental to the creep properties. The more extensive this layer, the more detrimental. It was desired to diminish the volume of such glass layer as much as possible. This glass is usually formed mainly from the oxidation of the SiC surface into silica and carbon oxides ($2SiC + 3O_2 \rightarrow 2SiO_2 + 2CO$) during manufacturing of the SiC or afterwards during processing of the composites and its combination with the matrix to form alumina-silicate glasses (Al_2SiO_5). Malghan et al. (1991) found that if the reinforcement is coated with a silica layer it is possible to clean it to a certain extent via an acid wash that attacks and removes the amorphous layer. Thus some of the SiC platelets (SF C-Axis Tech.) were subjected to an acid wash similar to that one of Malghan et al. (1991), the oxygen content decreased from 0.187 wt% to 0.169 wt%, not a significant decrease. By comparison, in another class of SiC platelets (SC-21 C-Axis Tech.) with an as manufactured oxygen content of approximately 1 wt% (Bloyce 1993), the oxygen content was decreased to 0.2 wt% by an acid wash. There are other possible benefits from the acid cleanse. It could remove surface contaminants that would promote lower viscosities in a glass layer, such as Ca. However, x-ray fluorescence analyses were done on the platelets before and after acid cleansing with no measurable change in impurities. Thus it was decided to fabricate the composites with as-manufactured platelets.

Silicon carbide is manufactured by a carbothermic reduction process in which silica and carbonaceous materials are reacted at high temperature (Nutt 1988). The structural types are generally classified into cubic (β) and hexagonal or rhombohedral (α) phases and exhibits a number of polytypes (Park et al. 1994). These consist of identical layers whose stacking sequences differ. Hundreds of distinct stacking sequences have been reported in SiC crystals, some of which require lattice constants of up to 1500Å (Knippenburg 1963, Kingery et al. 1976). The commonly used Ramsdell notation (Nutt 1984) consists of a number, representing the number of closed-pack layers of silicon and carbon atoms in the unit cell followed by a letter denoting the Bravais lattice type (C for cubic, H for hexagonal and R for rhombohedral) e.g. 2H, 3C, 1200R, etc. Figure 3.3 shows a schematic of some of the SiC polytypes.

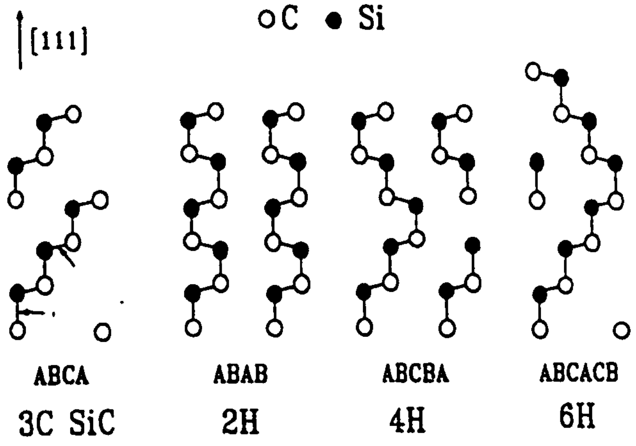

Figure 3.3. Atomic structures of some of the SiC polytypes. A, B and C denote the type of atomic layer, the [111] cubic or [001] hexagonal is vertical (Park et al. 1994).

The crystallography of the silicon carbide platelets was characterized using x-ray diffraction and neutron-diffraction[6] before and after different thermal treatments. This was aimed to test the phase

---

[6] Performed at AECL, Chalk River Laboratories, Chalk River, ON.

stability of the platelets during sintering and subsequent thermal treatments, as any phase change could affect the internal strains of the composites and thus the mechanical behaviour. The two main heat treatments were:

1) An anneal under vacuum at 1650°C for 1 hour, which intended to mimic the sintering conditions of the composites and,

2) an anneal under vacuum at 1825°C for 5 hours, which intended to transform any β phase into α and maybe form more 4H as that structure has been found to be the most stable (Park et al. 1994).

The platelets are α-phase with the c-axis perpendicular to the platelet plane, their phase or polytype did not change during heat treatment. They are composed of approximately 66% (all percentages will be in volume percent, unless otherwise specified) 4H and 33% 6H. However, the presence of other polytypes was confirmed by high resolution electron microscopy. From the literature, reported mechanical properties of SiC platelets include an elastic modulus of 470GPa, a Vickers hardness of 30GPa and a failure stress that exceeds 3GPa (Claussen 1990).

3.3. Processing.

3.3.1. Tape casting.

In the present work, the tape cast slurry formulation was based on that by Burger et al. (1990). Several modifications were made to suit the particular needs and to obtain a more reproducible forgiving process. The possible solvents are selected based on the solubility of binder, plasticizers and possible dispersants, as well as a low boiling point and heat of vaporization. The latter favours the use of non-aqueous solvents (Roosen 1988). Often more than one type of solvent is needed to enable solution and uniform distribution of the plastics within the slurry. An azeotropic mixture of solvents avoids preferential volatilization and prevents the formation of a polymeric skin on the surface of the tapes during drying (Plucknett et al. 1994a). The majority of published non-aqueous tape casting formulations employ either mixtures of trichloroethylene (TCE) and ethanol with menhaden fish oil[7] as a dispersant (e.g. Shanefield and Mistler 1974, Mistler et al. 1978, Burger et al. 1990), or mixtures of methyl ethyl ketone (MEK) and ethanol with either menhaden fish oil or phosphate esther as a dispersant (e.g. MacKinnon and Blum 1984,

---

[7] Merck Index (5660). Pogy oil, mossbunker oil. Obtained along the east coast of North America from the Menhaden fish (Brevoortia tyrannis) somewhat larger than a herring. The oil contains glycerides about 6% myristic acid, 16% palmitic acid, 30% linoleic acid, 19% C_{20}- and 11% C_{22} acids (highly unsaturated). Reddish oil. Characteristic distateful fishy odour and taste. Density 0.925-0.933.

Boch et al. 1986, Chartier et al. 1988, Portu et al. 1988). Plucknett et al. (1994a) compared the two dispersants and the two solvent systems. Considerable variations were found for the dispersion properties in two menhaden fish oil batches, attributed to seasonal and locational variations in composition and degree of oxidation. Phosphate ester was found to be more consistent and thus chosen as dispersant. In addition, they concluded that the combination TCE/ethanol allowed for larger changes in dispersant level without a significant effect in the slurry viscosity. Thus, an azeotropic mixture of trichloroethylene and ethanol was employed as solvent and phosphate esther[8] as dispersant in tape cast slurry formulation in this work.

The best dispersion and the highest slip stability is obtained with the amount of dispersant that gives rise to the lowest viscosity for a given shear rate. This optimum amount of dispersant was determined by the rheological behaviour of mixtures of Al_2O_3 powder, the azeotropic solvent mixture of TCE/ethanol and different amounts of phosphate esther. The mixture does not include the binder and plasticizers, as it has been found that their later addition does not affect the location of the minimum in the viscosity vs dispersant concentration curve (Roosen 1988, Plucknett et al. 1994a). The viscosity of the Al_2O_3/TCE/ethanol/phosphate ester slurries was measured using a concentric cylinders viscometer[9]. A relatively high solids loading (45-50 %) was needed in order for the slurry to have a high enough viscosity to be accurately measured by the instrument. The mixtures presented shear-thinning behaviour, as shown in Figure 3.4. The amount of dispersant required was found to be 3 to 4 % in an alumina slurry (Bloyce 1993).

---

[8] Emphos PS-21, Witco Canada Inc, Ontario.

[9] Bohlin Visco 88 BV, Bohlin Rheologi, Inc. Cranbury, New Jersey, USA.

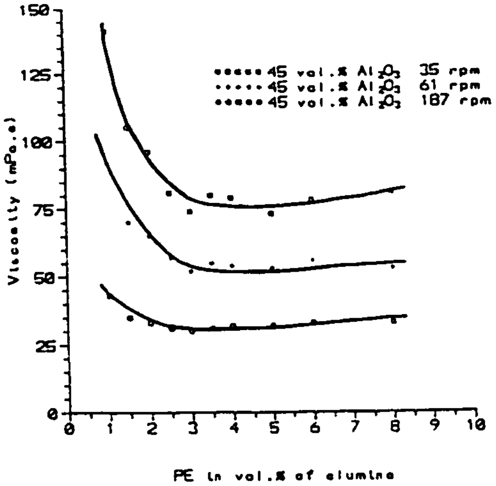

Figure 3.4. Viscosity vs vol% of phosphate esther (Bloyce 1993).

The rest of the tape casting slurry formulation was optimized by a trial-and-error process mainly based on the following criteria:

1) Prevention of particle segregation after casting and orientation of the platelets parallel to the glass surface. For this, the viscosity of the slurry should decrease as it flows beneath the doctor blade and increase relatively fast thereafter.

2) Obtainment of green tapes with an homogeneous microstructure and a relatively high density,

3) The green tapes should posses enough flexibility and strength for relatively easy handling.

All slurry formulations are shown on Table 3.3.

component	function	density (g/cm^3)	Al_2O_3 (%)	Al_2O_3/ 5% SiC (%)	Al_2O_3/ 15 % SiC (%)	Al_2O_3/ 30% SiC (%)
Al_2O_3	powder	3.98	25	23.8	21.3	18.1
SiC	powder	3.21		1.2	3.7	7.9
phosphate esther	dispersant	1.04	0.9	0.8	0.7	0.6
trichloroethylene	solvent	1.46	34.8	34.8	34.8	33.8
ethanol	solvent	0.79	25.2	25.2	25.2	24.5
polyvinyl butyral	binder	1.01	4.7	4.73	4.8	5.0
polyethylene glycol	plasticizer	1.13	4.7	4.73	4.8	5.0
dioctyl phthalate	plasticizer	0.98	4.7	4.73	4.8	5.0

Table 3.3. Slurry formulations for alumina and alumina/silicon carbide tapes.

It should be noted that different species in the suspensions can compete with the dispersant for the particle surface (Roosen 1988). To minimize the competition, the sequence in which the compounds are added becomes important. Thus solvent, dispersant and Al_2O_3 powder were first ball milled for 48 hours. This breaks most powder agglomerates and allows the dispersant to be adsorbed onto the surface. The binder and plasticizers were then added. The slurry was milled for another 24 hours to dissolve the plastics and obtain an homogeneous mixture. In the case of the composite materials, the platelets were added 12 hours after the binder and plasticizers had been added and then milled for 12 hours. This minimized platelet damage and ensured an overall milling time of 72 hours for composites and monolithic material. The milling steps are shown on the first part of the processing flow chart on Figure 3.5.

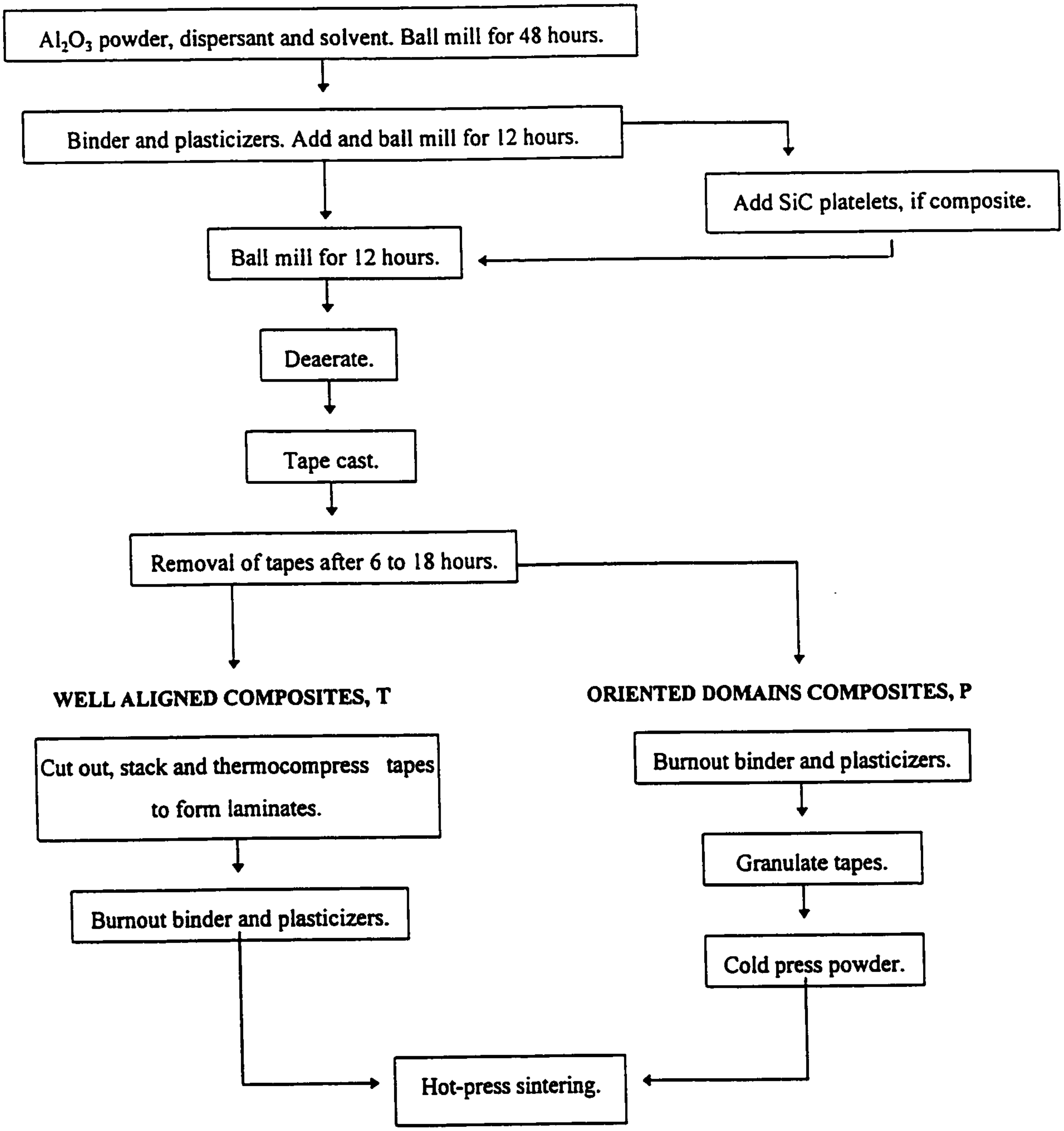

Figure 3.5. Tape cast processing flow chart.

After milling, the slurry is deaerated, i.e. for approximately 30 seconds a vacuum of 25 mmHg is applied to remove entrapped gas and avoid bubbles in the cast tapes. The slip is then transferred to the casting vessel. The tape casting system[10] consists of a mobile reservoir with dual doctor blades driven by a motor and a stationary casting surface of tempered glass. The blade speed was approximately 8mm/sec. The gaps between the glass casting surface and the edge of the blades were set to 400μm the first and 300μm the second. A schematic of the dual blade system is shown on Figure 3.6. The tapes were generally 150mm wide and 1m long. They were dried on the glass plate for 6 to 18 hours prior to removal. The dried tapes had a thickness average of 146μm ±7μm. The width (parallel to glass surface) drying shrinkage was negligible.

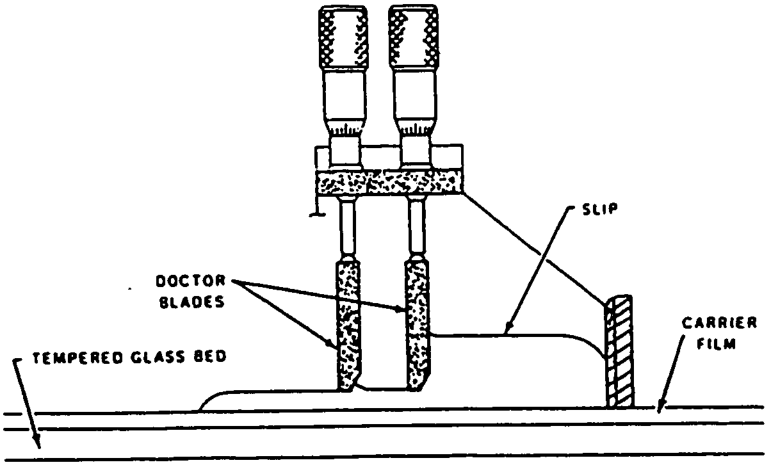

Figure 3.6. Dual doctor blade system (Mistler et al. 1978).

To fabricate composites with the platelets preferentially oriented, designated by T, the dried tapes were cut into 45x65mm rectangles. These were then stacked and thermocompressed to give laminates of various thicknesses. The tapes were thermocompressed under a 25mm Hg vacuum, at a temperature of 90-110°C and a pressure of ~33MPa using a hand press[11].

The dry tapes contain approximately 37% of organics. These have the temporary function to make the tape casting and laminating processes feasible but they must be expelled before sintering occurs. The large volume percentage of organics and the relatively high packing density (approximately 60% solids, 3% pores) of the green tapes requires a controlled burnout to avoid damage in the tapes.

---

[10] Model 133A, Cladan Inc, San Marcos, California, USA.

[11] 20 ton hand press, Model C, Carver Laboratory Press, Wisconsin, USA.

Thermogravimetric analysis (TGA) was performed on single layers of tape -of both the alumina and composite tapes- as well as on the SiC platelets powder. These results were used to determine the binder removal cycle. The TGA data was obtained using a constant heating rate of 5°/min, in flowing air to a maximum temperature of 1000°C. The TGA on the composites and on the SiC were done mainly to find the temperature at which the oxidation of the platelets starts to occur. It should be noted that the degradation of the organic phase occurs at slightly lower temperature when the heating rate is reduced (Scheiffele and Sacks 1988, Plucknett et al. 1994b). From the TGA on the 30% SiC/Al_2O_3 tapes (Figure 3.7) it can be seen that a very rapid volatilization of the organics occurs between 180 and 210°C. At 400°C approximately 93% of the organics have been eliminated from the tape and by 600°C, approximately 99% have been volatilized. Between 740 and 750°C a slight weight gain commences, probably due to oxidation of the platelets as this was not observed on the TGA of alumina tapes. The organics burnout cycle, for single tapes and laminates, was designed based on the TGA results, its schematic is shown on Figure 3.8.

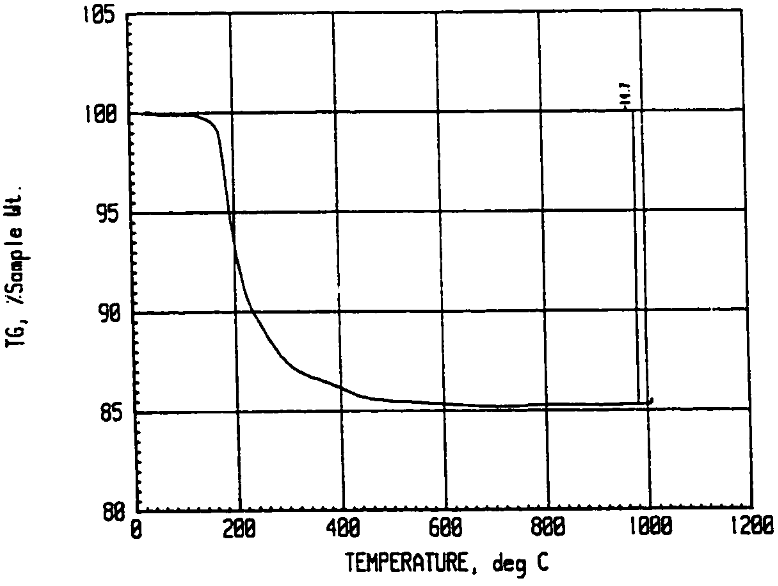

Figure 3.7. Thermogravimetric analysis of 30% SiC/Al_2O_3 single tapes.

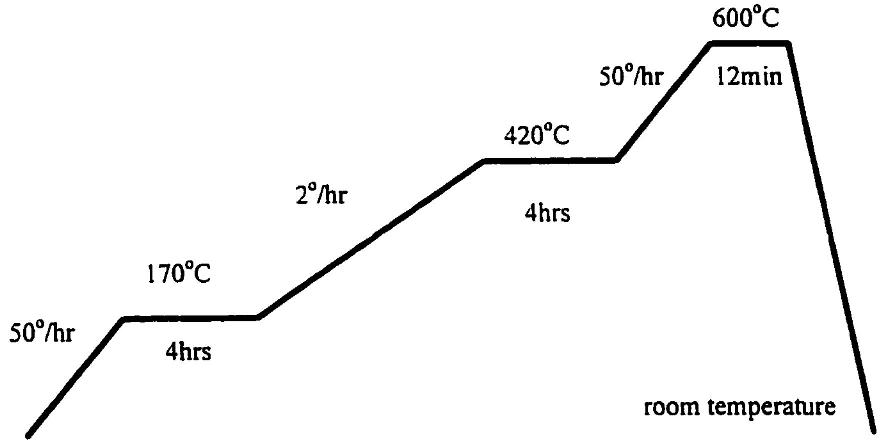

Figure 3.8. Organics burnout cycle.

The oriented domains composites, designated by P, were produced by bisque firing single tapes and then granulating them using a mortar and pestle. The resulting powder consisted of elongated Al_2O_3/SiC agglomerates of up to 150µm[12], with the platelets preferentially oriented in one direction within each granule. A micrograph of a typycal granule is shown on Figure 3.9. The size of the agglomerates was advantageous for cold pressing, as flowable powders require large particles (>50µm) because the separating force produced by differential acceleration during flow is proportional to particle mass (Lange 1989). After granulation, the powder was cold pressed at ~9MPa inside the hot-pressing die. The tape casting processing steps are summarized on Figure3.5.

---

[12] The granules' size estimate was done from SEM micrographs. It was not possible to asses the size distribution of granules by the OTM particle size analysis (used with the alumina powder) because the assumptions for the analysis are not realistic for the granules. The necessary assumptions are: each measured particle is a sphere, with no porosity (the granules are porous) and with the same density as the macroscopic composite (each granule would have important variations in density depending on its composition).

Figure 3.9. Al_2O_3/30% SiC agglomerate from granulated tapes.

3.3.2. Slip casting.

The slip casting procedure was based on those used by Porter (1989) to fabricate SiC-whisker reinforced alumina and Chou and Green (1992) to fabricate SiC-platelet reinforced alumina. Each phase was first dispersed in water by ball milling as this method is more efficient than ultrasonification in the break down of hard agglomerates (Sacks et al. 1988b). pH control was used to create a double layer on the particles' surface. Hence electrostatic repulsion was the stabilization mechanism. In the case of the alumina, the appropriate pH value was obtained from zeta-potential (ζ) measurements[13], the pH vs ζ plot is shown on Figure 2.4. These type of measurements require a minimum amount of particle horizontal displacement in suspension. Due to their relatively large mass, the SiC platelets tend to sink too rapidly making an accurate measurement of ζ impossible. Thus the pH value range to disperse the platelets was taken from literature values on SiC whiskers (Sacks et al. 1988a, Porter 1989, Smith et al. 1989). The slurry's solids loading was 30-35 vol%. A high pH (10-11) was used to disperse the silicon carbide platelets, obtained by ammonium hydroxide (NH_4OH) additions to the slurry. A low pH (2-3) was

---

[13] Zeta Meter System 3.0^+, Zeta-Meter Inc. Long Island City, New York, USA.

produced by nitric acid (HNO_3) additions and used to disperse the alumina powder. The milling time of the SiC was kept to a maximum of 1 hour to try and avoid mechanical damage of the platelets.

In order to fabricate randomly oriented composites, designated by S, it was desired to form alumina and silicon carbide granulates with the following characteristics:

1) each granule should have a random orientation of platelets and be approximately equiaxed.

2) the granules should be large (>50μm, Lange 1989) to be able to flow with relative ease when cold-pressed and thus obtain material with high final density.

For that purpose, the alumina and silicon carbide slurries were first combined in the proportions necessary to achieve the reinforcement volume fraction desired, then the pH was adjusted to a value of ~7.5 by adding ammonium hydroxide or nitric acid 0.1N solutions, and ball milled for 30 min. The processing steps are illustrated on the flow chart on Figure 3.10. Experimentally, it was found that heteroflocculation and alumina flocculation occurred at pH=7-8, where alumina particles become attracted to the SiC platelets and to each other. This is illustrated on the micrograph of Figure 3.11, which shows a platelet covered by alumina particles taken from an alumina-SiC slurry. It is interesting to note that the pH range for heteroflocculation seems not to be only a function of the materials involved since Porter (1989) found heteroflocculation occurring between alumina and SiC-whiskers at a pH=2 in similar suspensions.

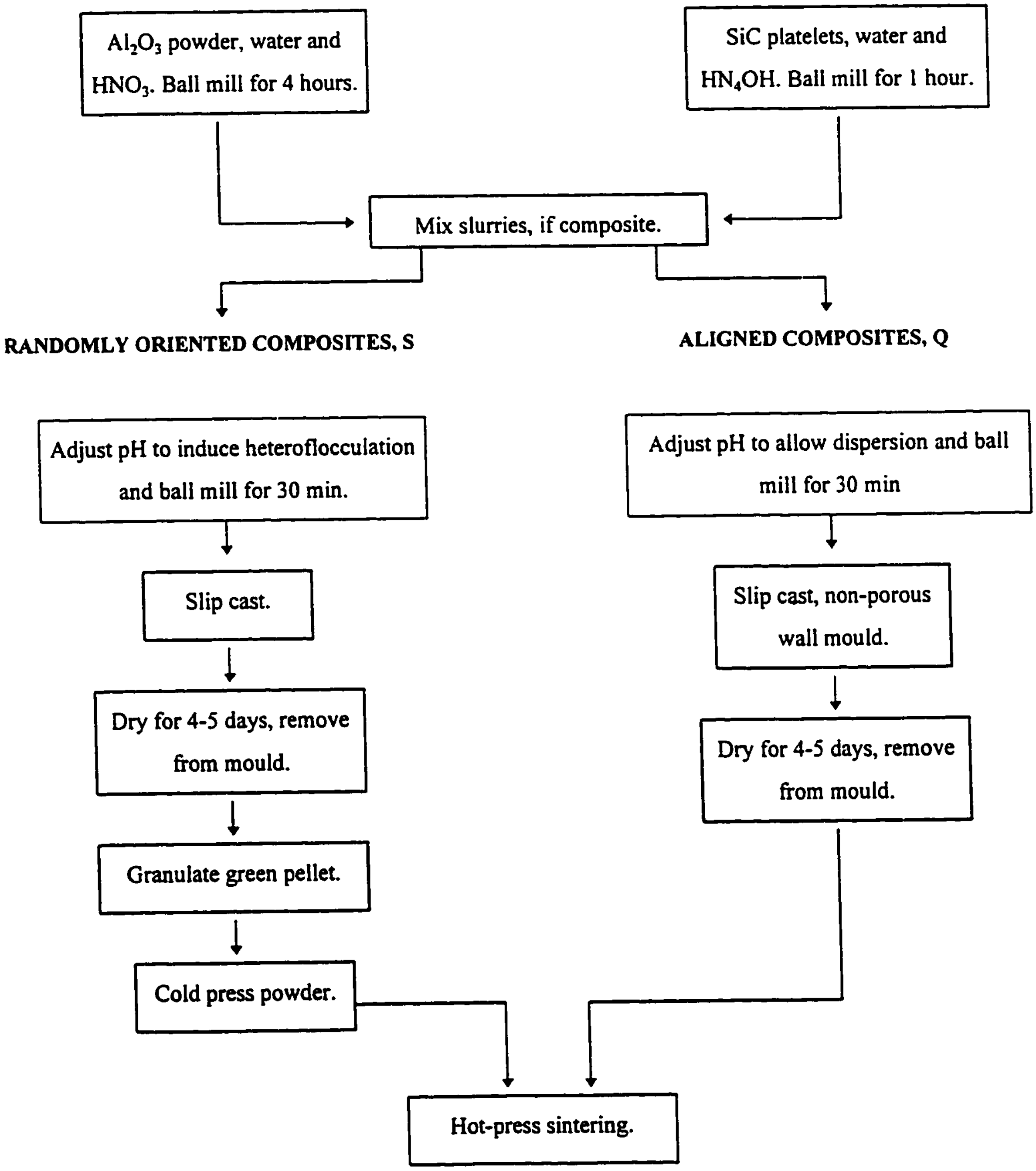

Figure 3.10. Slip casting processing flow chart.

Figure 3.11. Silicon carbide platelet covered with alumina particles. The very light, apparently flat, parts are due to charging effects on the sample and do not represent its actual topography.

The flocculated slurry, containing 20 to 35% solids, was then slip cast. The slip casting moulds were made of gypsum ($CaSO_4 \cdot 2H_2O$) which is usually used for reasons of its relatively low cost, ability to cast moulds with good surface smoothness, high ultimate porosity and small pore size and short setting time (Reed 1988). However, there are some disadvantages such as erosion due to their low abrasion resistance and the significant solubility of gypsum in water (Reed 1988). Therefore, contamination of the green bodies with gypsum is practically unavoidable. A few minutes after casting the slurry alumina or alumina and silicon carbide clearly sedimented. The cast slurry was allowed to dry at room temperature for 4-5 days. The green pellet was then easily removed from the mould and crushed using mortar and pestle into fairly equiaxed agglomerates of up to 100µm in diameter, Figure 3.12 shows an SEM micrograph of an Al_2O_3/SiC agglomerate. As with the tape cast granulates, the powder was then cold pressed at ~9MPa in the hot-pressing die.

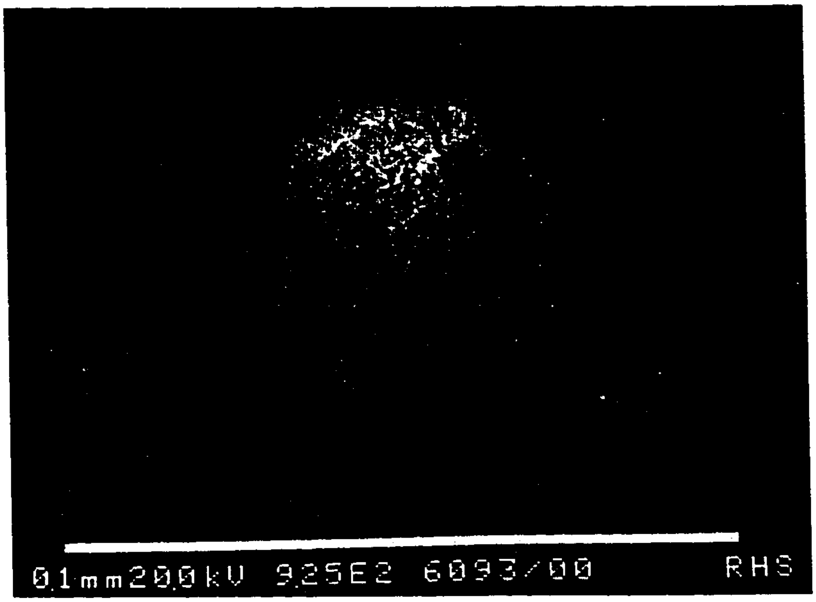

Figure 3.12. Granule from an Al_2O_3/30% SiC powder.

The flow diagram (Figure 3.10) illustrates the steps followed to make the aligned composites, designated by Q. The Al_2O_3 slurry and the SiC slurry were mixed in the proportions necessary to obtain the desired volume fraction in the composite. Then the pH of the mixture was adjusted to 4 by nitric acid or ammonium hydroxide solution additions as at this pH both components showed good stability. The slurry, constituted of 25-35 % solids, was ball milled for 30 min before casting.

When platelet-containing slurries are cast, the platelets tend to orient parallel to the porous mould surfaces (Chou and Green 1992, Selçuk et al. 1995) due to the outward liquid flow. Near the porous mould walls a layer of well oriented platelets is formed. Towards the central region of the sample the liquid flow occurs towards all porous surfaces making the platelet orientation more chaotic. To achieve good platelet alignment Selçuk et al. (1995) utilized a mould with 2 long and 2 short porous walls and a non porous support so as to obtain bar-shaped samples with platelets aligned parallel to the long walls. The resulting alignment was fairly good with the majority of platelets within 30° of the mould's walls. However, in the central section of their samples the platelets formed a V shaped orientation profile with a number of them forming high angles with the mould's walls. In the present work, the aligned Q samples were fabricated using a casting mould with a porous bottom, made of gypsum, and a non-porous cylindrical wall, Figure 3.13 shows the schematic. The cylinder wall was lined with teflon to avoid wetting.

This facilitated the separation of the sample from the wall while drying and shrinking, thus preventing the occurrence of cracks in the dried green pellet.

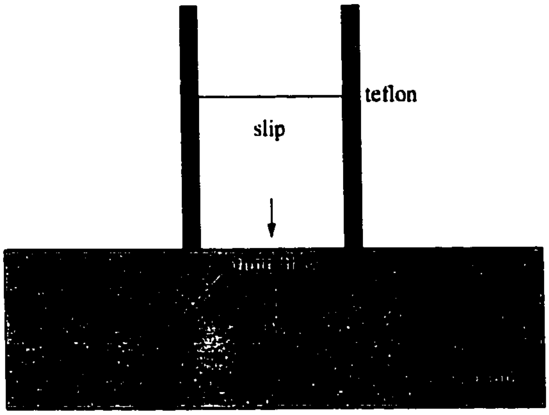

Figure 3.13. Schematic of plaster mould used for aligned composites, Q.

3.3.3. Sintering.

It was desirable to have a relatively large size difference between the platelets and the matrix grains as the increase in effective diffusion path is likely to be an important creep resistance mechanism. However, the matrix grain size was not to be as small as to allow significant grain growth during high temperature testing. Thus the sintering temperature varied depending on the sample SiC loading in order to obtain a grain size of approximately 2.5μm. Table 3.4 lists the different sintering temperatures depending on the SiC-platelet volume fraction. All samples were hot pressed[14] in a graphite die, under a vacuum of $8x10^{-2}$torr. The hot-pressing cycle consisted of a 1hr 30min to 1hr 45min ramp to the sintering temperature dwell of 1 hour where a pressure of 66MPa was applied, the load was removed at the start of the cooldown. A typical cooldown cycle is shown in Figure 3.14. The actual temperature of the sample likely lagged behind the monitoring temperature as the thermocouple was external to the graphite die which insulated the sample. Some of the microstructures are shown in Figures 11 and 12. The ceramic pellets (66mm diameter or 45x65mm of variable thickness) were machined into 4x3x45mm bars for flexure creep tests and

---

[14] 50 ton hot press, Electrofuel Mfg. Co. Toronto, Ontario.

4x3x8mm bars for compression creep tests to a surface finish according to the C1161-90 ASTM standard. The 3mm dimension was taken parallel to the hot-pressing direction.

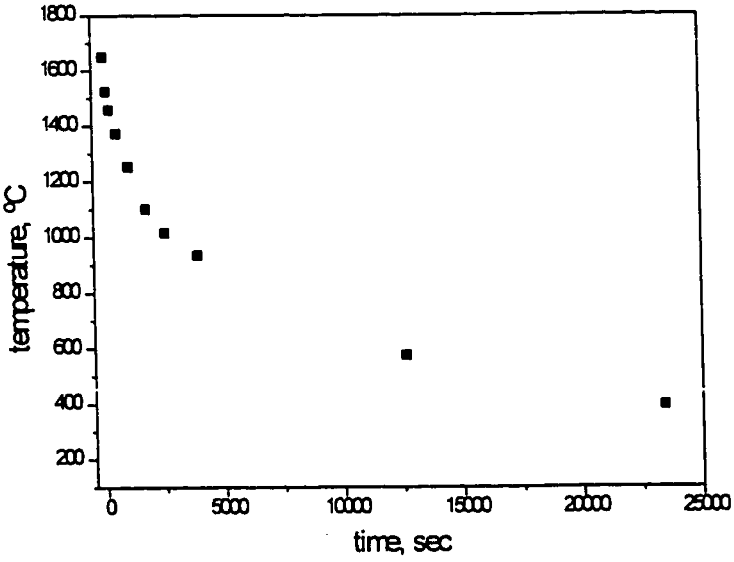

Figure 3.14. Cooldown cycle from 1650°C.

SiC %	Sintering temperature, °C
0	1590
5	1580
15	1560
30	1650

Table 3.4. Sintering temperatures.

3.4. Summary.

Silicon carbide-platelet reinforced alumina composites were fabricated by various processing methods with different volume fractions. Table 3.5 lists the samples method of fabrication and their short designation name which is used in future chapters.

composite, SiC vol%		designation
granulated slip cast, 30	random	S30
tape cast, 30	well aligned	T30
slip cast, 30	aligned	Q30
granulated tape cast, 30	oriented domains	P30
granulated slip cast, 15	random	S15
tape cast, 15	well aligned	T15
slip cast, 15	aligned	Q15
granulated tape cast, 15	oriented domains	P15
granulated slip cast, 5	random	S05
tape cast, 5	well aligned	T05
slip cast, 5	aligned	Q05
granulated tape cast, 5	oriented domains	P05
granulated slip cast, 0		S0
tape cast, 0		T0
slip cast, 0		Q0
granulated tape cast, 0		P0

Table 3.5. Method of fabrication and designated short name of the materials fabricated.

4. EXPERIMENTAL METHODS.

4.1. Introduction.

This chapter describes the procedure followed to prepare the samples for microscopy and the experimental setups used in the microstructural and mechanical characterization of the samples. Comments are made on the main advantages and disadvantages of the different techniques applied. Some results are presented in the x-ray texture characterization section. These are only meant as an illustration on the technique and are not referred to in any of the later chapters. The neutron diffraction experiments were performed at Atomic Energy Canada Limited (AECL), Chalk River Laboratories, Chalk River, Ontario.

4.2. Microscopy.

In order to prepare the samples for microscopy, material cross sections were taken perpendicular and parallel to the hot-pressing (HP) direction, the specimens were ground down using SiC paper to 1000grit, then polished down to 1μm diamond paste, and then ultrasonically cleaned in acetone and methanol. Optical microscopy was performed to visualize the different platelet textures in the samples and to verify the platelet volume fraction in the 30%[1] SiC composites. The volume fraction measurement was done using a LECO 2001 Image Analysis System, which verified the expected SiC-platelet volume fraction within 0.8%. To measure the matrix grain size, various specimens cross-sections were thermally etched[2] under a vacuum of less than 50 milliTorr at 1200°C for 6 hr. The grain size was estimated from scanning electron microscope (SEM)[3] micrographs by the Linear Intercept Method (LIM) according to the ASTM standard E112-88. The average given by LIM was multiplied by a geometrical factor (1.56) that depends on the assumed grain shape, in this case tetrakaidecahedral (truncated octahedral), to obtain the average grain size (Mendelson 1969).

---

[1] Any percentage refers to volume, unless otherwise specified.

[2] CENTORR-M60, Centorr Associates Inc. Suncook, New Hampshire, USA.

[3] SEM, Model 515, Phillips, Netherlands.

High resolution electron microscopy (HREM)[4] was performed by Dr.X.G.Ning from McMaster University as part of the characterization of the as-processed and after-creep samples. In order to prepare the samples a procedure similar to that by Alexander et al. (1990) was used. Thin sections were taken parallel to the hot-pressing direction, from these sections 3 mm diameter discs were cut and then mechanically thinned and dimpled until the thinnest section was of the order of several microns. The discs were then argon ion-milled at 4kV, 0.5μA at a glancing angle of 12°, on a nitrogen-cooled stage until perforation. Nitrogen cooling was specially useful to avoid preferential thinning of any glassy phase. The HREM main purpose was to asses the presence of impurities and any amorphous phase in the samples. In particular, the interfacial region between alumina and silicon carbide was of interest as it was expected to play a major role in the creep properties of the composites. The presence of impurities was evaluated by electron energy dispersive x-ray spectrometry (EDS) with a 1nm probe. The HREM results are described in section 5.3.

4.3. Texture measurements by x-ray diffraction.

The SiC texture of the composites was evaluated using both x-ray and neutron diffraction (section 4.5 of this chapter for the latter). In x-ray diffraction the information comes mostly from the sample surface, from a relatively limited region of varying volume. Thus, volume fraction angular distributions of the platelets cannot be directly obtained. However, differences between samples can be qualitatively evaluated. In addition, x-ray diffraction is faster and less expensive than neutron diffraction, making it ideal for preliminary comparative texture analysis.

---

[4] FEG JEOL 2010F HRTEM, JEOL, Japan.

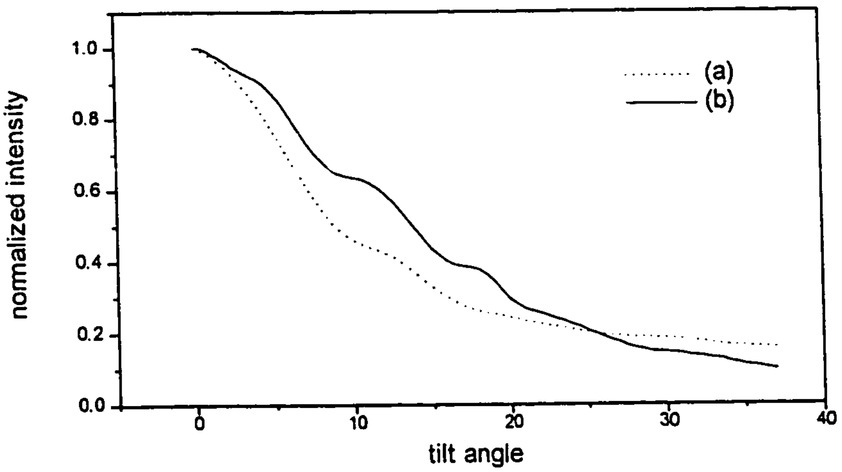

Figure 4.1. X-ray intensity vs tilt angle for two different places, (a) and (b), on the same specimen. Straight lines between data points have been added and the actual data points have been omitted for clarity.

A procedure similar to that used by Chou and Green (1992) was followed to evaluate the composite texture by x-rays. Since the samples were hot-pressed, cylindrical symmetry was assumed with the cylinder axis being parallel to the HP direction. Thus the samples were examined by rotating about an axis perpendicular to the HP direction. It was desirable to use a basal plane reflection, as this is unique for each crystal or platelet. The largest intensity basal plane peak is from the (004) plane, thus this is the best crystal plane to follow. However, the (008) plane was used instead for the measurements due to a practical constrain in the apparatus. The specimen had to be set at the relevant Bragg angle to begin with and could only be tilted to reduce this angle. A range of 36° could be achieved using the (008) plane compared to a range of 17° for the (004) plane as the respective Bragg angles (2θ) are 75.5 and 35.7°. The specimens were loaded in the chamber with the surface perpendicular to the HP direction as reference, i.e. for an aligned platelet the basal plane (008) would be lying parallel to the specimen surface. The specimens were then set to the corresponding diffraction angle θ for diffraction by the (008) plane (37.7°) and then tilted off this angle by 1° (2θ) increments about an axis perpendicular to the specimen's surface. X-ray information was recorded from each increment. A total irradiated area of about 0.5 cm^2 was utilized for each sample. This area, and the sampling volume, varied with the tilt angle. No correction was made due to this. Thus the results obtained are only comparative. A plot of platelet orientation was obtained by graphing the normalized intensity of the (008) peak (Intensity at any tilt angle η / Intensity at $\eta=0^\circ$) against the tilt angle at 0.5° intervals. The results from different runs on the same specimen but at different places can vary to a relatively large extent as illustrated on Figure 4.1. Despite this, the technique gave a good idea of the comparative textures between composites.

4.4. High temperature creep tests.

4.4.1. Creep experimental setup.

Creep experiments on ceramic materials are often performed in bending to avoid the problems of gripping, aligning and higher cost associated with tensile tests. Although experimentally easy, bending tests do not always allow exact calculations of strain and stress. Because ceramics generally creep at different rates under tension and compression, the stress distribution and the position of the neutral axis are strain (Hollenberg et al. 1971, Chuang 1986, Grathwol 1988) and time dependent (Carroll et al. 1989). Due to a higher creep resistance under compression as compared with tension, the neutral axis of the beam will tend to shift to the compressive side of the specimen. Nevertheless, flexure testing can provide meaningful creep data. Chuang (1986) developed a numerical technique by which tension and compression behaviours, equal or not, can be predicted from bend test data provided steady state is achieved and the behaviours can be described by a Norton power law (equation 2.11). In addition, flexure creep analysis can often be based (implicitly or explicitly) on the assumption that the tension/compression asymmetry is not significant (e.g. Chokshi and Porter 1986, Lipetzky et al. 1988, Lin and Becher 1991, Gu et al. 1994) i.e. assuming the neutral axis always coincides with the bar centroid. This assumption is valid if the strains are kept small and/or if tensile or compressive creep data has demonstrated that the difference in creep behaviour is not significant. In addition, a lack of steady state creep will complicate the analysis of the strain rate dependence on stress in any testing configuration. This will be furtherly discussed in later chapters.

The present creep experiments were done in bending and compression; 4x3x45mm bars were used for flexure and 4x3x8mm bars for compression. The tests were performed in a dead-weight creep furnace in which the load was applied through a lever arm and a SiC rod onto the flexure or compression rig supported on a SiC platform. The bar to be tested was first carefully aligned in the rig outside the furnace and then glued in position. Rig and sample were then placed in the furnace and aligned with the load applying push rod and three displacement-measuring probes, as illustrated in Figure 4.2 for flexure and Figure 4.3 for compression. The centre probe maintained contact with the sample or plate by a weak spring, the outer probes maintained contact by a weight compensation system which placed the probes in contact with the sample or plate. The two outer probes displacements, were mechanically averaged and subtracted from the displacement of the centre one[5]. This relative displacement y_r, between the inner and outer probe positions, was read by an LVDT[6] and the voltage signal sent to the data acquisition system[7], where the higher frequency electronic noise was filtered and the equivalent displacement was calculated according to a previous calibration. A relatively small load of approximately 100g was applied to the rig to keep it in place while heating. The glue burned at approximately 400°C, well before the testing temperature was reached, and did not react with the samples. Heating rates were non-linear, slowing down towards the desired dwell testing temperature, with an average of 250°/h. Twenty minutes after reaching the dwell temperature, the displacement measuring device was zeroed and the load was slowly applied. All tests were performed at 1250 ±2°C under air. A time vs strain graph was obtained in real time to monitor the experiment progress. The data recording rate varied according to the sample deformation rate. At the beginning of the test a data point was acquired every 3-10 sec, when the deformation rate was the fastest. At the slower deformation rates data points were acquired every 5-10 min. The typical test duration was one week.

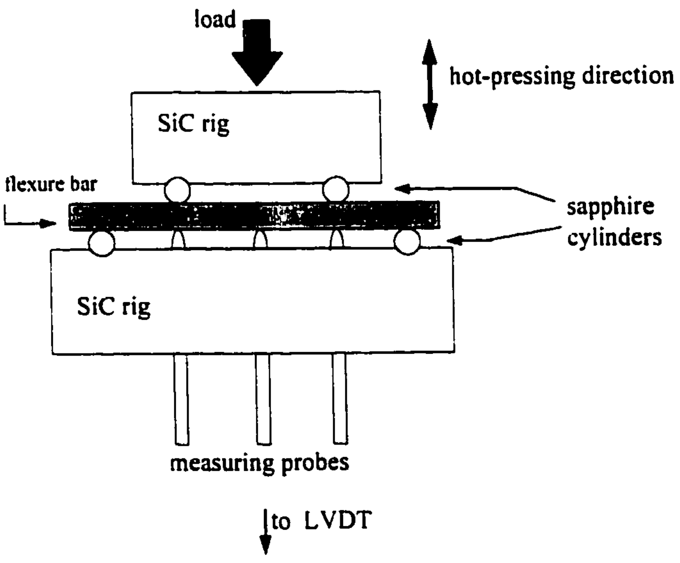

Figure 4.2. Schematic, flexure creep setting.

---

[5] System designed by Dr. G.Robertson at McMaster University.

[6] LVDT, 7DCDT-500, Hewlett Packard. Walthan, Massachusetts, USA.

[7] ATMO-16 board, 486DX PC, Labview, National Instruments. Austin, Texas, USA.

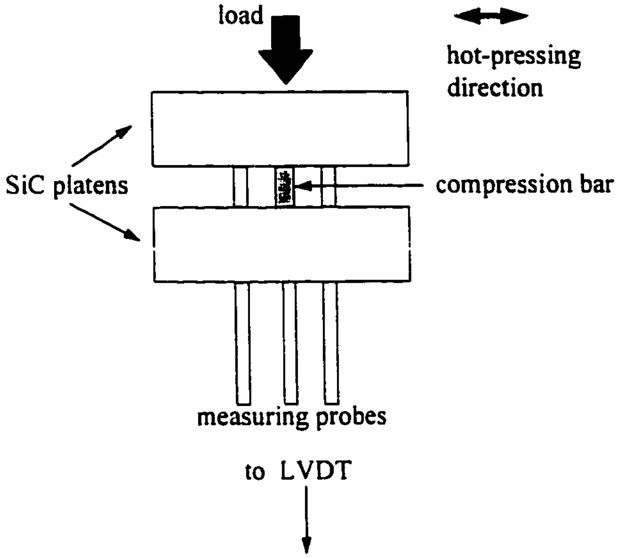

Figure 4.3. Schematic, compression creep setting.

4.4.2. Flexure tests.

The flexure tests were made in four point bending with support and load spans of 40 and 20mm, respectively. The rig was made of SiC with 3mm radius sapphire load bearing cylinders, held in place by semi-cylindrical grooves. The displacement was measured by 3 probes, one in contact with the specimen centre and the two others at 10mm from the centre exactly underneath the loading pins, this is illustrated in Figure 4.2. The centre probe was polished and rounded to minimize sample damage; as this probe is in contact with the sample face undergoing tensile strain. As compared with the point-load displacement measurement, the three-point-probe measurement is more difficult to make and the samples are more likely to be damaged (as contact with the measuring probes is required). However, the three-probe configuration is considered to be the most precise for four-point bend creep tests (e.g. Passmore et al. 1966, Hollenberg et al. 1971, and Chuang 1986). In the present experiments, the strain and stress were calculated according to Hollenberg et al. (1971). Assuming a linear moment distribution in the outer span and a constant maximum moment in the inner span, the outer fibre strain can be written in terms of the deflection y_r, measured at the centre of the beam relative to the two inner load points, for small values ($a \gg y_r$):

$$\varepsilon_{max} = \frac{4h}{a^2} y_r \qquad (4.1)$$

where, ε_{max} is the maximum strain in the outer fibre, h is the thickness of the beam, and a is the distance between load points. Assuming that the strain rate is proportional to the power n of the stress, $\dot{\varepsilon} \propto \sigma^n$ and that the neutral beam axis always coincides with the centroid, the outer fibre stress is given by:

$$\sigma_{max} = \frac{3(L-a)P}{bh^2}\frac{(2n+1)}{3n} \qquad (4.2)$$

where L is the support span, b is the width of the beam, 2P is the total load and n is the creep exponent.

4.4.3. Compression tests.

The compression setup, illustrated on Figure 4.3, essentially consisted of two 10mm thick SiC platens, between which the sample was "sandwiched". The LVDT measured the relative displacement of the platens. As in the flexure experiment, the relative displacement between the outer probes and a centre one was measured by an LVDT. The centre probe was in contact with the lower platen and the two others were placed symmetrically in opposite sides of the specimen, in contact with the upper platen. The strains were calculated as $\varepsilon = y_r/L_0$, where L_0 is the initial length of the sample and y_r is the relative displacement between outer and centre probes. The strains were kept small to try and avoid barreling. Whenever barreling was visible, the sample was discarded from the creep data analysis. However, some of the barreled samples were used for neutron diffraction analysis to measure extreme changes in texture and internal strains.

4.4.4. Dilatometer tests.

The linear dimension change during a heat-treatment of the as processed S30 and Q30 composites as compared to S0 and Q0 alumina, respectively, was measured in a dilatometer. The measurement was done on 45x4x3mm bars, parallel to their long dimension and perpendicular to the HP direction. The tests were done in flowing Ar. The samples were heated at the rate of 120°/h up to 1250°C. For the Q30 composite the dwell temperature was held for 42 hours followed by a cooldown. In the case of the S30 composite, due to an instrumental failure, the dwell temperature was held only for 28 hours.

4.5. Neutron diffraction: texture and internal strains.

The principal advantage of using neutrons rather the more conventional x-rays to evaluate texture and strain is due to their deeper penetration. Thus neutrons can be used to measure properties within the bulk of the material whereas x-rays can only be used to examine near surface regions. For most neutron-scattering studies of condensed matter, one needs neutrons with energies of about 25 meV, also called thermal neutrons (Scherm and Fak 1993). Their wavelength is comparable to the interatomic spacing in condensed matter thus enabling them to undergo diffraction. Neutrons emerging from fission or spallation reactions have their energy spectrum centred in a few MeV. These neutrons must therefore be slowed down to the desired energy range in a moderator through collisions with light atoms such as H or Be. The spectrometer arrangement used for the neutron diffraction experiments is schematically shown in Figure 4.4. Neutrons exit the reactor after having been slowed down so as to have wavelengths of the order of 1Å. The neutrons will then enter into a collimation tube consisting of a tube with Soller slits[8] and exit into a monochromator. This is usually a single crystal, where a Bragg reflection from a set of lattice planes selects a monochromatic neutron beam with wavelength λ. The monochromatic beam then traverses a second Soller slit collimator and then hits the sample to be analyzed. The diffracted neutrons are detected using a counter which rotates about the centre of the sample.

---

[8] These consist of long cadmium-lined channels which absorb neutrons which are off axis by more than a critical angle defined by the length of the channel and the width of the slits (Bacon 1975).

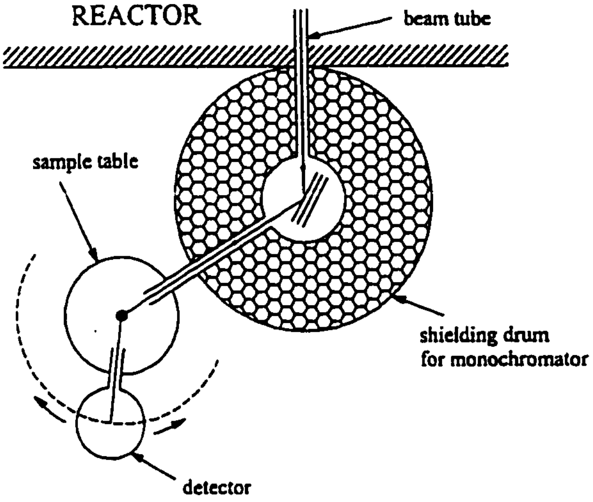

Figure 4.4. Schematic, experimental setup for neutron diffraction experiments (Gharghouri 1997)

The present experiments were done with a Ge monochromator using the (113) set of planes. This selected wavelengths of λ=2.37Å and fractions of that number, i.e. 2.37/2, 2.37/3, etc. After the monochromator, a pyrolytic graphite filter was placed which absorbed most of the λ/n wavelengths, thus obtaining a mostly monochromatic beam. The sample to be measured was mounted on a Eulerian cradle which enables the rotation of the sample by three different axis. The direction and cross-section of the incident beam was defined by a window delimited using neutron-absorbing cadmium masks near the sample. The volume of material sampled is usually defined by the intersection of the incoming and outgoing neutron beams in the sample. In our case, most of the samples used were relatively small (8x4x3mm, compression creep bars) thus the volume was defined by the sample's volume, as it was smaller than the volume defined by the intersection of the beams. Special care was taken to align the sample so that it was inside the beams intersection at all times. The direction of the outgoing diffracted beam was defined by a window near the sample and the detector position. The Eulerian cradle is shown in Figure 4.5. The detector and the Eulerian cradle were controlled by a PDP-11 microcomputer connected to a VAX microcomputer.

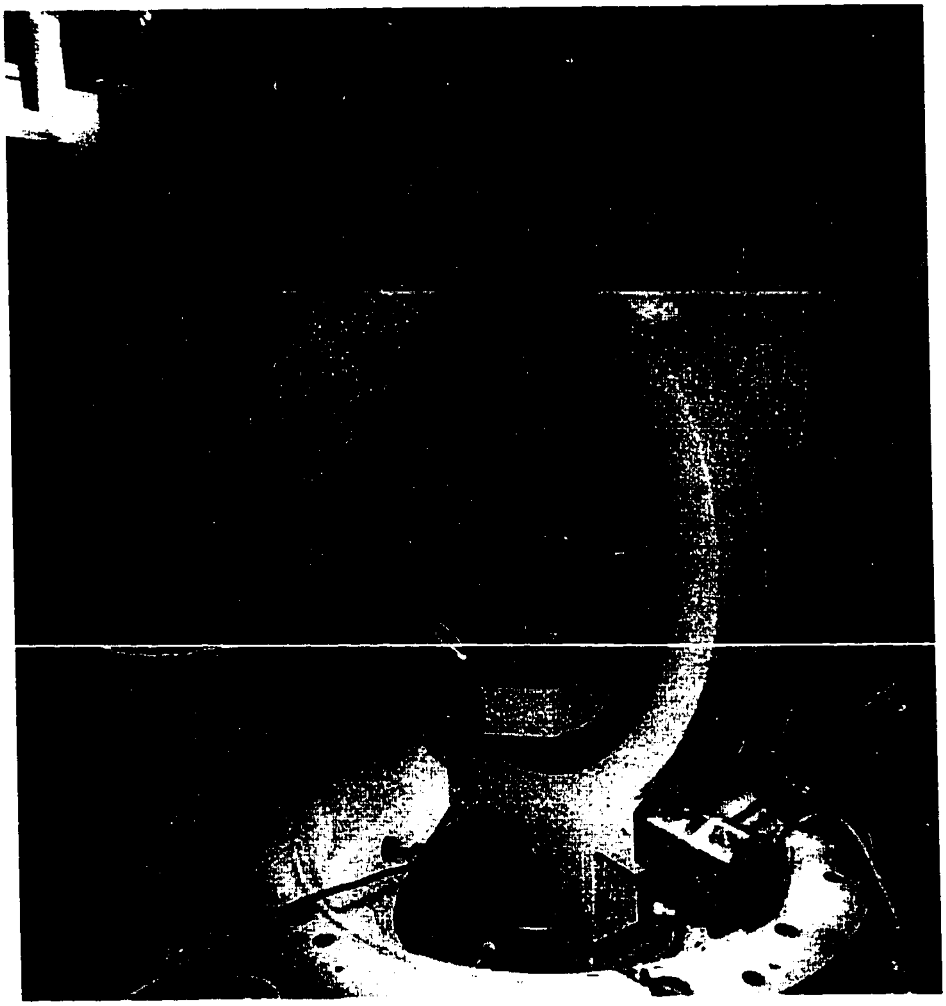

Figure 4.5 Experimental set-up for neutron diffraction measurements.

The intensity of the diffraction peak is proportional, among other parameters, to the volume of the diffracting phase. The small sample size used in this study produced relatively small diffracted intensities. As a consequence, the only samples that could be measured within a reasonable time (22-30 hr), and with relatively accurate results, were those with 30vol% SiC. A preliminary diffraction test was made in the as processed S30 sample to select the best diffraction peaks that would be measured in all samples. The highest intensity peaks produce the best results in the shortest amount of time. Choosing any overlapping peaks was to be avoided as this would mask the information obtained. The alumina and the silicon carbide are both hexagonal, thus for texture and orientation measurements it was convenient to follow a basal plane diffraction peak. As explained in section 4.3, this makes the interpretation of the results and visualization easier, since the large platelet surface corresponds to the basal plane. The following Al_2O_3 and SiC crystal planes were chosen:

Al_2O_3: (006) and (300)

SiC: (002) and $(2\,\bar{1}\,0)$

The Al_2O_3 (300) and the SiC $(2\,\bar{1}\,0)$ were selected due to the relative high intensity of their diffraction peaks together with forming a good complement to the basal plane information as they are perpendicular to that plane. However, their position in the spectrum $2\theta > 100^\circ$ (where θ is the diffraction angle) is associated with a relative large peak width and carries more uncertainty associated to their mean position than that of the basal planes where $2\theta < 70^\circ$. As in section 4.3, the samples were assumed to posses cylindrical geometry. Therefore, for each set of measurements, the samples were tilted around an axis perpendicular to the HP direction.

In order to determine the peak position μ, the integrated intensity I, and the full width half maximum from the diffraction data, standard numerical procedures used at AECL were applied. A diffraction peak can be defined by a set of 2θ-Y coordinates where 2θ is the position in degrees and Y is the number of neutrons which were detected in that position. The data is then fitted to a gaussian function superimposed on a linear background of intercept b and slope m:

$$Y = b + 2m\theta + Ae^{-\frac{1}{2}\left(\frac{2\theta-\mu}{\sigma}\right)^2} \qquad (4.3)$$

The fit is optimized by minimizing the least squares error between measured values of Y and calculated values using a Newton-Raphson iterative scheme. Initial estimates of the five parameters b, m, A, μ and σ are obtained from the raw data. In order to determine the uncertainties in the fitted parameters, the following equation is used to determine the root mean square error, χ, as follows:

$$\chi = \sqrt{\frac{\sum_{i=1}^{N}(Y_i^{calc} - Y_i^{exp})^2}{(N-5)}} \qquad (4.4)$$

where N is the number of experimental data points for the given peak. The parameter is used to determine the error in each fitted parameter. Once a peak has been fitted, the full width at half maximum (FWHM) and the integrated intensity (I) can be calculated from the following equations:

$$\mathrm{FWHM} = \sigma\sqrt{8\ln 2} \qquad (4.5)$$

$$I = A\sigma\sqrt{2\pi} \qquad (4.6)$$

In the present experiments, the error in the integrated intensity and in the FWHM varies from 3-10%, depending on the strength of the peaks.

4.5.1. Texture measurements.

The texture measurements were performed on two different size samples: 1)*large samples* (approximately 60x25x3mm) in the as-processed condition and 2)*compression bars* (8x4x3mm) in the as-processed, annealed and after creep conditions. The larger samples made it possible to measure a well-defined diffraction peak in 3-5 minutes, as opposed to 45-70 min in the smaller samples. This enabled the measurement of the large samples diffraction peaks every 5° interval, whereas the smaller samples were rotated in 15° intervals. The samples were set so that at a tilt angle of $\eta=0^\circ$, the measured planes were those perpendicular to the HP direction, as illustrated in Figure 4.6.

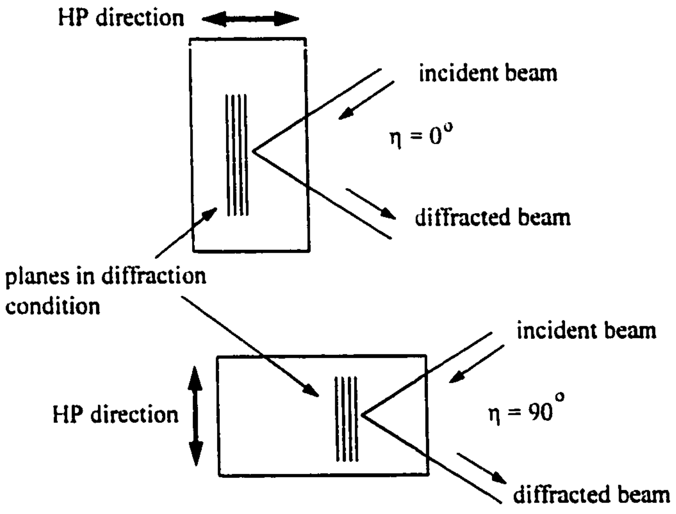

Figure 4.6. Sample geometry with respect to the tilt angle η.

The intensity, I, measured for a given tilt angle, η, is proportional to the volume of material which contributes to the signal. In our case, a correction must be made because the fraction of platelets at a given tilt which contribute to the measured intensity depends on η. This can be explained with the aid of Figure 4.7. All the basal plane normals corresponding to a given tilt can be represented by a cone with its axis coinciding with the cylindrical symmetry axis. The cone describes all possible scattering vector directions for this tilt. Two such cones labelled A' and B' are shown in the figure. The sample is modelled as a point at the centre of a sphere of radius D, which is the fixed distance between detector and sample.

The circle formed by the intersection between a cone and the sphere represents the crystals with orientation A, i.e. those crystals whose scattering vectors form cone A'. This circle is referred as the locus circle for tilt A. Since the detector is of finite size, δa, it only samples a part of this locus. The fraction of grains sampled is therefore δa divided by the circumference of the locus circle for tilt A. The same geometric constructiion for tilt B shows that the locus circle for tilt B is larger than for tilt A. However, since the detector size is fixed, δb=δa, and the fraction of grains sampled for tilt B is smaller than for tilt A. The sampled fraction of grains for a given tilt is inverseley proportional to the radius of the corresponding locus circle, which is proportional to sinη. Therefore, the volume fraction of grains at tilt angle η, V_f will be proportional to the intensity measured I and sinη. Thus in order to obtain the texture graphs from the measured integrated intensity I, the volume fraction of platelets located in a specified angular range was first calculated as:

$$V_f = \frac{I\sin\eta}{\sum I\sin\eta} \qquad (4.7)$$

Equation 4.7 is customarily used for this type of data analysis, similar procedures can be found in Gharghouri (1997) and Sandlin et al. (1997). Unfortunately, this procedure artificially diminishes the volume fraction values at low angles. By multiplying by "sinη" the V_f values are underestimated at low angles and, consequently, over estimated at high angles. However, most frequently, the interest lies on how a sample compares with a random sample, and not in the actual V_f values. Then the volume fraction values are usually then normalized with respect to those ones of a randomly oriented sample. Thus the incertitude of the procedure will not affect the final results.

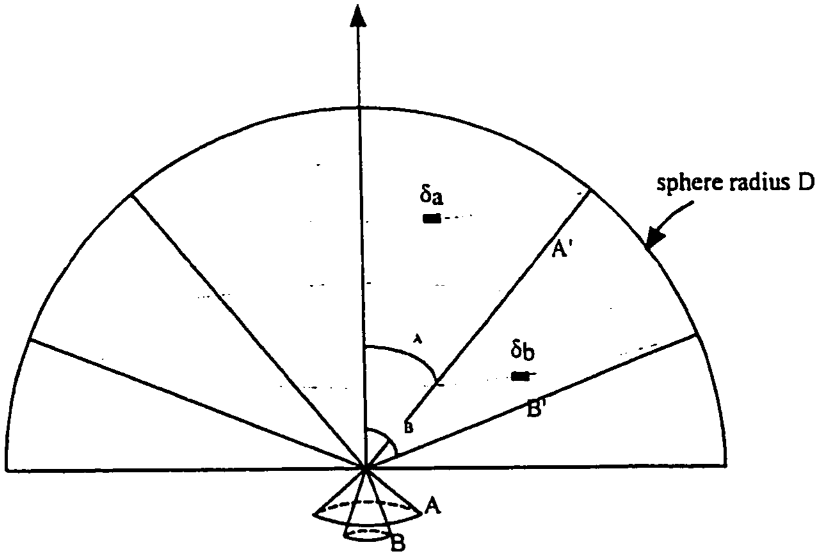

Figure 4.7. Figure showing the tilt dependence of the measured intensity (Gharghouri 1997).

It is worthwhile mentioning that the particle alignment can also be evaluated based on angular distributions of planar sections (Park et al. 1994, Sandlin et al. 1997). The method has some disadvantages, in that it is destructive and it requires a great deal of manual measurements making it time consuming and prone to bias. However, the method is a very good alternative in systems where diffraction is difficult or impractical.

4.5.2. Internal strains.

The strain was determined using Bragg's law of diffraction,

$$2d^{hkl}\sin\theta^{hkl}=\lambda \qquad (4.8)$$

where d^{hkl} is the crystal lattice spacing corresponding to a Bragg reflection observed at the scattering angle $\phi^{hkl}=2\theta^{hkl}$, λ is the neutron wavelength, and (hkl) are the Miller indices of the diffracting planes. For a monochromatic source (λ= constant) the strain ε is then obtained with equation 4.8 and

$$\varepsilon=\frac{d-d_o}{d_o}=\frac{\Delta d}{d_o} \qquad (4.9)$$

where d_o is the lattice spacing of the unstrained material. The shift in the Bragg angle relative to that of the stress-free material is used to calculate the average lattice strain present in the volume sampled. Thus the lattice spacing d_0 of the unstrained material must be known. This was obtained by measuring the lattice spacing in a mixture of alumina and SiC heat treated powders. The strains which needed to be measured were those associated with the thermal expansion coefficients of the phases and netwoking of the second phase. Thus the powders were subjected to a heat treatment similar to the sintering of the composites so as to mimic any structural changes that could arise as a result of exposure to high temperatures.

The error in the lattice strain was calculated by differentiating equation 4.9 and obtaining an equation in terms of $\Delta\theta$ and $\Delta\theta_0$, which were determined with equation 4.4. The calculated error in the measured strain was approximately $\pm 1.3\times10^{-4}$. However, on repeating the same measurement, the calculated strain values could vary up to $\pm 2\times10^{-4}$. Thus the latter value, 2×10^{-4}, was taken as the error in all strain values.

4.6. Summary.

The experimental methods for the characterization of the samples have been described. Some of the main advantages and drawbacks of the methods were mentioned. Most of the results presented in the next chapter are based on calculations from experimentally measured variables. In those cases, the calculations based on the raw data have been described. Further manipulation of the data is explained in the Results and Discussion chapters.

5. RESULTS

5.1. Introduction.

This chapter is divided according to the experimental technique employed to obtain the results presented. The only exception involves the density and average grain size results, as it is convenient to present them together in table form. Only limited observations are made in this chapter. The results presented here are commented on mainly in the Discussion chapter. In some of the graphs, the experimental points are linked by straight lines within a set of data. These are meant to guide the eye and are not intended to imply that all the data follows linear relationships.

5.2. Density and grain size.

Table 5.1 summarizes the density and average grain size results of all the materials fabricated, in their as-processed state. In addition, the grain size of the S30 and T30 composites was measured after creep (compression, 7 days at 1250°C, 21.5 MPa, $\varepsilon \approx 2\%$). No change in the average grain size was detected. Therefore, no more after creep grain size measurements were made.

The lowest as-processed density was that of the P30 composite. It is likely that the anisotropic shape of the P30 agglomerates did not facilitate homogeneous compaction while cold pressing. As a consequence, the P30 green body likely had a relatively inhomogeneous density and sintering was uneven leading to a lower final density. Density measurements on crept S30 compression specimens did not show any change as compared with the as-processed values, within the experimental error of the density measurement (±1%). However, the slip cast composites developed the least amount of porosity and amorphous phase during creep. Thus they are the least likely to show any change in density.

composite, SiC vol%	designation	density (%ρ_{th} ±1%)	grain size (μm ±0.2μm)
granulated slip cast, 30	S30	99	2.6
tape cast, 30	T30	99	2.7
slip cast, 30	Q30	98	2.5
granulated tape cast, 30	P30	97	2.7
granulated slip cast, 15	S15	99	2.7
tape cast, 15	T15	98	3.2
slip cast, 15	Q15	99	2.6
granulated tape cast, 15	P15	98	not measured
granulated slip cast, 5	S05	99	2.5
tape cast, 5	T05	99	3.3
slip cast, 5	Q05	99	2.6
granulated tape cast, 5	P05	98	not measured
granulated slip cast, 0	S0	99	2.8
tape cast, 0	T0	100	2.8
slip cast, 0	Q0	99	2.7
granulated tape cast, 0	P0	99	not measured

Table 5.1. Densities and average grain size of the as-processed Al_2O_3/SiC composites.

5.3. Optical microscopy and SEM.

5.3.1. As-processed.

The different platelet orientation distributions in the composites can be visualized in Figure 5.1 which shows optical micrographs of as-processed S30, T30, Q30 and P30 samples. The HP direction in the photographs is vertical, the light phase is SiC and the dark phase is the Al_2O_3 matrix. The S30 composite shows the least texturing. The T30 composite shows the most anisotropic orientation distribution. The texture of Q30 lies somewhere in between those of S30 and T30. Finally, the P30 composite is formed by an assembly of cells or domains. Each domain originated from one agglomerate, and retains the orientation anisotropy of the green tapes. Thus within each domain the platelets are preferentially oriented in the original tape cast direction.

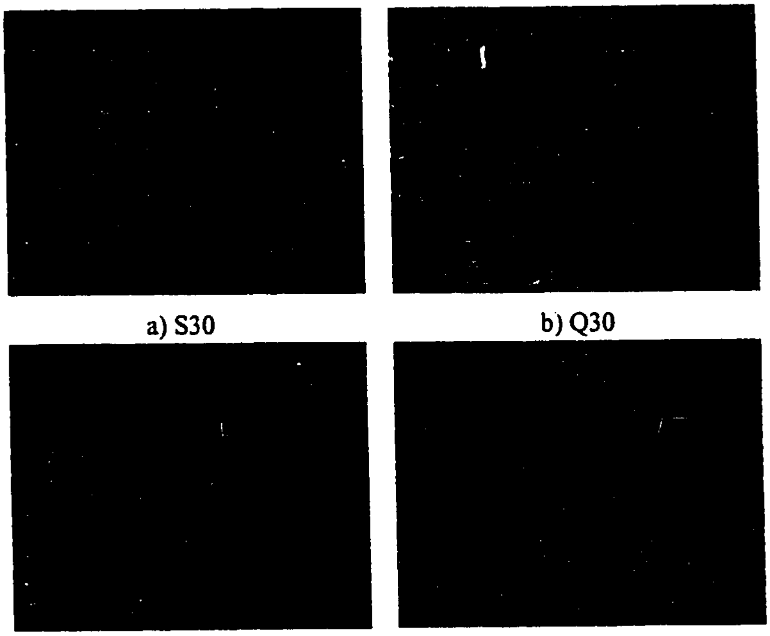

a) S30

b) Q30

c) P30

d) T30

Figure 5.1. Optical micrographs of as processed composites. Slip cast: a) S30, b)Q30 and tape cast: c)P30, d)T30. The HP direction is vertical.

The average grain size was determined from SEM micrographs of polished and thermally etched sections such as the ones shown on Figure 5.2 for the slip cast S materials. As the volume fraction of SiC decreases, the number of larger grains seems to increase. Even though the average grain size is similar in all materials, the grain size distribution must vary with the SiC volume fraction to allow for the increased number of large grains. These micrographs (Figure 5.2) were complemented with higher magnification observations (or micrographs, when necessary) of the same area. These helped to readily recognize all grain boundaries and any SiC particle that could be confused with an alumina grain. Figure 5.3 shows a higher magnification micrograph showing a grain boundary and a SiC particle that would be concealed at lower magnifications.

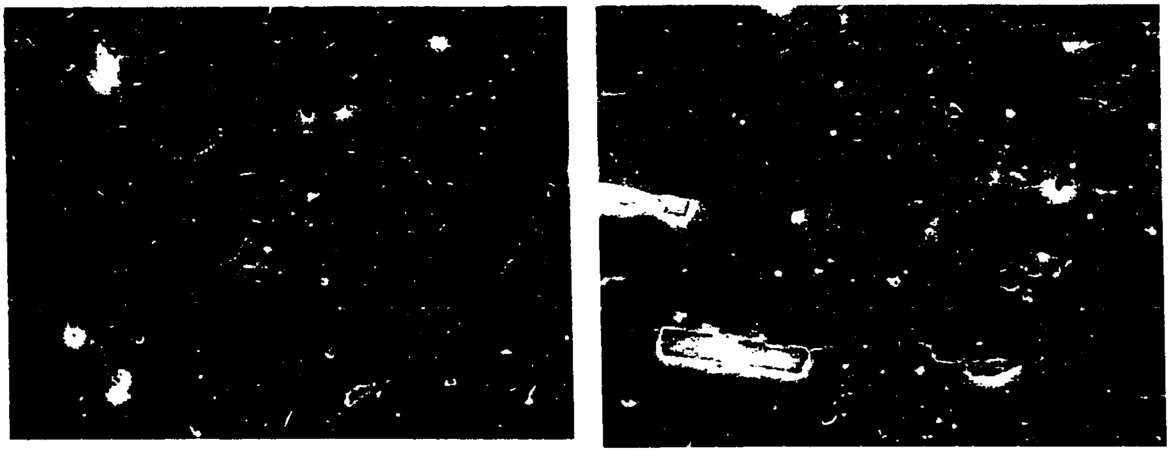

a) 0% SiC b) 5% SiC

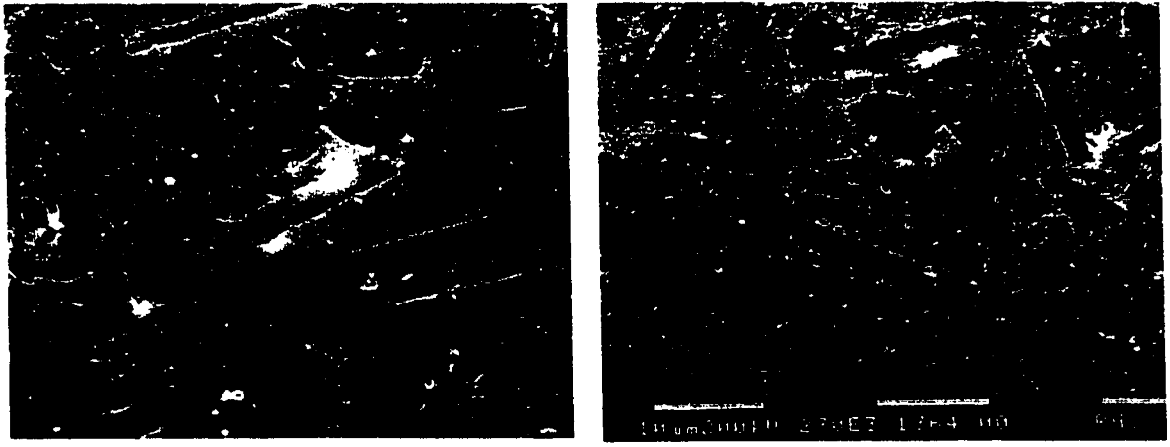

c) 15% SiC d) 30% SiC

Figure 5.2. SEM micrographs for grain size evaluation. Slip cast materials: a) 0%, b) 5%, c)15% and d) 30% SiC.

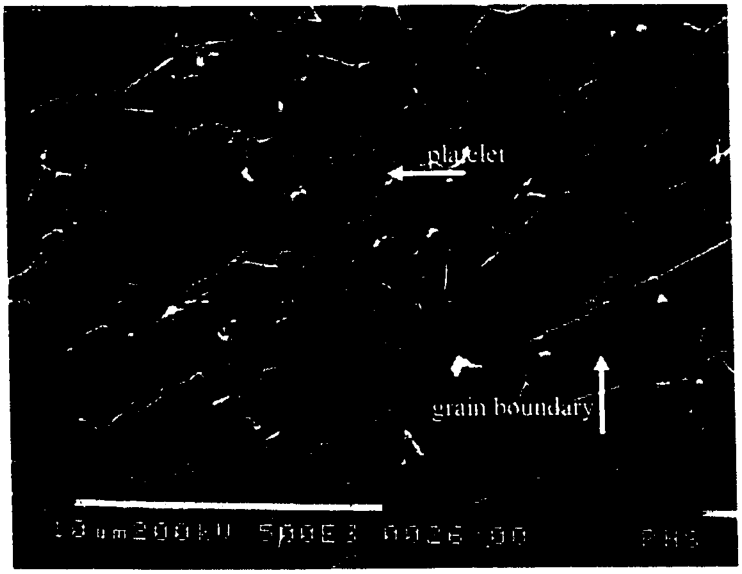

Figure 5.3. These SiC platelet and grain boundary are not readily recognizable at lower magnifications.

5.3.2. Crept material.

The micrographs shown on Figure 5.4 were taken from a crept S30 flexure bar with a 2.5% maximum strain on the tensile side; the stress direction being horizontal in the pictures. The tensile side of the bar (Figure 5.4. a)) shows a fairly homogeneously distributed cavitation. Note that the cavities are not always associated with a SiC platelet. The cavities are larger than originally due to the polishing used, that tends to enlarge any surface dimple-like feature, to prepare the sample. On the other hand, no voids are evident on the compressive side of the bar (Figure 5.4.b)).

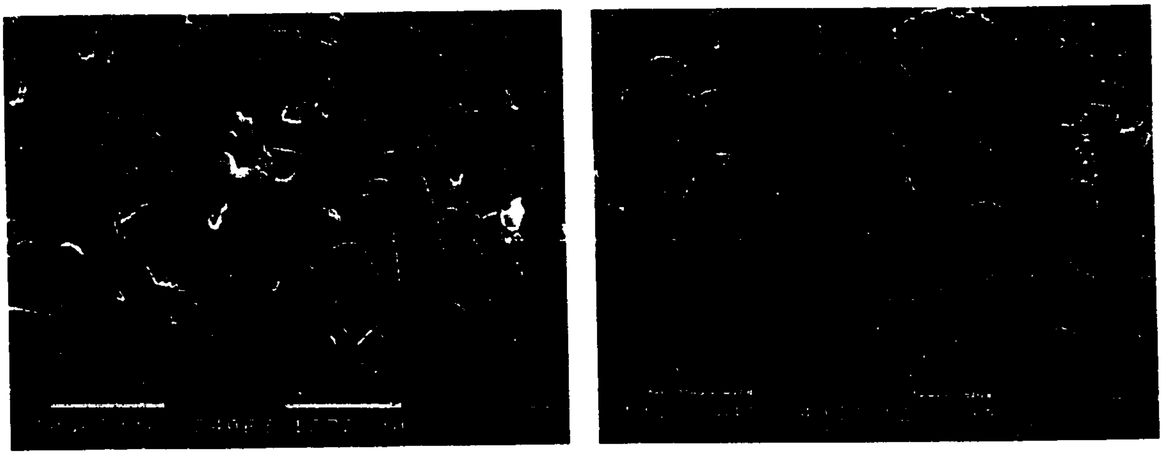

a) b)

Figure 5.4. After creep flexure bar; a)tensile side. b)compressive side.

The after creep surfaces of the T30 and S30 composites are qualitatively different, as shown on Figure 5.5. A glass-like phase, probably due to extensive oxidation, can be observed on the T30 composite surface, particles appear embedded in this phase. The somewhat blurry dark circular spots are cavities underneath the surface which seem to be bubbles. Figure 5.6 shows what appears to be a large bubble breaking the surface of the T30 composite. In the case of the S30 composite the glass does not cover all the surface uniformly (Figure 5.5. a). Rather, it is distributed in an irregular patchy way. Bubble-like cavities could also be found in the S30 composite, however to a much less extent than in the T30 one. Typical x-ray spectra of the glass-like phase on the surface are shown beside the micrographs. The x-ray analysis revealed the presence of K, Na, Ca and Mg in the T30 glassy phase. The S30 x-ray analysis shows the presence of Ca, K and Mg. The Ca is present in larger quantities in the S material, while K is more prevalent in the T composite. The samples were gold coated which explains the presence of Au in both spectra.

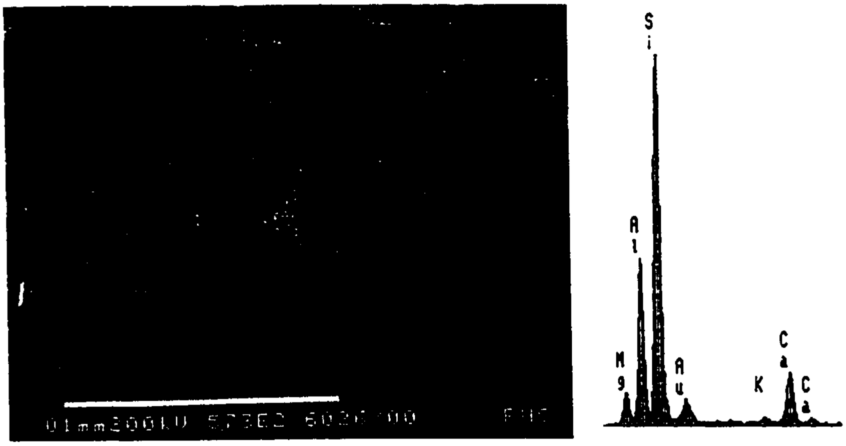

a) S30

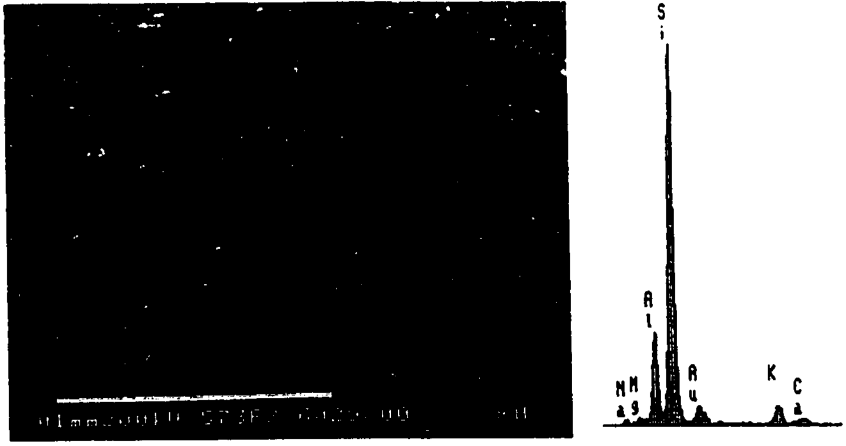

b) T30

Figure 5.5. After creep surfaces (7 days at 1250°C) and x-ray analysis of glass phase; a)S30, b)T30.

Figure 5.6. Micrograph of cavity on T30 surface.

5.4. HREM.

5.4.1. As-processed.

High resolution micrographs of representative Al_2O_3/SiC interfaces in the as processed S30, Q30 and T30 composites are shown in Figure 5.7. No HREM was done on the P30 composite, as the preparation of the samples is very time consuming and it was felt that the results would be very similar to those of the T30 samples; as a practically identical creep behaviour of the T30 and P30 composites was found. In the S30 and Q30 composites no distinct amorphous phase was found at the interface. In general, this region exhibited only a relatively small disorder and no clear amorphous region could be seen. On the other hand, the T30 interfaces presented a distinct disordered region. The observed amorphous layer, mainly an aluminosilicate phase, was distributed continuously along the interface. It is important to note that all micrographs are of edge-on interfaces with respect to the beam direction so that the width of the interface is parallel to the paper.

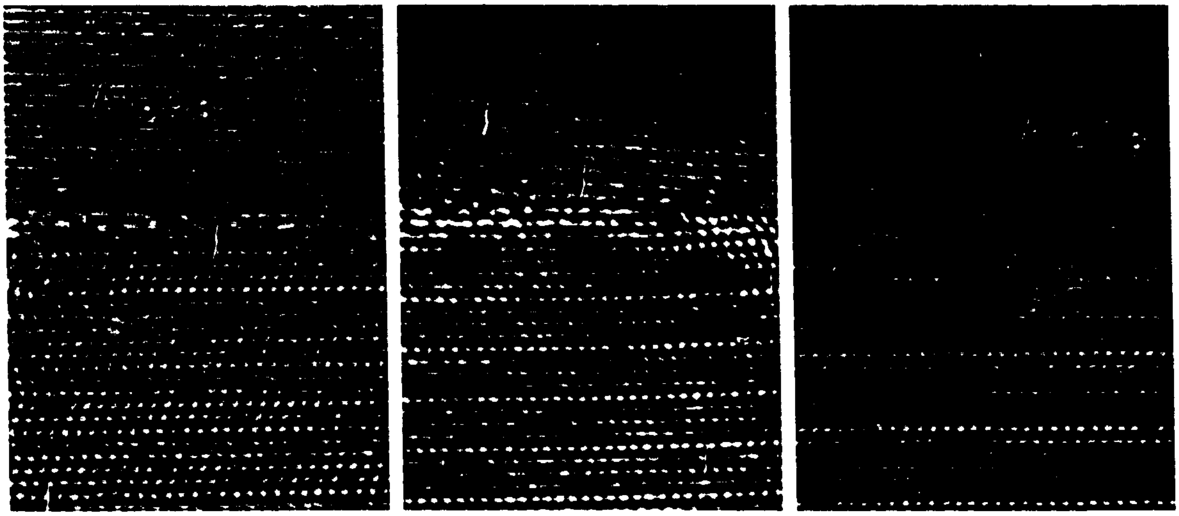

a) S30 b) Q30 c) T30

Figure 5.7. Al_2O_3/SiC interfaces in as-processed a) S30, b) Q30 and c) T30 composites. The distance between bright spots in the SiC is 2.5 Å.

Figure 5.8 shows an Al_2O_3/SiC interface in the S15 as-processed composite. A discontinuous amorphous layer and graphitic carbon were found along the interfaces. This type of interface is probably responsible for the poor creep properties found in this material. The presence of graphite can suggest the precipitation of C during processing (Chowdhury et al. 1995, Pan and Baptista 1996). However, the presence of relatively large quantities of C, strongly suggests contamination of the samples during processing rather than C precipitation.

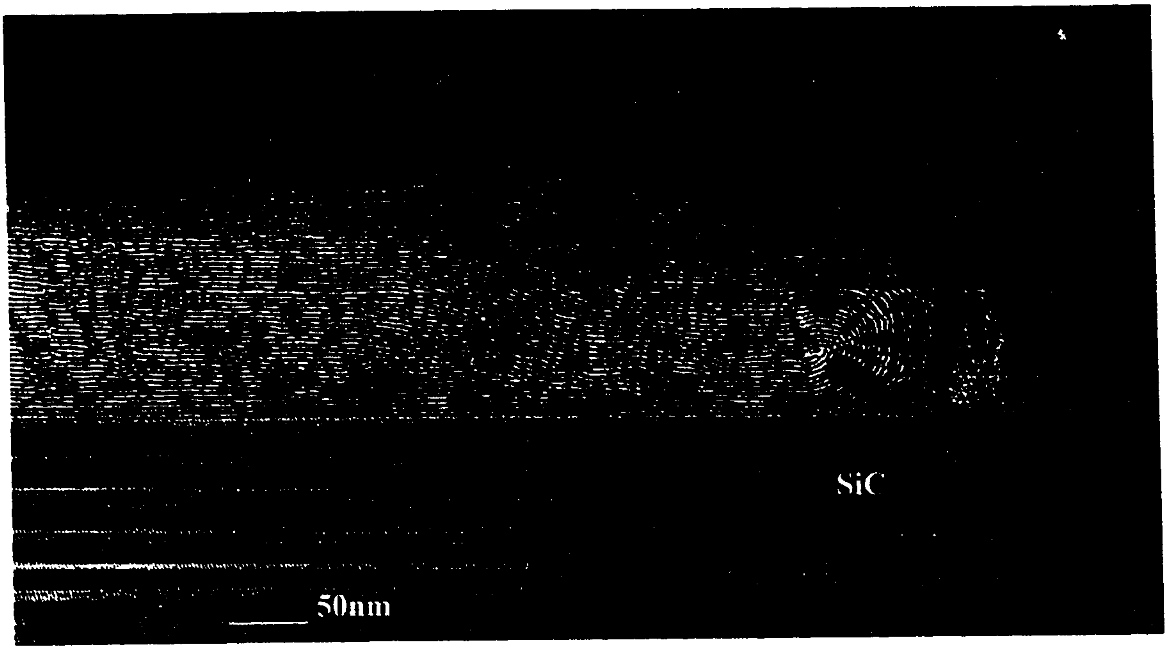

Figure 5.8. Al_2O_3/SiC interface in as-processed S15 composite. The fingerprint-like structure extending to the left at the interface is graphite. An amorphous layer can be seen extending to the right.

5.4.2. Crept material.

After creep micrographs were taken from compression samples; their strain vs. time curves are shown on Figure 5.9. The final time and strain basically coincides for all samples, thus the results are readily comparable with each other in terms of the amount of cavitation present and the oxidation that occurred during exposure to air at high temperatures. Figure 5.10 shows transmission electron microscopy (TEM) micrographs of the S30 and T30 composites. Voids can be seen associated with the labeled platelets. It is clear that cavitation occurred to a larger extent in the T30 composite as compared with the S30 one.

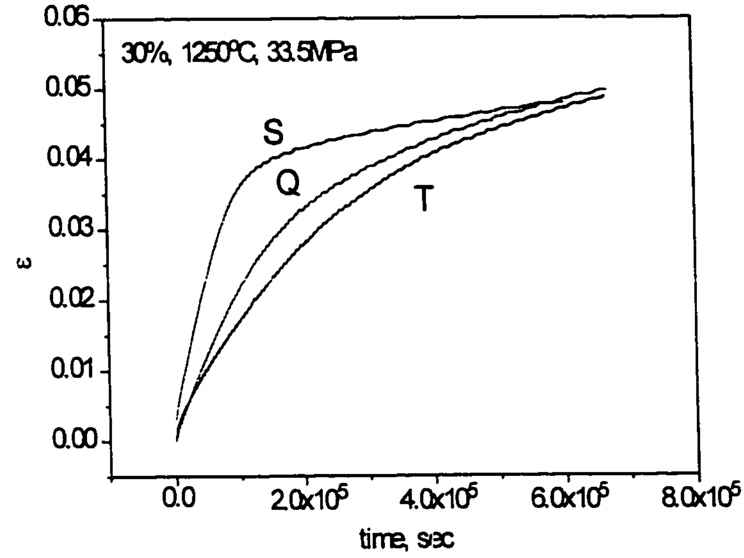

Figure 5.9. Creep curves for samples employed in after creep TEM and HREM observations.

a) S30

b) T30

Figure 5.10. TEM micrographs of after creep , $\varepsilon=5\%$, a) S30 and b) T30 composites. The large light areas are the SiC platelets, the dark area is the alumina matrix. Some cavities and areas of cavitation are indicated by the arrows.

High resolution electron microscopy of the crept composites revealed an amorphous aluminosilicate layer on all the Al_2O_3/SiC interfaces. HREM micrographs are shown in Figure 5.11. In the S30 and Q30 samples the interfacial layer appears to be distributed homogeneously around the platelets with a thickness of less than 1 nm. This interfacial phase likely results from the oxidation of SiC when exposed to air at elevated temperatures. In the case of the T30 composites, the observed creep effect on the amorphous layer was to enlarge it. In addition, graphitic carbon was observed along the platelet/matrix interface. However, the graphite was not observed extensively and it is not possible to conclude that it formed during creep rather than during processing.

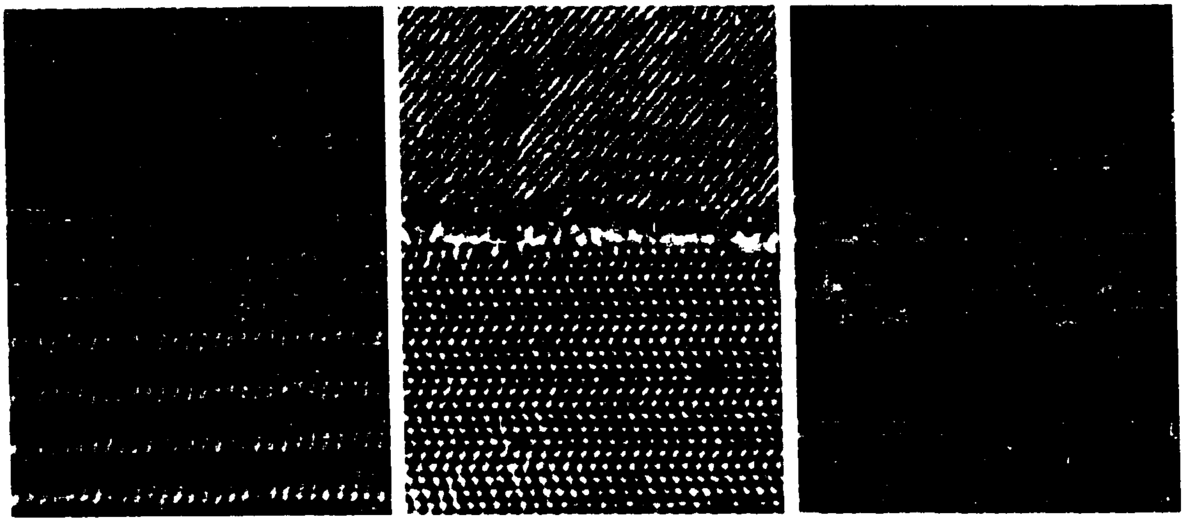

a) S30 b) Q30 c) T30

Figure 5.11. Al_2O_3/SiC interfaces in after creep a) S30, b) Q30 and c) T30 composites. At the T30 interface a series of lines can be seen near the alumina grain, their spacing corresponds to that of graphitic carbon. The distance between bright spots in the SiC is equivalent to 2.5 Å.

The difference between slip cast and tape cast composites is also manifested in the voids formed at triple junctions during creep, between two matrix grains and a platelet. Figure 5.12 shows micrographs of typical voids. The cavity size in the slip cast materials (S30 and Q30) is very similar while the cavities tend to be larger in the tape cast composite. Nevertheless, at alumina triple junctions there are no clear differences in void size between composites. This is illustrated in the micrographs of Figure 5.13.

It is also interesting to note that the cavities in the T30 composite seem to have rounder boundaries rather than the more straight edges found in the slip cast composites.

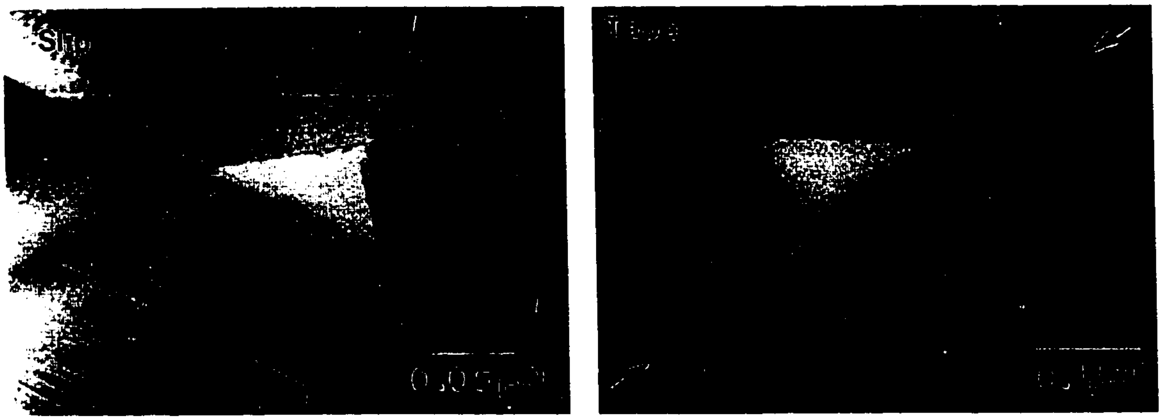

a) S30 b) T30

Figure 5.12. Cavitation at an Al_2O_3 grain boundary and Al_2O_3/SiC interface; a) S30 and b) T30, the arrows indicate the Al_2O_3/SiC interface. Please note the change in scale.

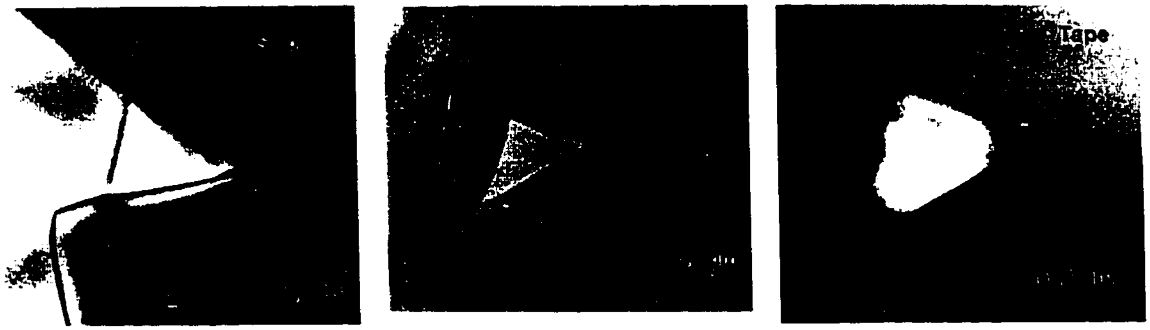

a) S30 b) Q30 c) T30

Figure 5.13. Cavitation at alumina triple junctions; a) S30, b) Q30 and c) T30.

Figure 5.14 shows a cavity in the T30 composite that probably developed from an accumulation of glass phase. The presence of ligaments extending across the void have been interpreted in SiC-whisker reinforced alumina as an indication that the aluminosilicate phase behaved as a viscous liquid during creep deformation (Lipetzky et al. 1991).

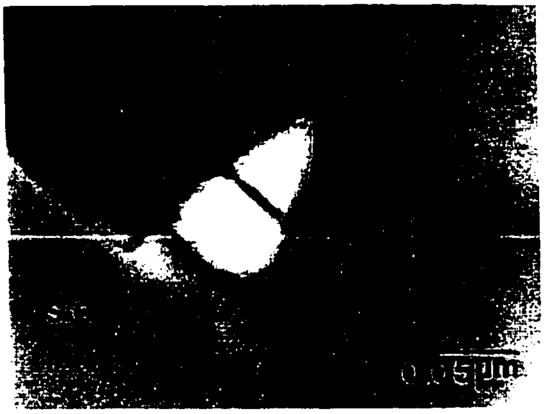

Figure 5.14. Cavitation in the T30 composite.

The composition of the alumina grains, alumina grain boundaries, SiC platelets, as well as the Al_2O_3/SiC interfacial region was examined by EDS. Table 5.2 lists the elements found in grain boundaries and interfaces. The alumina and SiC platelets presented a fairly clean composition and were basically the same before and after creep. Impurities were concentrated near or at grain boundaries and interfaces. The level of impurities at grain boundaries and interfaces varied with location to a relatively large extent. No larger variations were detected between as-processed and after creep samples. Both S30 and Q30 slip cast composites had similar levels of impurities both in the as-processed and after creep conditions. The T30 material presented a higher quantity of impurities than the slip cast composites.

	alumina grain boundaries	Al_2O_3/SiC interfaces
slip cast	Al, O, Zr	Al, Si, O, C, Zr, S, Ca, Fe
tape cast	Al, O, Na, S	Al, Si, O, Na, C, S, Ca, Cl, K, Fe

Table 5.2. Elements found at grain boundaries and interfacial amorphous layer in after creep samples.

Similar to the results of Lipetzky et al. (1991) on crept Al_2O_3/SiC whisker composites, the compositions of the glass phases were different from the, mainly silica, composition expected from SiC oxidation alone. A significant amount of aluminium was found. Typical glassy interfacial phase EDS data are shown in Figure 5.15. The spectra show predominantly silicon and aluminium. Since no crystallites of alumina or mullite were observed by HREM, it is likely that the alumina was dissolved in the apparently homogeneous glassy phase. Impurities such as S or Ca can greatly increase the solubility of alumina in aluminosilicate glass (MacDowell and Beall 1969). Thus the presence of impurity elements in the amorphous layer likely inhibited phase separation, resulting in the observed homogeneous alumina-rich interfacial phase.

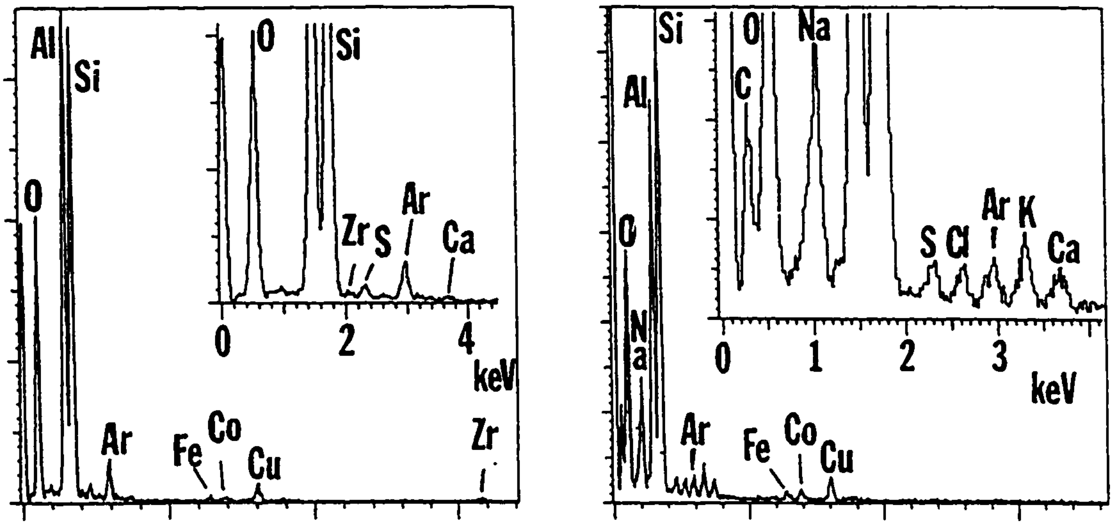

a) S30

b) T30

Figure 5.15. Typical EDS results for Al_2O_3/SiC interfacial phase in the after creep composites; a) S30, b) T30. The Co, Cu and Ar impurities were found in all spectra and are presumably due to the TEM sample preparation process.

5.5. Texture, x-rays.

The comparative plot of platelet orientation obtained by graphing the normalized intensity of the (008) peak against the tilt angle at 0.5° intervals is shown on Figure 5.16 for the S30, P30, T30 and Q30 as-processed composites. A tilt angle $\eta=0°$ corresponds to platelets whose basal plane is perpendicular to the HP direction.

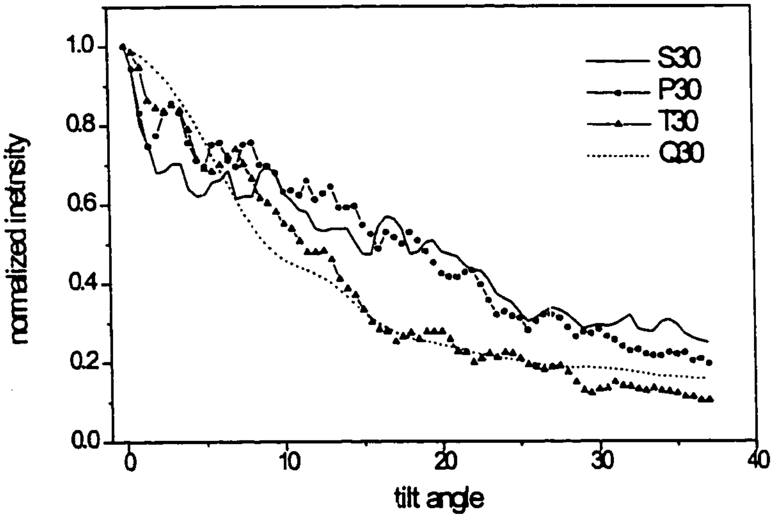

Figure 5.16. Comparative plot of platelet orientation in the S, P, T and Q30 composites. The lines between data points have been added as an aid to guide the eye within one data set. In the case of the slip cast materials, S and Q, the actual data points were removed for clarity.

5.6. Creep.

5.6.1. Shape of the creep curves.

The S0, T0 and Q0 materials creep curves presented, as is common for alumina, a short transient creep followed by a constant strain rate. Their shape being typically that of Figure 5.17. For the S, T and Q composites strain vs. time flexure creep curves are shown in Figures 5.18, 19 and 20, respectively. The following particulars are noted:

-Most curves show a decreasing strain rate with time, indicating that a steady-state was not reached.

-The S30 curve can be roughly divided into a rapid strain rate and a slow strain rate linear sections separated by a relatively short transition.

-The curve corresponding to Q30 lies in between those of S30 and T30. This can be better seen in Figures 5.9 and 5.21.

-The shape of the creep curves is the same in flexure and in compression.

-The behaviour of the T30 and P30 composites is practically identical.

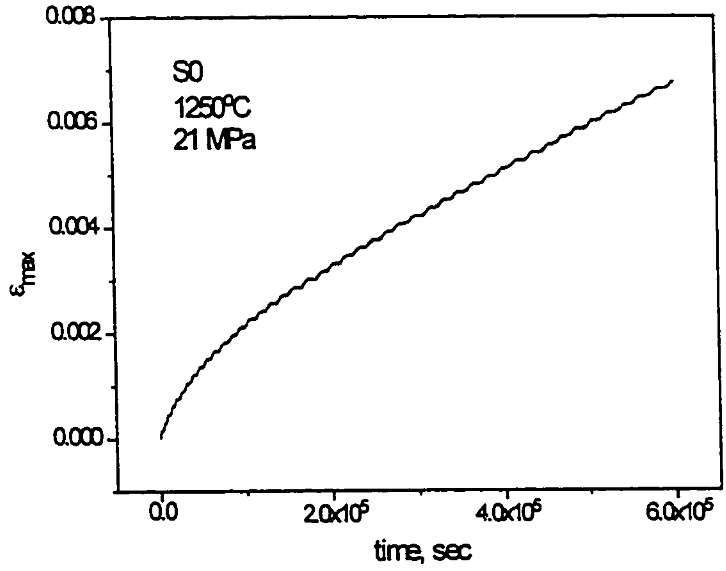

Figure 5.17. Typical alumina flexure creep curve.

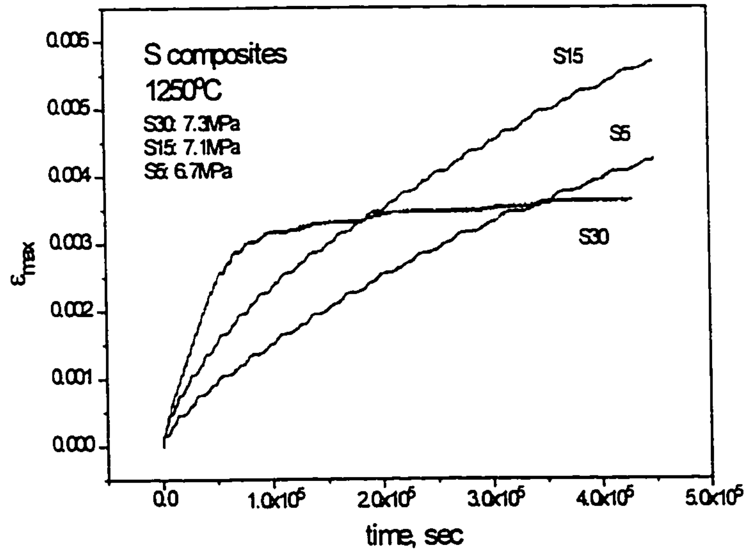

Figure 5.18. Flexure creep curves for granulated slip cast composites. The corresponding strain rates are: 30%-$1.2\times10^{-9}s^{-1}$, 15%-$6.76\times10^{-9}s^{-1}$, 5%-6.27×10^{-9} s^{-1}.

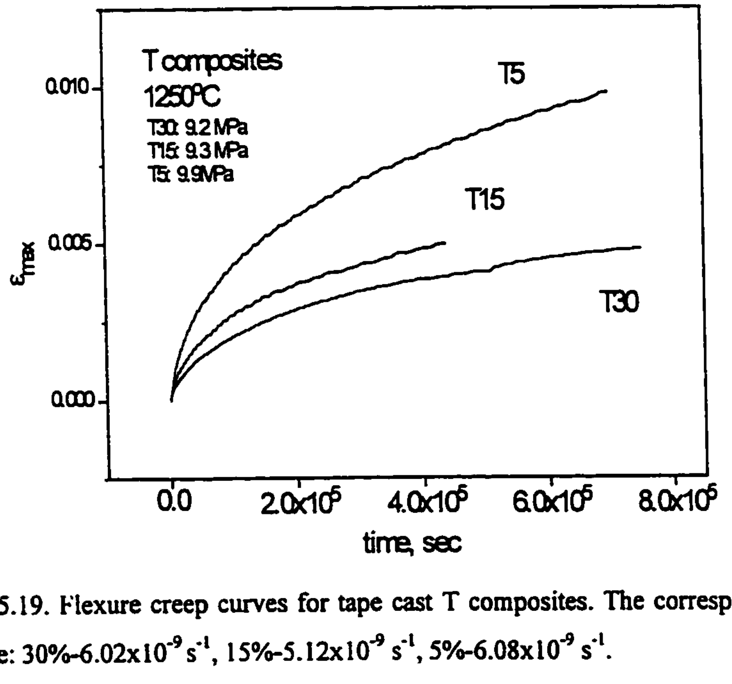

Figure 5.19. Flexure creep curves for tape cast T composites. The corresponding strain rates are: 30%-6.02×10^{-9} s^{-1}, 15%-5.12×10^{-9} s^{-1}, 5%-6.08×10^{-9} s^{-1}.

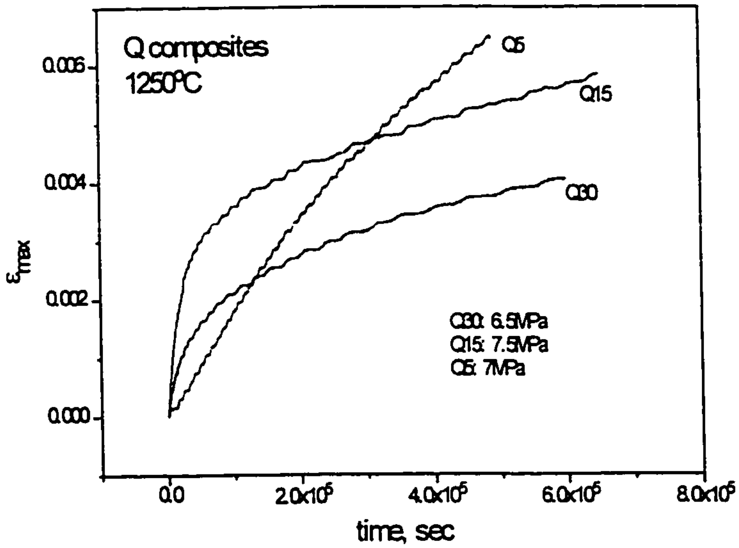

Figure 5.20. Flexure creep curves for slip cast Q composites. The corresponding strain rates are: 30%-2.7x10^{-9} s^{-1}, 15%-2.6x10^{-9} s^{-1}, 5%-9.2x10^{-9} s^{-1}.

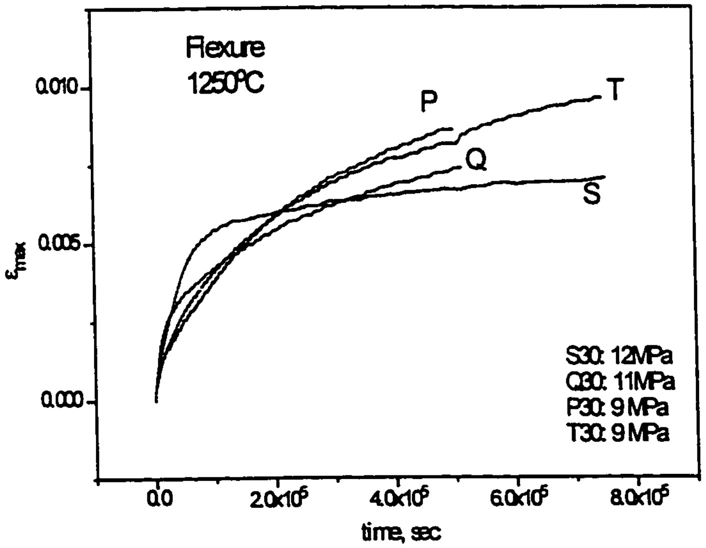

Figure 5.21. Flexure creep curves for the 30% SiC composites. T30 and P30 show practically the same behaviour.

5.6.2. Effect of annealing.

In the absence of failure, the S30 composites creep curves can be divided in three sections: a rapid strain rate regime, a transition period and a slow strain rate regime, as shown in Figure 5.22a-b. As a reference, Figure 5.22c compares the strain rate of the S30 composite with that of alumina. The strain rate vs.time curves are obtained by numerically differentiating strain vs.time curves[1]. From the S30 strain rate vs. time curves of Figure 5.22b, an almost constant strain rate is reached in the interval between test commencement and 3-4x10^4sec. This is followed by a transition period, the passage from the first, rapid strain rate, regime into the second, slow strain rate. After 1.5x10^5sec the strain rate has decreased one or two orders of magnitude with respect to the one of the first regime and is nearly constant. In order to resolve the time-dependency of this behaviour, a compression sample was subjected to an anneal-like heat treatment for 1.5x10^5sec and then subjected to creep. These results are compared with those from an unannealed specimen in Figure 5.23. From this test it became evident that the onset of the second slow-creep regime is time dependent.

---

[1] The procedure is very sensitive to small changes in the initial curves and therefore susceptible to fluctuations in the experimental strain values that might be only a result of vibrations an/or electronic noise. Thus the strain rate curves present features that are not necessarily meaningful and the observations will be limited to the general shape of the curves.

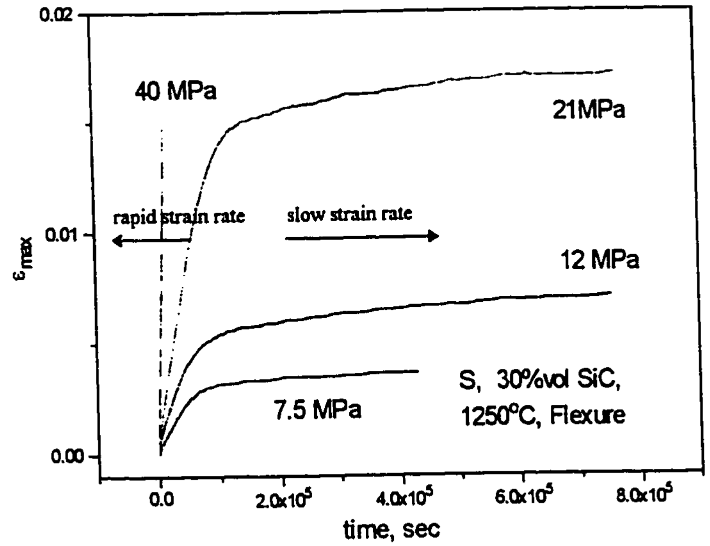

Figure 5.22a. Flexure creep curves for the S30 composite. Note: the sample subjected to 40 MPa failed.

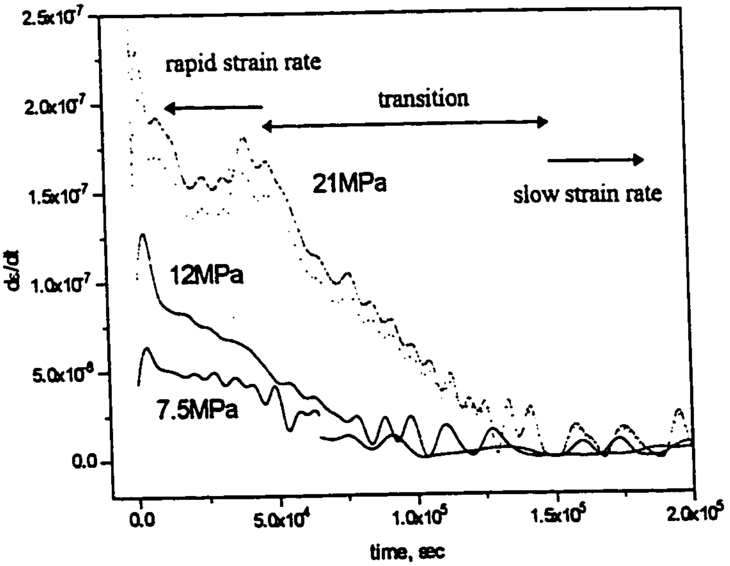

Figure 5.22b. Time vs.strain rate curves for the above S30 samples. Note: there is a change in scale on the time axis.

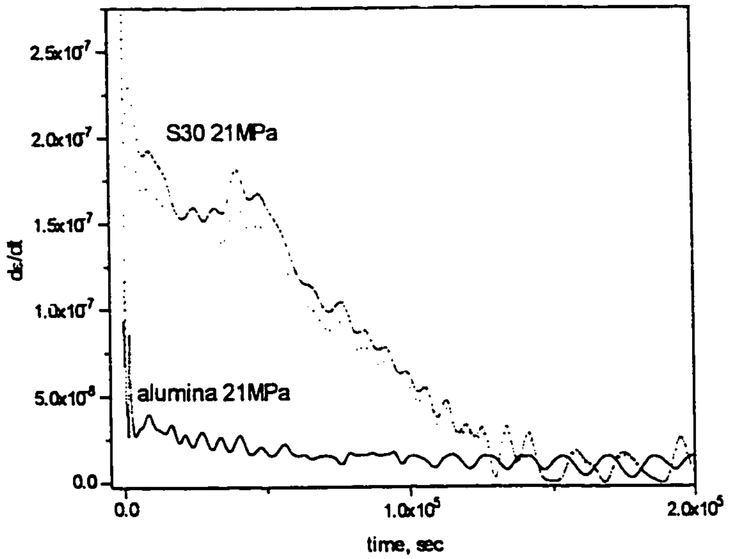

Figure 5.22c. Comparison between S0 (alumina) and S30 materials.

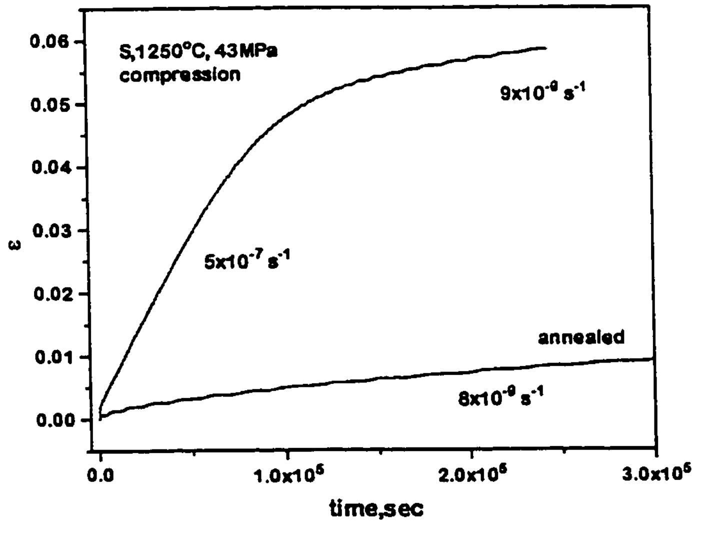

Figure 5.23. The effect of heat treating on the S30 composites is to reduce the strain rate to the slow creep values. The sample was annealed for $1.5x10^5$sec.

5.6.3. Anelastic experiment.

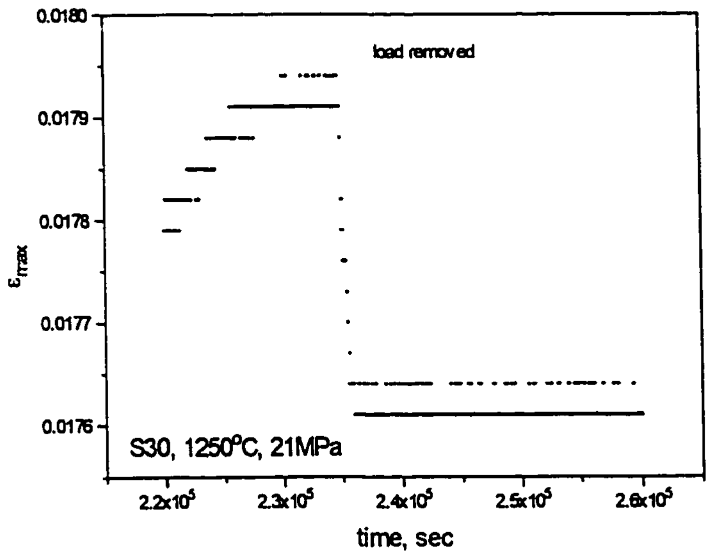

Figure 5.24. Anelastic experiment on S30 composite in flexure.

The elastic loading of a composite reinforcement network undergoing creep is likely to be associated with a relatively large strain recovery upon load removal (Porter 1988). When the load was removed during a creep experiment (Figure 5.24), the S30 composite recovered 1.7% of the total strain equal to a strain of 0.03%. No measurable anelastic recovery was found. This is in contrast with SiC-whisker reinforced alumina which has been reported to recover 20% of the total strain (Porter 1988) in a similar experiment. The S30 results can also be compared with a similar anelastic strain recovery test performed in S0, pure alumina, at 78 MPa. The alumina showed a recovery of 1.2% of the total strain. Thus the composite basically recovered the same negligible amount of strain as the monolith.

5.6.4. Dilatometer test.

The dilatometer test revealed a dimensional change, perpendicular to the HP direction, in both S30 and Q30 composites during a stress free dwell at 1250°C. Figure 5.25 shows the results of the test (curves "S30" and "Q30") and the numerical derivatives of the experimental curves with respect to time (curves "d(S30)" and "d(Q30)"). The dimensional change was much larger in the S30 composite than in the Q30 one. Initially, the Q30 curve shows an increase in strain rate until 1x10^{4} sec, then followed by a decrease, reaching towards zero, and the dimension of the sample remains essentially unchanged after 4x10^{4}sec. On the other hand, the S30 curve shows an initial rapid increase in strain rate until 1x10^{4}sec, then there is a period of an almost constant strain rate until 3x10^{4}sec, then again an increasing strain rate rapidly changing to a decreasing strain rate around 7x10^{4}sec. Assuming the decrease in strain rate continues, a zero strain rate would be expected at 1.2x10^{5}sec for the S30 composite.

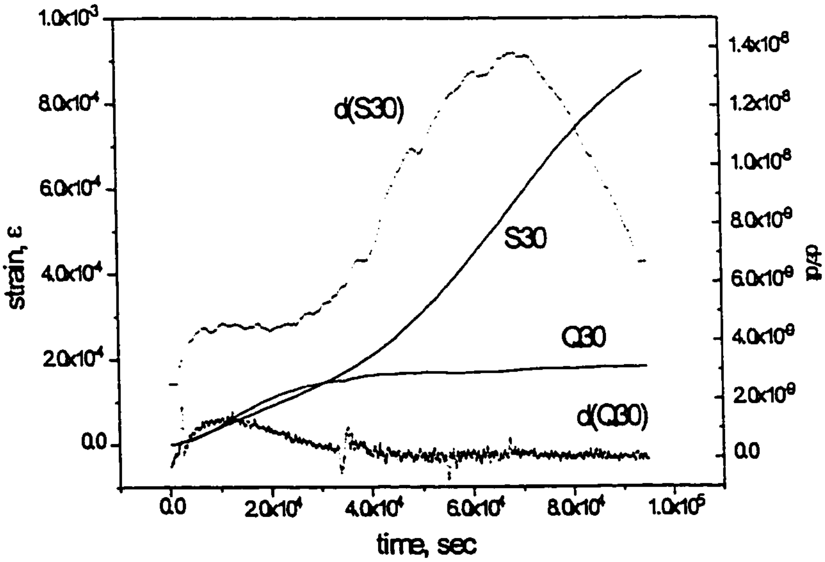

Figure 5.25. Results from dilatometer test on S30 and Q30 composites.

5.6.5. Strain rate vs. stress curves.

The lack of steady state creep complicates the analysis of the stress dependence of the strain rates. Since the strain rate can be a function of strain and/or time, a criterion must be set in order to determine the strain rate that will be used to plot stress vs.strain rate curves and calculate the creep exponent. As there is a clear time dependency in the S30 composites, a time criterion is appropriate. Thus all strain rates, for all materials, were calculated in the vicinity of $t=4x10^5$ sec, in the absence of failure. When failure occurred, the strain rate was calculated immediately before the onset of tertiary creep. When measured in compression, those strain rates are plotted on the graphs. However, the creep exponents were calculated only from the flexure data. In all flexure cases the maximum strain was lower than 5%. Thus Chuang's (1986) correction for creep asymmetry between compression and tension was not used. Each plot of Figure 5.26 corresponds to one type of processing used, thus the effect of different SiC platelets loading on the strain rate can be better viewed. In Figure 5.27, the same data is used but each plot corresponds to a certain SiC volume fraction thus the effects of different processing methods can be better seen.

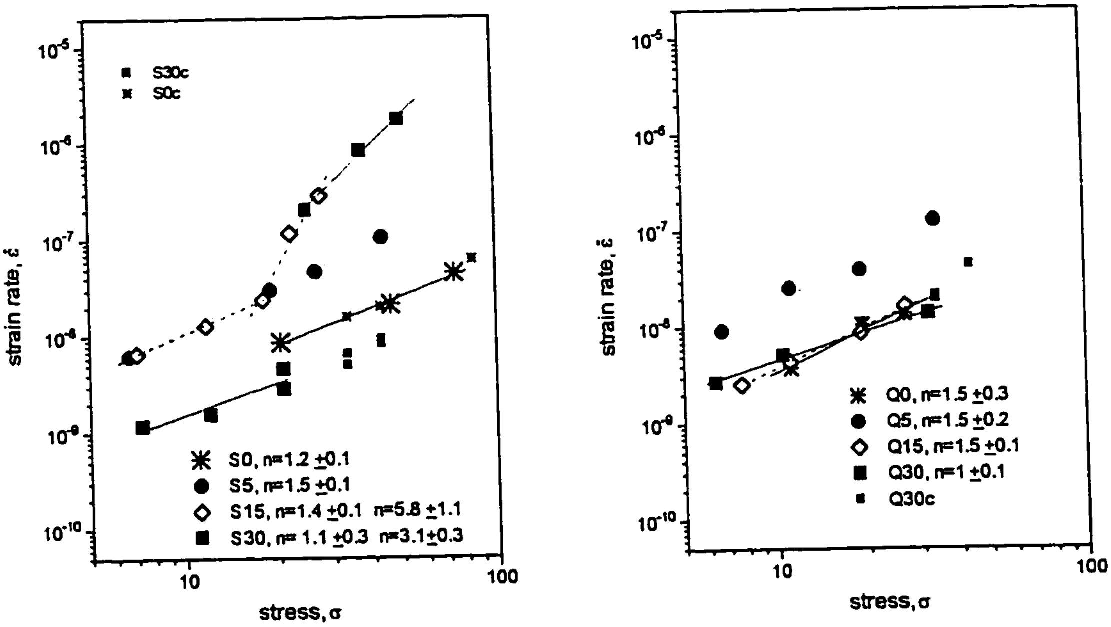

Slip cast S.

Slip cast Q

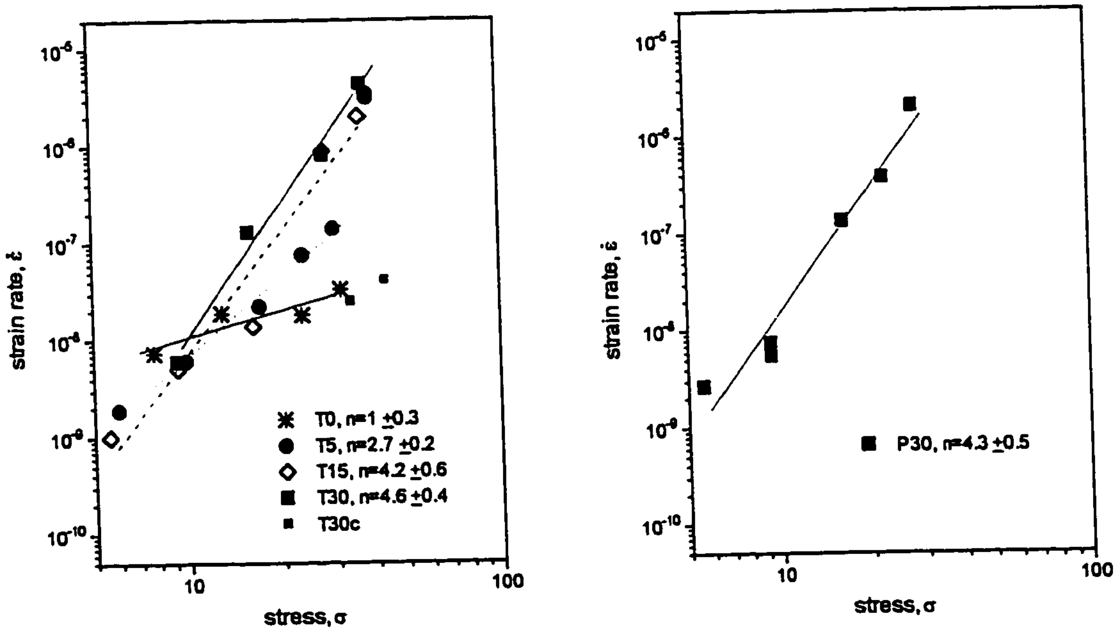

Tape cast T

Tape cast P

Figure 5.26. Strain rate vs.stress plots, for the different processing methods. The data labeled with "c" comes from compression tests. All stresses in MPa and all strain rates in s^{-1}.

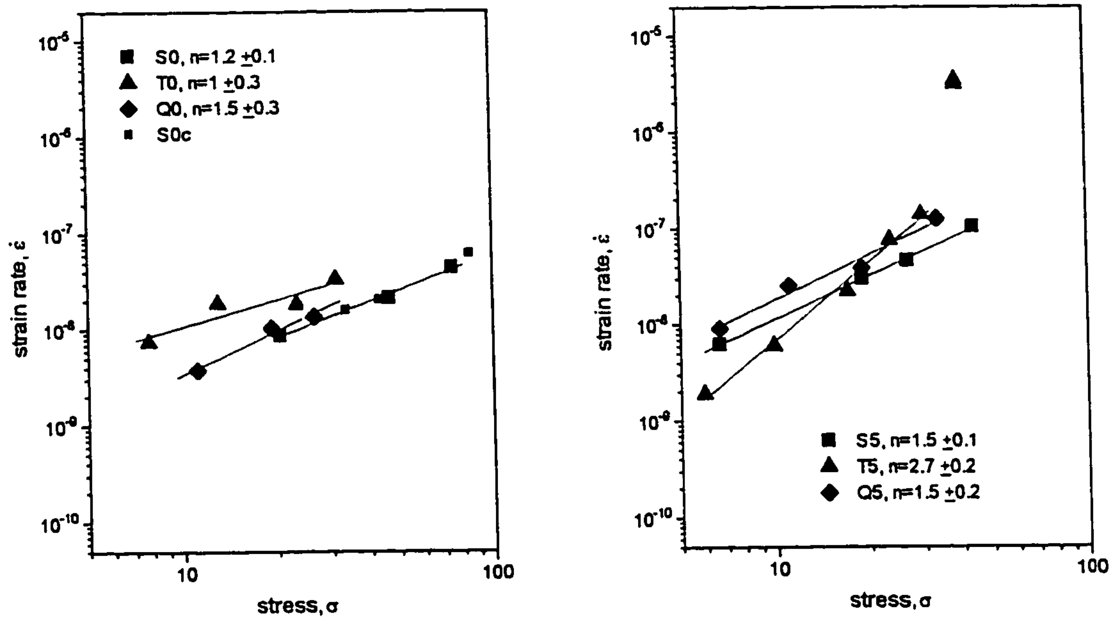

Alumina

5% SiC

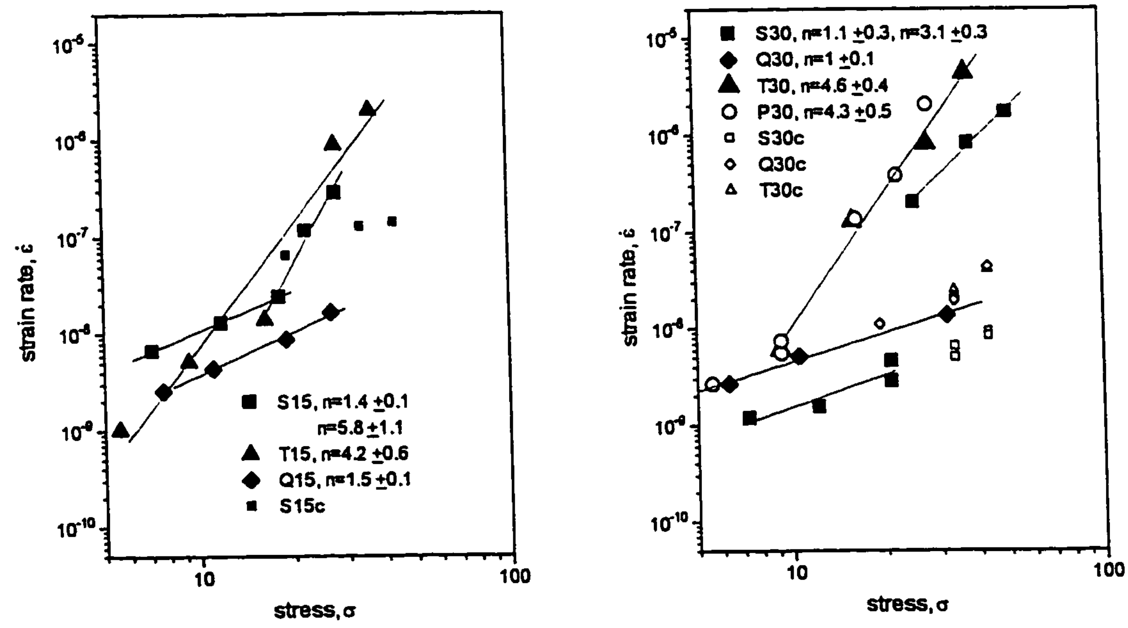

15% SiC

30% SiC

Figure 5.27. Strain rate vs.stress for the different volume fractions. All stresses in MPa and all strain rates in s^{-1}. The data labeled with "c" comes from compression tests.

It is interesting to note that the "pure" alumina samples have different strain rates, depending on the green process used (Figure 5.27 0% SiC). The slip cast samples S0 and Q0 have very similar stain rates and could be regrouped in a slip cast single set of data. The tape cast alumina has higher strain rates than the slip cast ones. The compression creep tests on slip cast S samples showed similar strain rates to those obtained by flexure tests, practically landing on the same curve.

In all the S and Q composites one can find a stress region where they have essentially equal creep exponents. However the magnitude of the strain rate varies. The S15 composites presented relatively high strain rates which are probably due to the presence of a glassy phase and graphite at the alumina/SiC interfaces (Figure 5.8).

Several composites show a change in creep exponent or mechanism. In the case of the T5 composites, they show a change of creep exponent in the region of 50 MPa. In that case, the last two data points were not used to calculate any creep exponent.

5.7. Neutron diffraction measurements (30vol% SiC composites).

5.7.1. Texture.

As -processed composites.

The neutron diffraction texture results of the as-processed 30 vol% SiC samples, are shown in Figure 5.28. The vertical axis is normalized to a random distribution of platelet orientation, thus the value represents multiples of that case. It strictly corresponds to a relative volume and not to a relative number of platelets, as the customary label "relative frequency" could imply. The relative volume of platelets will be equal to the relative number of platelets only if the orientation is independent of the particle size. The tape cast samples (T30) have the strongest texture, followed by the slip cast (Q30) composites, and lastly, the granulated slip cast (S30) and granulated tape cast (P30) have very similar overall anisotropy. The texture of the S30 and P30 is mainly attributable to the uniaxial cold and hot pressing during processing.

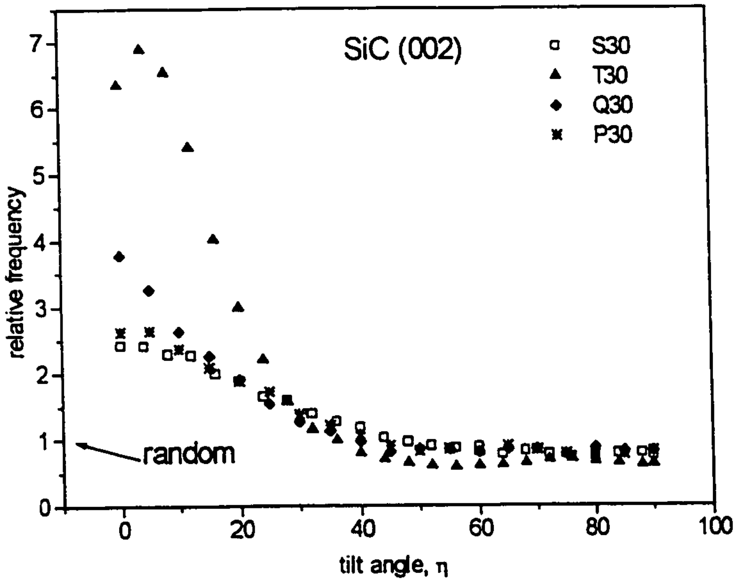

Figure 5.28. Texture of as-processed samples. A tilt angle of zero represents platelets whose c-axis is parallel to the HPA.

The overall textures of the S (granulated slip cast) and the P (granulated tape cast) are practically indistinguishable. However, from optical micrographs it is possible to observe that at a smaller scale the composites are quite different. The P composites are formed by domains of oriented platelets which likely correspond to the granules used to make the composites.

Change in texture after creep.

The S30 and Q30 texture graph on Figure 5.29 compares as-processed samples, with crept samples. It shows the compression samples have become less textured, i.e. more random, during creep. This result strongly suggests that platelet rotation took place during deformation.

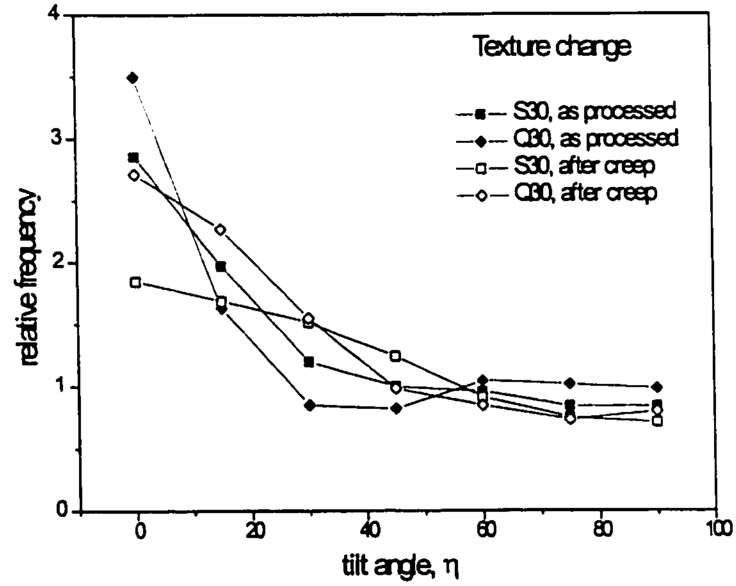

Figure 5.29. Change in texture between the as-processed and after creep composites.

5.7.2. Internal strain and FWHM.

The effect of processing on the internal strains and the FWHM (Full Width Half Maximum), of the corresponding peaks, is shown in Figures 5.30a-d. The data is plotted in two different sets mainly for clarity The data was obtained on two different occasions and it is divided accordingly. Figures 5.30a-b correspond to the S, Q and P (on the P composite only the SiC (002) was measured) composites and Figures 5.30c-d correspond to the S and T composites. The following can be noted:

-In all cases the absolute value of the strain increases with the tilt angle.

-The strain values seem to be independent of texture in the case of the SiC (002).

-The FWHM of the (002) SiC peaks depend on tilt angle and are larger in the S composite than in the Q, T or P.

-The FWHM of the Al_2O_3 peaks do not depend on tilt angle or type of composite.

The effect of annealing and creep, for the S30 and Q30 composites, on the strains and the FWHM is illustrated in Figure 5.31a-b.

-The strains change only in the S sample after a deformation of ε=16%, which was probably accompanied by a non negligible amount of damage.

-The FWHM of the SiC (002) in the S composites decreases after annealing and after creep. No change is apparent in the Q composites.

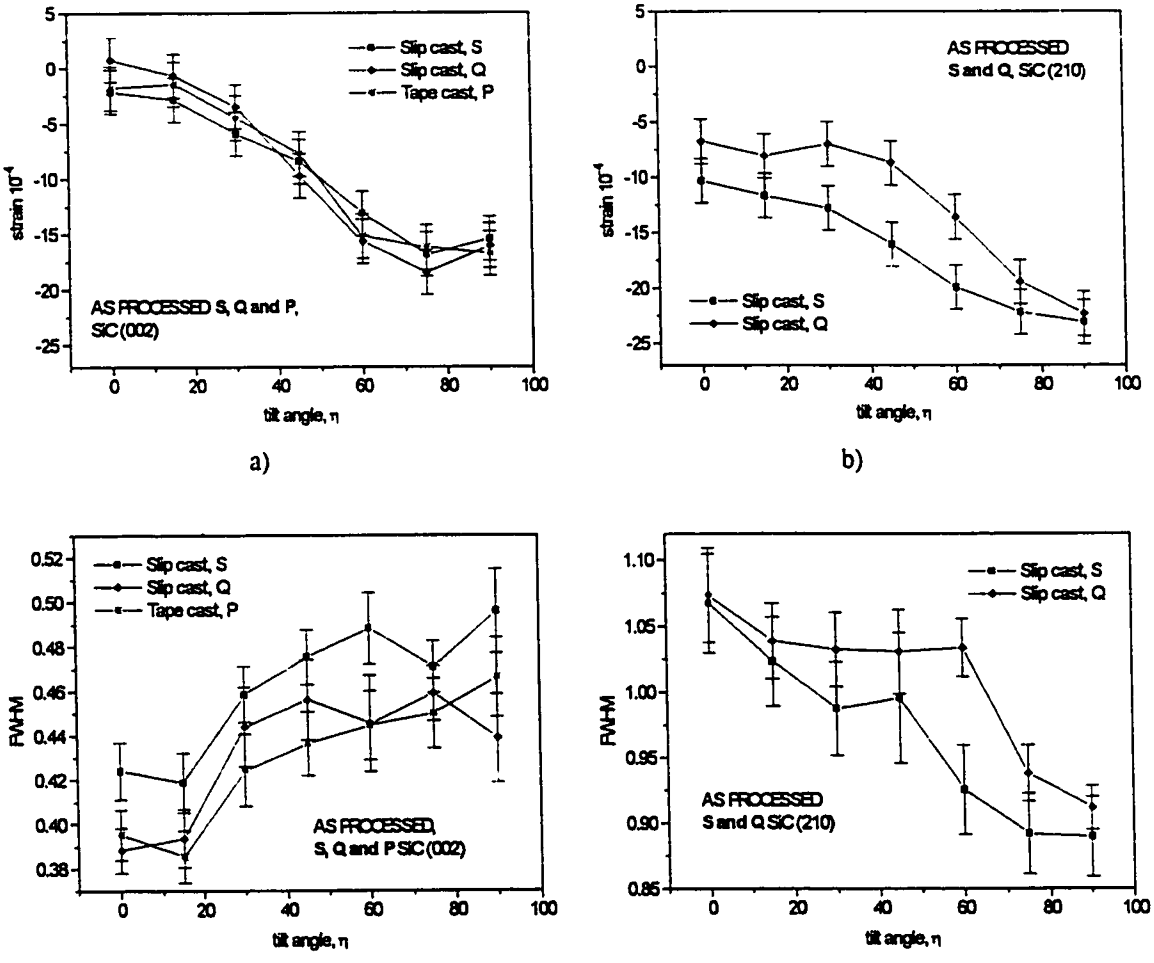

a)

b)

c)

d)

Figure 5.30a. Effect of processing on strains and FWHM in SiC.

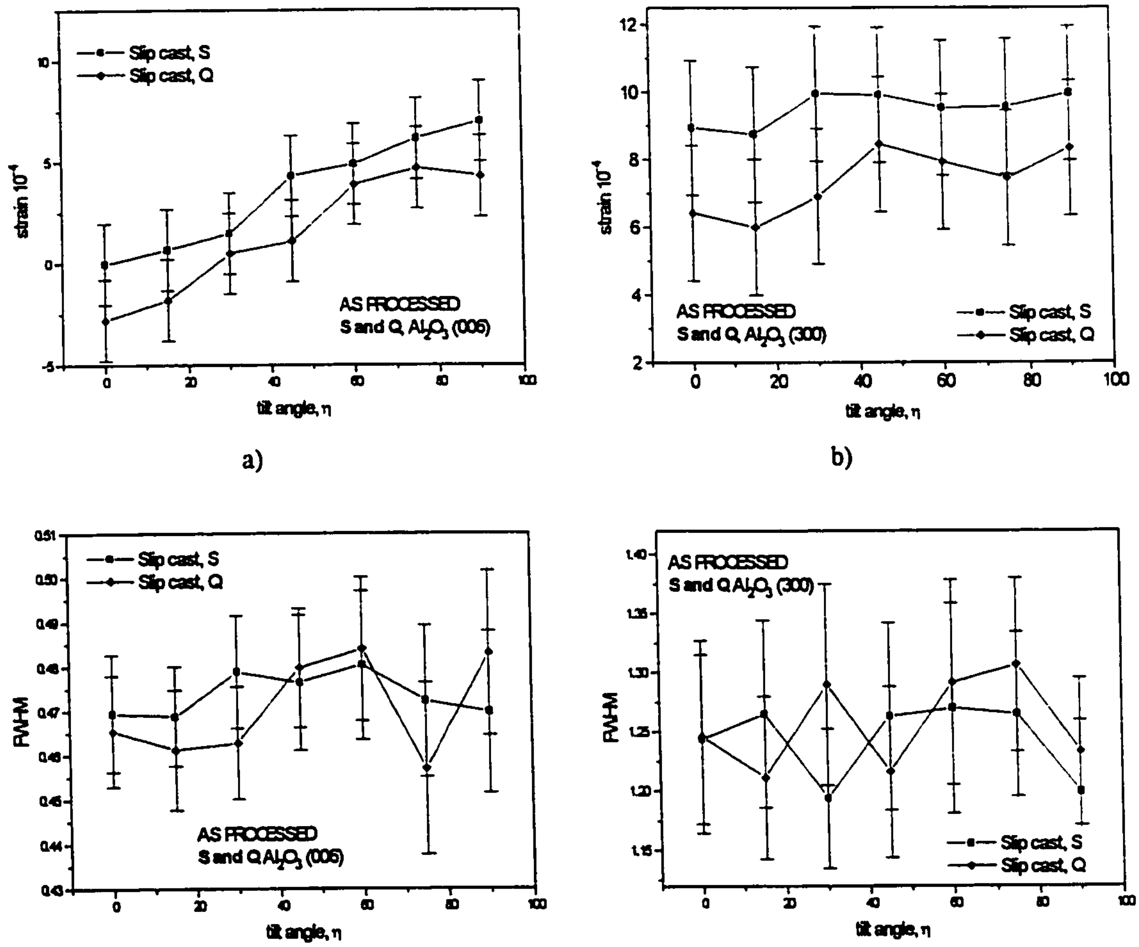

a) b)

c) d)

Figure 5.30b. Effect of processing on strains and FWHM in Al_2O_3.

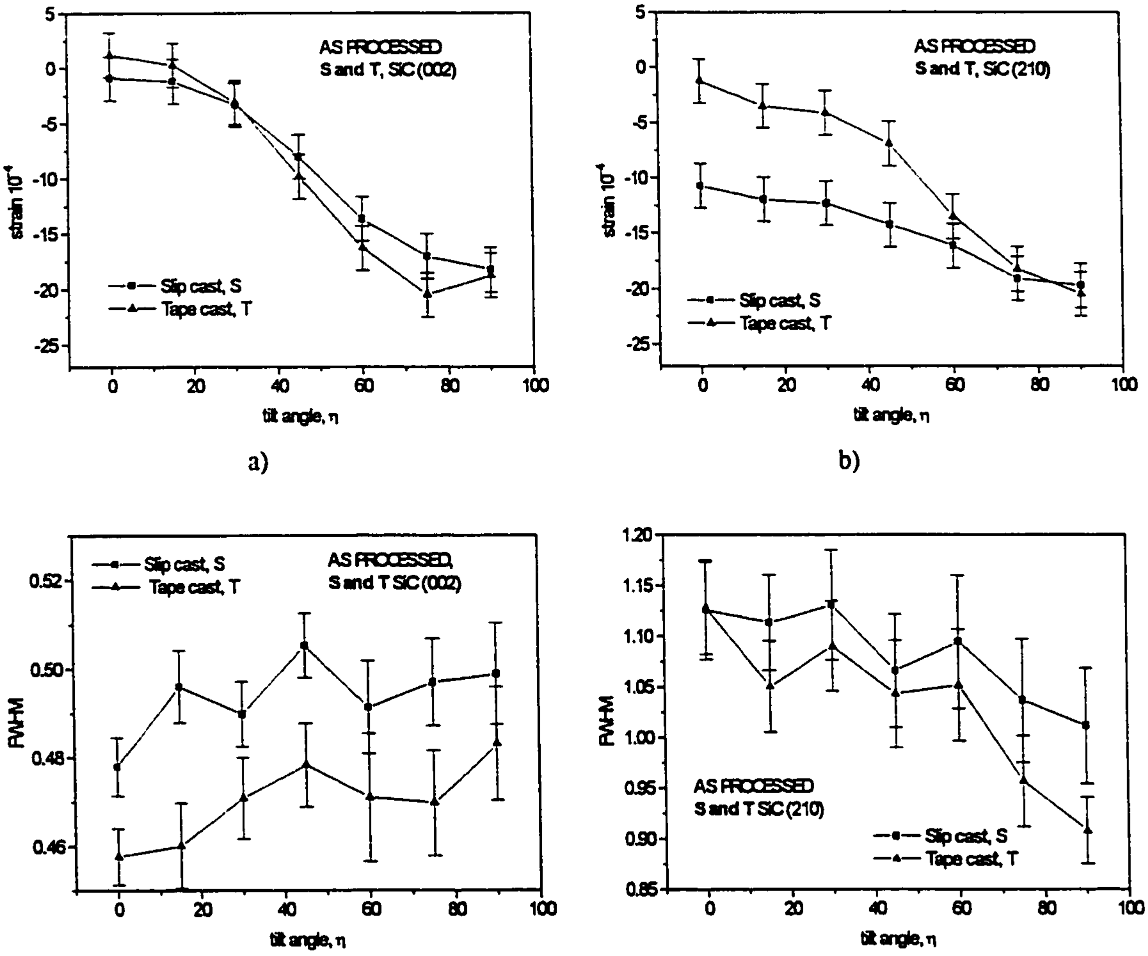

a)

b)

c)

d)

Figure 5.30c. Effect of processing on strains and FWHM in SiC.

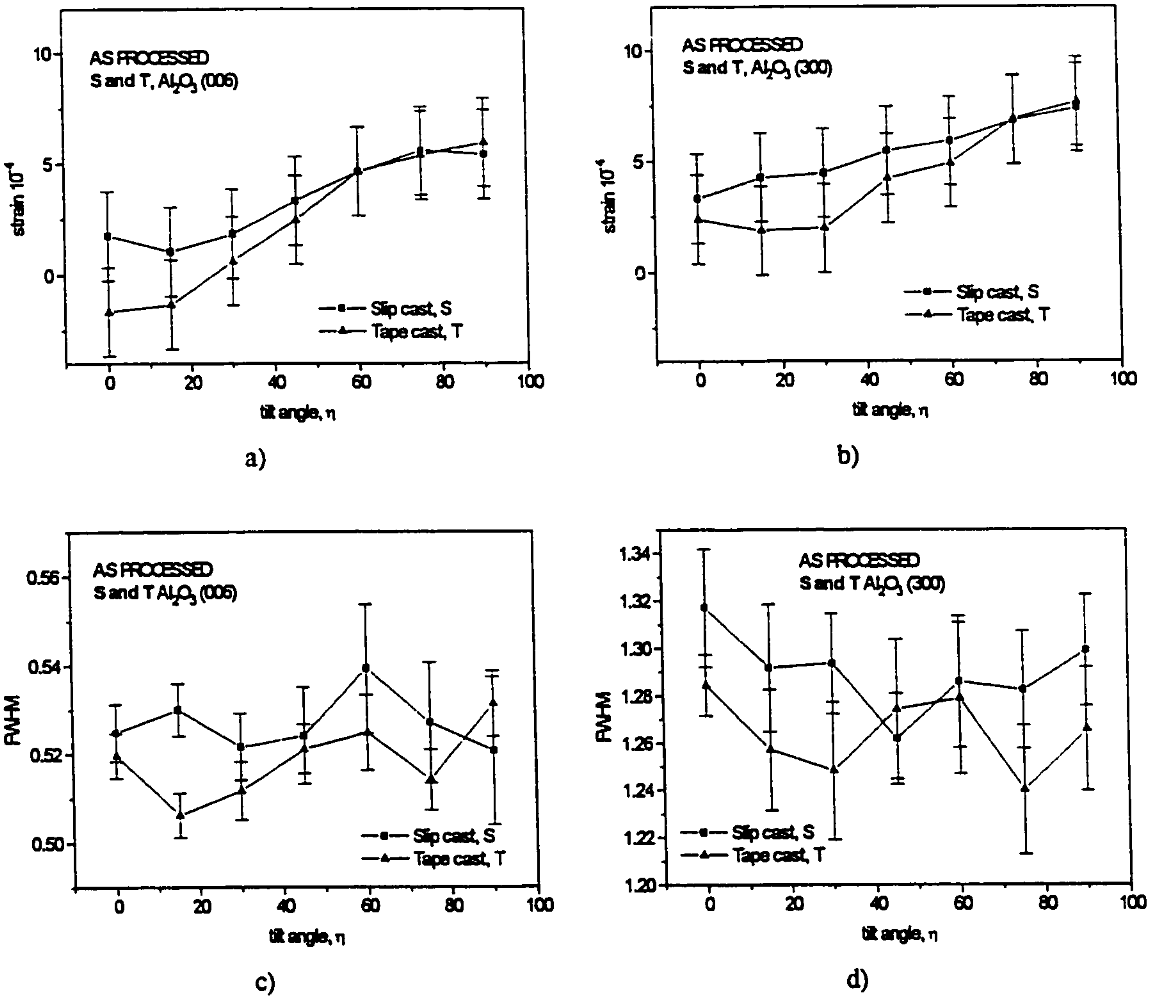

a)

b)

c)

d)

Figure 5.30d. Effect of processing on strains and FWHM in Al_2O_3.

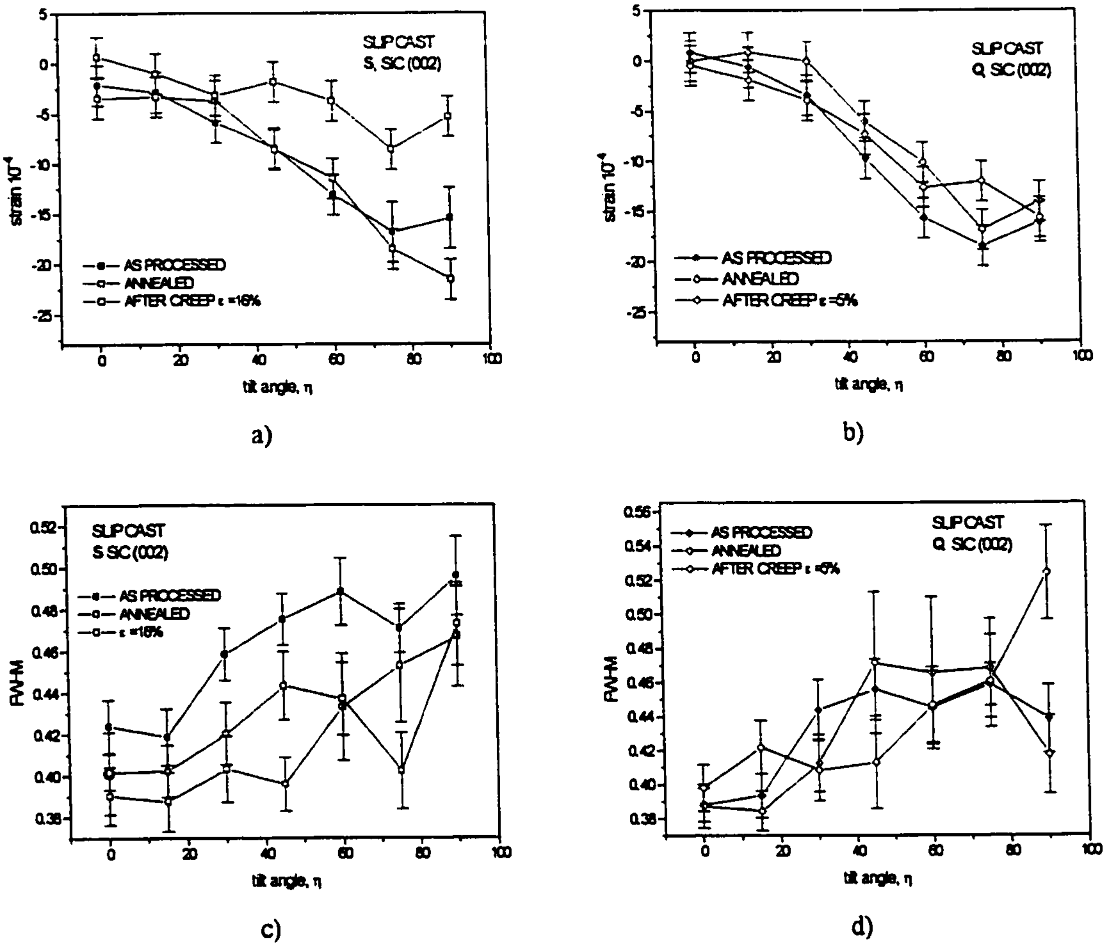

a)

b)

c)

d)

Figure 5.31a. Effect of annealing and creep on strains and FWHM.

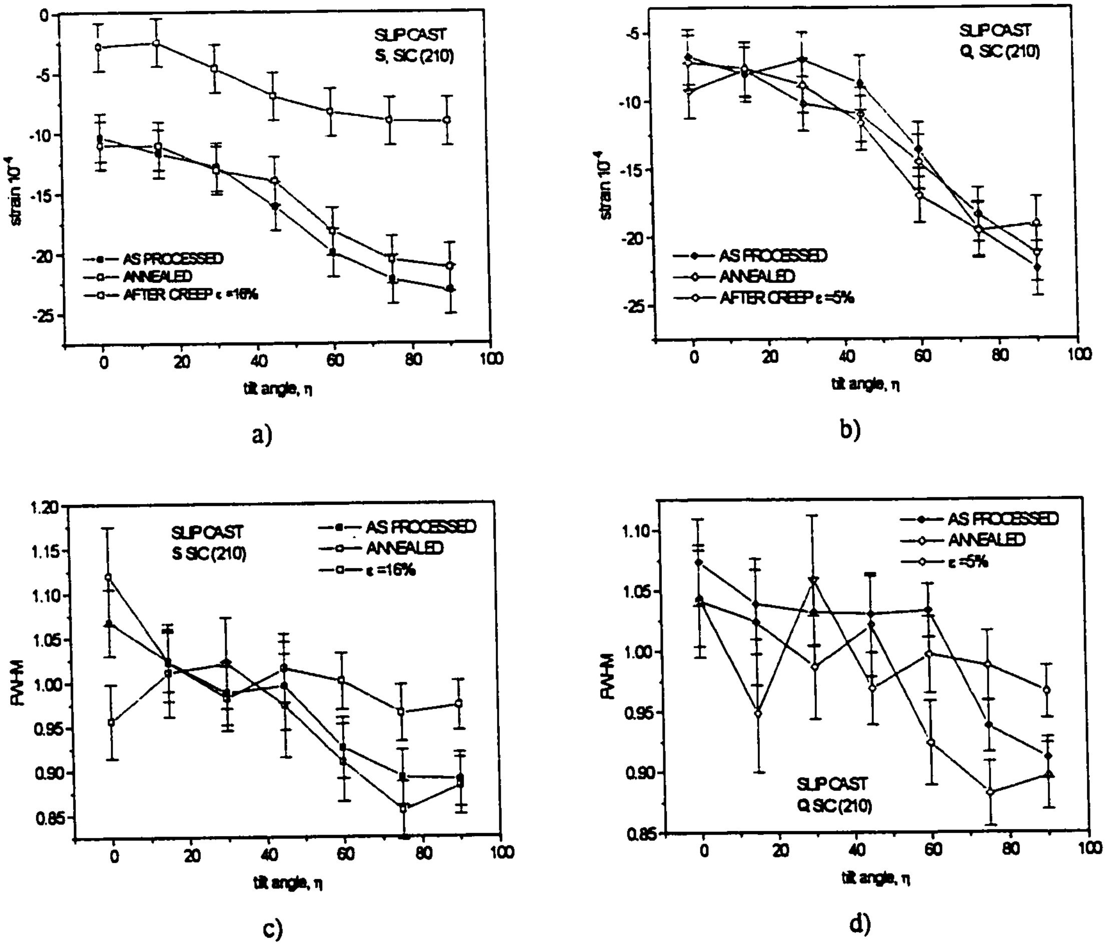

a) b)

c) d)

Figure 5.31b. Effect of annealing and creep on strains and FWHM.

6. DISCUSSION.

6.1. Introduction.

This chapter is divided in smaller specific discussion topics which follow the Results chapter sequence, whenever possible, thus providing a logical order to the contents. Some sections make use of relatively elaborate calculations which cannot be found in the literature. In these cases, the calculations are explained in the thesis Appendix. Then only the results are given in this chapter so as to not distract from the main purpose of the discussion. The summary section puts together all the information discussed in the chapter and it provides an overview to the most relevant information obtained.

6.2. Influence of green processing on impurities.

The sources of impurities in samples are mainly the starting powders and the green processing used to fabricate them. During processing, contamination is practically unavoidable due to the mixing of ceramic powders with different chemicals, and the inevitable slurry contact with tools and moulds. As a result, the level and type of contamination in different samples will vary. For example, Wereszczak et al. (1993) measured chemical distributions on silicon nitride/silicon carbide whisker interfaces. These distributions were found to be process-dependent.

In this work, two types of green processing were used: slip casting (aqueous) and tape casting (organic solvents). The analyzed tape cast samples presented a larger number and quantity of contaminants than the slip cast ones, as shown in Figures 5.5 and 5.15. This is to be expected, as the tape casting process involves longer ball milling times (during which material from the milling media and container grinds off into the slurry) and the use of a larger variety of chemicals. The impurities found, such as Ca, Mg, Mn, Na and Fe, promote glass formation (Becher and Tiegs 1988) in SiC/Al_2O_3 composites. Thus the larger quantity of impurities present in the T samples is likely the cause of the increased presence of amorphous phase found in the T30 composites as compared with the slip cast S30 and Q30 composites (Figures 5.7 and 5.11). Similar results have been obtained by Chowdhury et al. (1995) where the Al_2O_3/SiC whisker interfaces synthesized without sintering aids, were directly bonded and did not exhibit an amorphous interface phase. In general, a structurally clean interface can be associated with a chemically clean interface (Wereszczak et al 1993). It must be noted that some of the foreign chemicals found in the samples were acquired after processing. Apart from the obvious ones, such as the Au detected on Au-coated samples or the Ar in Ar-ion milled TEM samples, it is also possible that contamination occurred during creep. For example, Mg was detected on the surface of crept samples. However, it was not detected in the samples made from the bulk of the crept specimens, suggesting that the presence of Mg on the external surfaces is due to contamination during creep.

6.3. Influence of impurities on creep rates.

The influence of contaminants on the creep rates of the monolithic material is well illustrated on the "Alumina" graph of Figure 5.27 which shows strain rate vs stress plots for S0, Q0 and T0. The slip cast alumina (S0 and Q0) samples show practically the same strain rate dependence on the stress, whereas the strain rates of the tape cast material T0 are systematically higher by about a factor of two. Since the same batch of alumina powder was used for all materials, they were sintered in the same conditions, and their average grain size is practically the same (Table 5.1), the difference in strain rates between tape cast and slip cast materials must then be largely due to the different impurities acquired during processing. The impurities present in the T0 material apparently facilitate deformation and increase the creep rates. The likely mechanism for the increased strain rate is the change in grain boundary structure and ionic mobility associated with the impurities. The higher impurity concentration facilitates the diffusion of atomic species favoring deformation. On the other hand, there seems to be no influence from the green processing on n, the creep exponent, as the difference in the n values is within the experimental error. The n value close to one suggests diffusion as the prevalent creep deformation mechanism.

In the case of the composites, as explained in section 6.2, an increased concentration of impurities translates into an increased amount of glass in the as-processed and crept materials (Figures 5.7 and 5.11). These results are in agreement with studies conducted by Becher and Tiegs (1988) on the oxidation of alumina 20 vol% SiC whisker-reinforced composites. Their results indicate an increased glass formation in lower purity alumina composites.

From the "Tape cast T" graph on Figure 5.26, it is clear that the T30 composite shows higher creep rates in flexure than in compression. Thus a tension/compression creep asymmetry exists. The difference between compression and flexure creep rates, the presence of an amorphous interfacial layer, and the association of higher creep exponents (n>2) with cavitation strongly suggest cavitation as an important creep deformation mechanism in the flexure tape cast composites. In addition, from the graphs of Figure 5.26, the tape cast composites (T and P) exhibit higher creep exponents (tested in flexure), $2.7>n_{tape}>4.6$, than the slip cast ones (S and Q), $1>n_{slip}>1.5$ at lower loads, suggesting the occurrence of different creep mechanisms. Therefore, the effect of the increased impurity content in the tape cast composites as compared with the slip cast ones is mainly the increased glass content and the subsequent cavitation creep mechanism. This is in agreement with the TEM results on crept T30 and S30 samples (Figures 5.10, 5.11, 5.12, and 5.14). Even though the samples were deformed to the same strain (Figure 5.9), the tape cast samples show more cavitation (Figure 5.10) than the slip cast ones.

6.4. Effect of SiC volume fraction on creep.

During deformation of the composites -in air and at high temperatures- the presence of SiC particles in an alumina matrix has two main effects: 1) a mechanical influence (the original reason for adding them!) and 2) the occurrence of oxidation reactions and the resulting formation and/or growth of an amorphous phase. The first effect tends to decrease the creep rates. The second effect can be assumed to increase the creep rates -in general, the presence of a grain boundary glassy phase in alumina ceramics will increase the deformation rates (Jakus et al 1986)- and will be referred to as the "non-mechanical effect". This latter effect clearly has a strong influence on the mechanical behaviour of the composites as it will cause an increase in diffusion and enhance cavitation. Thus the term "non-mechanical" was chosen based on the origin of the phenomenon and is not intended to imply anything about its consequences. Both effects tend to become more important as the SiC volume fraction increases and can have a comparable influence on the creep rates depending on the type and volume fraction of the reinforcement. However, either the mechanical or the non-mechanical effects can be more important at different volume fractions.

The mechanical effect of the SiC in the 5% composites is expected to be small due to the low volume fraction. An estimation of this effect can be made using the Wilkinson-Pompe model for creep of ceramic composites (Wilkinson and Pompe 1997). From equation 2.16 the increase in viscosity in the material due to the added rigid particles can be calculated. Assuming the platelets are aligned,

$$\frac{\eta_{\text{reff}}}{\eta_o} = 1 + 2.5\frac{\phi}{1-\phi} = 1.13 \qquad (6.1)$$

and assuming the platelets are randomly oriented,

$$\frac{\eta_{\text{reff}}}{\eta_o} = 1 + 2.5\left(\frac{\lambda}{\pi} + \frac{1}{2}\right)\phi = 1.56 \qquad (6.2)$$

where $\phi=0.05$ is the SiC volume fraction and $\lambda=10$ is the average platelet aspect ratio. The effect is, indeed, very modest. From these values and Equation 2.15, the strain rate is expected to decrease by the same factor. An estimate of the influence of the SiC "non-mechanical" effect may be obtained by comparing the 5% SiC composites with the expected creep behaviour i.e. the mechanical effect. As an example, it is convenient to consider the Q material as the S material has essentially the same behaviour and the T material has a change of n which complicates the analysis. Using Equation 6.2, the expected mechanical effect of adding 5 vol% platelets to the Q alumina matrix would be to decrease the creep rates as illustrated in Figure 6.1 . Then the non-mechanical effect of the added platelets can be estimated by comparing Q5 expected behaviour with its experimental behaviour. The non-mechanical effect is then to increase the strain rates by almost one order of magnitude.

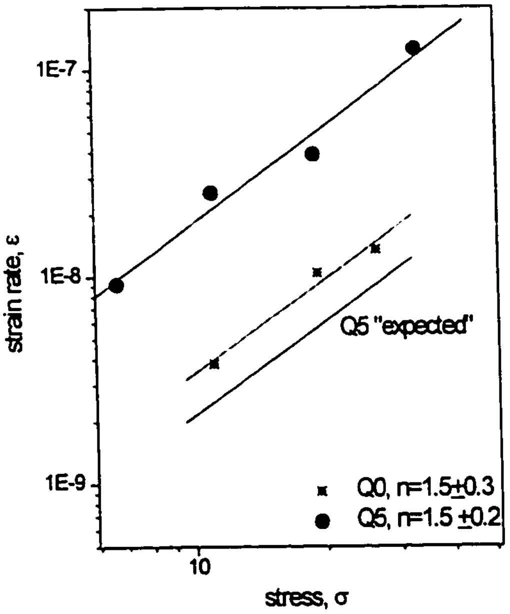

Figure 6.1. Expected mechanical influence from adding 5 vol% platelets to the Q alumina matrix.

The T5 composites display lower strain rates than the alumina at low stress, but higher creep rates at high stress (Figure 5.26 "Tape cast T" graph). It is possible that the increased silica content (due to the platelets) is not significant for the low loads as there is already a fair amount of impurities in the alumina from green processing. Thus the analysis of the observed strain rates is not as straightforward as in the other composites. In addition, the creep exponent is higher (n_{T5}=2.7, n_{T0}=1) than for alumina, suggesting a different creep mechanism associated with cavitation. At loads of about 40MPa, the T5 creep mechanism seems to change. It is worth noting that in graph "5% SiC" Figure 5.27, there are two data points (not used in the calculation of n_{T5}) with the largest apparent strain rates. Their high strain rates indicate a change to a larger creep exponent; in addition, these samples failed in less than 1 hour (as compared to 1 week without failure for most of the samples) thus suggesting extensive damage at this high stress. The SiC and impurities favoured glass formation and this, in turn, promoted damage and cavitation leading to fracture.

At higher platelet volume fraction the mechanical effect has the added complication of the interaction between particles. In addition, as the volume fraction of platelets increases, the oxidation effects become more important. Thus, differentiating between the mechanical and the non-mechanical effects becomes more difficult as the reinforcement volume fraction increases. However, an estimation of the non-mechanical effect for the 15 and 30% composites can be made by using the calculated effect for the 5% composites. As the softening of the matrix likely increases with the volume fraction, the 5% matrix viscosity (softened due to platelets addition) estimate can provide a lower bound estimate for the non-mechanical effect. Thus, in order to better asses the mechanical effect of the platelet additions to the alumina, one can first estimate the creep resistance of the matrix material (i.e. glass-boded alumina) within the composites taking into account the non-mechanical effect of platelet additions. Thus, the composite matrix alumina creep rates are an order of magnitude higher than the experimentally measured ones for the monolith. When comparing the composite creep rates with those of the matrix alumina the main difference is now the mechanical effect and the propensity to cavitation due to platelet additions. This is clearly approximate but it does provide a means to differentiate the mechanical and the non-mechanical effects and rationalizes the relatively high strain rates measured in the 5% platelet composites. Assuming the effect is similar in the S and T composites, the strain rate vs stress plots with the apparent matrix creep added are illustrated in Figure 6.2.

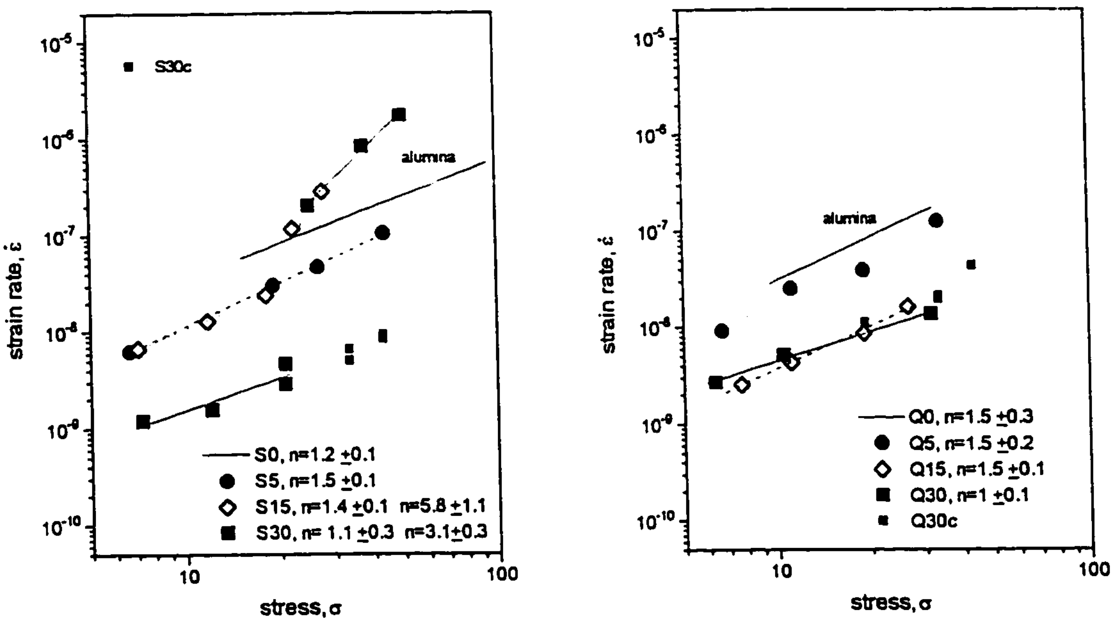

Slip cast S

Slip cast Q

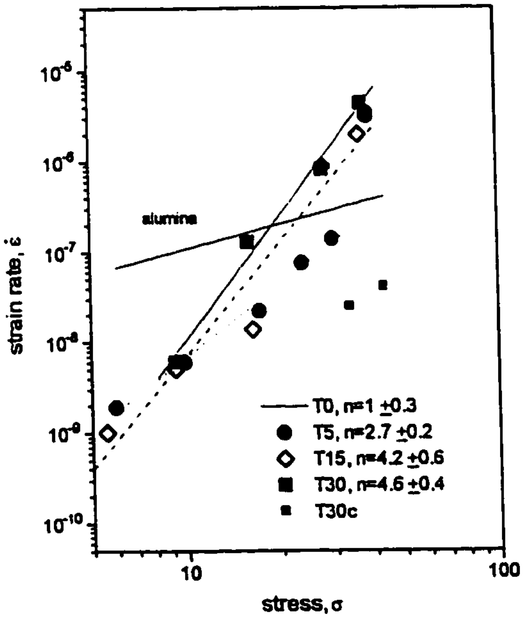

Tape cast T

Figure 6.2. Strain rate vs. stress plots for the different processing methods considering a softened alumina. All stresses are in MPa and all strain rates in s^{-1}.

In the case of the S material, the effect of adding 15% SiC could not be determined, as HREM showed that the samples were contaminated. The as-processed S15 samples showed relatively thick layers of glass and graphite at SiC/alumina interfaces. This likely increased the creep rates as compared to uncontaminated glass- and graphite-free samples. However, at low stresses, the relevant creep mechanism for S15 is the same as for alumina and S5, as the creep exponents are similar $n_{S15}=1.4$, $n_{S5}=1.5$. The low creep exponents suggest that diffusion is the main creep mechanism. From the graphs in Figure 6.2 it can be observed that there is a change of creep mechanism at stresses of about 20MPa, as there is an increase in creep exponent from 1.4 to 5.8. Within the S material, the lowest creep rates are those of S30, at stresses lower than 20 MPa. Beyond this load, S30 presents a change in creep exponent from 1.1 to 3.1. The higher creep exponents are likely associated with cavitation. This agrees with the compression creep results where cavitation is expected to be less important. In the compression samples, at loads higher than 20 MPa, the creep rates continue to fall onto the same line as the flexure data for lower loads. The data from lower loads in flexure and compression suggests a diffusion creep mechanism.

For the Q material, 15% and 30% SiC composites have essentially the same creep rates. It would seem that adding more than 15% platelets has no effect on the creep rates. However, it is clear that there is a difference in creep behaviour between Q15 and Q30 as can be seen from the strain vs time curves of Figure 5.20. Q30 has a lower total strain, as compared with Q15. The differences occur primarily in the first stages of creep, when the samples deform rapidly. One can speculate that a platelet network would be more rigid and better formed in Q30 than in Q15 and thus more difficult to deform. Though the creep behaviour is initially different, the strain rates become very similar at longer times. However, there is a small difference in the creep exponents ($n_{Q15}=1.5$ and $n_{Q30}=1$) which suggests the possibility of significantly different creep rates at higher loads. Due to the limitation on strain imposed on the bending experiments (to avoid a large uncertainty in calculating the stresses and strains in flexure) and on the compression experiments (to avoid barreling), no tests were performed at higher loads.

In the tape cast material T the presence of platelets caused a change in the creep exponent from $n_{T0}=1$ to $n_{T5}=2.7$, $n_{T15}=4.2$ and $n_{T30}=4.6$. The HREM results show a propensity to cavitation in the T30 compression samples, even in compression where cavitation is limited. In addition to this, the large difference between the compression creep rates and the flexure creep rates of the T30 composites strongly suggest cavitation as an important creep deformation mechanism. It is interesting to note that, as for the Q composites, the T15 and T30 materials have very similar creep rates and creep exponents (N.B. Figure 6.2 shows 5 data points for the T15 sample, the data points to the right are difficult to see as one is "behind" a T30 data point and the last one would seem part of another data set). Furthermore, similarly to the Q composites the total strain in the 30% composites is lower than in the 15% for similar applied load and time.

6.5. Influence of texture on creep.

The influence of texture on creep is best seen when comparing composites made with similar green processes but different textures. Disregarding the S15 composites (where an amorphous phase and graphite were found at alumina/SiC interfaces), the discussion will be divided in: a) slip cast composites, S and Q, and b) tape cast composites, T and P.

6.5.1. Slip cast composites.

The creep exponents of the S5 and Q5 composites are essentially the same, $n_{S5,Q5}=1.5$. Yet, the strain rates in Q5 are somewhat higher (Figure 5.27, 5% SiC). The same behaviour is observed, at loads lower than 25MPa for the S30 and Q30 composites, $n_{S30}=1.1$, $n_{Q30}=1$. The strain rates are consistently higher for Q30 than for S30 (Figure 5.27, 30% SiC). The low creep exponents suggest diffusion controlled creep. The lower creep rates in the S5 composites can be rationalized by the Wilkinson-Pompe model for platelet rotation during creep. Indeed, equations 6.1 and 6.2 predict a small decrease in creep rates in a 5% platelet randomly-reinforced composite as compared with an aligned one. Experimental evidence of the occurrence of platelet rotation during creep is presented in Figure 5.29 which shows the change in texture of as-processed and crept samples. The data was obtained from 30 vol% composites, however this mechanism must also exist in the lower volume fraction composites S5 and Q5 where platelets can rotate with increased ease.

At higher volume fractions, however, interactions between platelets become more important and the rotation model cannot be directly applied, as this assumes the independent rotation of each particle. If the difference in creep rates of the Q30 as compared with the S30 composites is mainly related to their platelet network morphology, then the S30 network must be more rigid and difficult to deform. In general, the more textured the reinforcement, the less likely to form a strong interacting network (Munson-McGee 1991). The interactions between platelets in S30 must account for the lower creep rates found. It is difficult to qualify and quantify the extent of interparticle interactions. However, evidence of a more or less rigid network can be obtained by looking at the rotation of platelets during creep. In an effectively interacting network the rotation of particles can be expected to be more difficult. The particles cannot rotate or move easily past each other as they are constrained by the surrounding particles, as illustrated in Figure 6.3. From the texture graph on Figure 5.29, of the as-processed and crept S30 and Q30 samples, the change in platelet average tilt angle was numerically calculated. The crept samples were compressed perpendicular to the HP direction and became less textured. In the case of S30, the average value of the tilt angle changed by $\Delta\eta_{ave}$=2°. In the case of Q30, this angle changed by $\Delta\eta_{ave}$=7°. Therefore, the platelets in Q30 were freer to rotate suggesting the existence of weaker platelet-platelet interactions than in S30.

At loads higher than 25MPa and in flexure, S30 shows a change in creep exponent to n_{S30}=3.i while the Q30 exponent remains the same. S30 deforms at faster strain rates than Q30 at these higher loads. The higher creep exponent is usually associated with cavitation and damage, suggesting there is a disposition to cavitation from the more random texture of S30. This propensity to cavitation can also be due to the more rigid network in S30. As the sample deforms, the platelets cannot easily rotate, translate or slide past each other to better accommodate the farfield strain leading to damage. This is in agreement with Lin and Becher's (1991) observation on the cavitation of SiC whisker reinforced alumina. They found that, in general, the higher whisker content composites exhibited a higher density of cavities. As the volume fraction of whiskers increases the network becomes more rigid, less accommodating, and more inclined to cavitation.

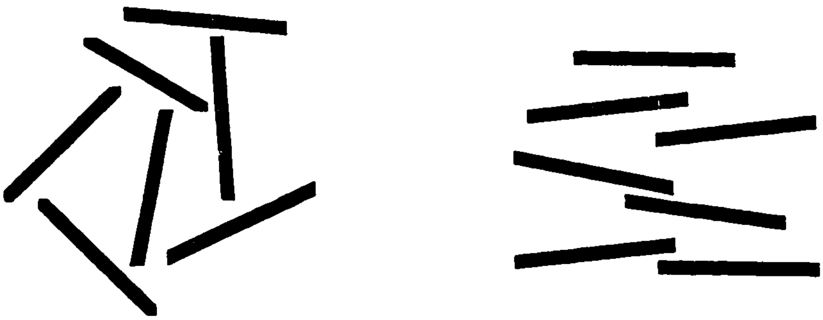

a) The rotation and translation range of the particles is strongly limited by their neighbours.

b) Most of the particles have a wider range of rotation before impinging onto a neighbour.

Figure 6.3. Schematic of platelets in a)S30 and b) Q30. The platelets in S30 tend to form higher angles with each other promoting a more rigid network.

6.5.2. Tape cast composites.

P30 and T30 have almost exactly the same behaviour in creep even though the texture data indicates a stronger difference in platelet orientation distribution than between S30 and Q30 (Figure 5.28). However, P30 has a very particular orientation distribution of platelets. The "overall" distribution is similar to that of S30, as illustrated in Figure 5.28. But from Figure 5.1, it can be seen that the P30 composite is formed by an assembly of cells or domains. Within each domain the platelets are preferentially oriented in a particular direction. Thus the majority of the platelets form low angles with each other, as in T30 and Q30. It is only at the domain boundaries that platelets form higher angles with each other where strong mechanical interaction is possible. This would suggest that the important factor in determining the creep resistance is the ability of interaction between platelets and not the angle of the platelets with the far field stress. However, the propensity to cavitation might also play an important role in the T30 and P30 creep behaviour. From the flexure tests, high creep exponents were obtained (n_{T30}=4.6, n_{P30}=4.3) which are associated with the occurrence of cavitation. In addition, from Figure 5.27 30% SiC, the T30 strain rates obtained in compression are lower than the flexure ones and similar to those of the Q30 composites. The compression samples suffer significantly less cavitation than the flexure samples during creep. Thus, in the case of the tape cast composites, their behaviour is almost certainly determined by their high glass content and consequent tendency to form cavities.

As previously mentioned, there are no clear differences between T15 and T30 strain rates, and between Q15 and Q30. At least in aligned materials, the volume fraction of platelets at higher loadings (15 and 30%) seems not to have an influence on the creep rates or creep exponent. However, since the S15 data cannot be fairly compared with the S30 data, this cannot be proven to be exclusive to the aligned materials.

6.6. S30 strain vs time creep curves.

The shape of the S30 ε vs t curves was described in section 5.6.2. The transition from a rapid strain rate to a slow strain rate is found in both flexure and in compression specimens. In flexure the creep behaviour of the composite is generally governed by the behaviour on the tensile side, suggesting the composite behaves in a similar way in tension and in compression. The transition from a rapid to a slow strain rate could be rationalized by the elastic loading of a platelet network: In the first stages of deformation, the composite deforms rapidly as the matrix deforms and platelets accommodate the deformation by small displacements and/or rotations. The deformation rate slows down as the particles approach each other, contacts are formed, and the platelet network must now deform elastically to accommodate the composite macroscopic strain. However, this does not seem to be the case. By analogy with SiC whisker reinforced alumina experiments (Porter 1988), if the platelet network was elastically loaded to a significant extent, then this could be measured by an anelastic strain recovery measurement. Figure 5.24 illustrates the results from a strain recovery test on an S30 composite. Essentially no strain was recovered, suggesting that the platelet network was not elastically loaded. This is confirmed by the neutron diffraction measurements on crept samples. If the platelet network was elastically loaded one would expect a change in the internal strains of crept samples as compared with as-processed materials (Figure 5.31). However, no evidence of internal strains change was found. In addition, if the deformation of the composite depended on the formation of an elastic network, it would be reasonable to expect a strain dependency for the onset of the slow strain rate regime. Not only was no strain dependency found but a time dependency was demonstrated by the annealing experiment illustrated in Figure 5.23. The onset of the slow strain rate regime depends on the time of exposure to high temperatures. Thus there is an initial process occurring in, approximately, the first 1.5×10^5s of exposure to high temperatures. This process does not depend on the sign of the stress applied, as it occurs in both compression and flexure tests, it appears to be strain independent, time dependent, and stress biased (regardless of the sign of the stress applied, it assists the deformation of the composite).

A dimensional change in the samples can be associated with an internal stress relaxation process occurring in the material. The S30 and Q30 composites were subjected to a stress free dwell whilst monitoring their change in length perpendicular to the HP direction. The results, illustrated in Figure 5.25, show an increase in length in both composites. However, the Q30 dimensional change occurs mainly within the first 3×10^4s and the total strain is of the order of 1×10^{-4}. On the other hand, the S30 shows a strain of 9×10^{-4}, almost one order of magnitude larger than Q30. In addition, the S30 deformation occurs throughout the time span of the dwell, clearly slowing down after 8×10^4s. In the case of S30, neither the direction nor the magnitudes of the strains or the strain rates during the dwell are comparable in magnitude to the ones in the first rapid strain rate stage of creep, Table 6.1, indicating the rapid strain rate regime cannot be directly attributed to the possible strain relaxation in the composites. It is worth noting that there is a significant difference between the dimensional change of Q30 and S30 -suggesting a more important relaxation process occurring in S30. Furthermore, the suggested relaxation time of S30 is similar to the one required for the slow creep regime onset. This possible strain relaxation process will be further discussed in section 6.7.3.

		strain	strain rate
dwell	expansion	10^{-4}	10^{-9}-10^{-8}s^{-1}
creep	compression or flexure	10^{-2}	10^{-7}-10^{-6}s^{-1}

Table 6.1. Comparison between stress-free dwell and creep of S30 composites.

6.7. Internal Strains.

All the neutron diffraction data used to calculate the internal strains is from the 30% SiC composites. Thus this section refers only to those composites.

6.7.1. As-processed.

The main origin of the internal strains in these type of composites is the difference between the coefficient of thermal expansion (α) of SiC and Al_2O_3. Considering that at the processing temperature the composite is strain-free and that $\alpha_{SiC}<\alpha_{Al2O3}$ (Table 6.2) then at room temperature (RT) the expected internal strains are compressive (negative) in the SiC and tensile (positive) in the alumina. The sign of the experimentally determined strains agrees with what was expected as shown in Figure 5.30.

		Al_2O_3	SiC	Reference
Modulus of elasticity, E (GPa).	Polycrystal	406		Lynch 1975
Modulus of elasticity, E (GPa).	Platelet		470	Claussen 1990
Poisson's ratio, ν.	Polycrystal	0.23	0.23	Lynch 1975
Coefficient of thermal expansion, α (1/°K).	Single crystal (hexagonal)		$\alpha_1=\alpha_2= 4.16\times10^{-6}$ $\alpha_3= 4.45\times10^{-6}$ (*)	Li and Bradt 1986
Coefficient of thermal expansion, α (1/°K).	Polycrystal	8.9×10^{-6}		Lynch 1975

(*) α_1, α_2 parallel to the basal plane; α_3 perpendicular to the basal plane.

Table 6.2. Alumina and silicon carbide data.

The experimentally measured strains (Figures 5.30 and 5.31) can be used to calculate the approximate temperature difference, ΔT, between the composite stress free-state and the measured internal strain state at room temperature. Using the equation obtained by Pompe and Wilkinson (1993) which models a platelet as a disk-like spheroidal inclusion with axes $a_1=a_2\neq a_3$, the average stresses in the platelets and the matrix, following a temperature change ΔT, are given by:

$$\sigma_p = -3\phi_m \frac{(\alpha_p - \alpha_m)\Delta T}{(\phi_p / K_m + \phi_m / K_p + 3/4G_m} \qquad (6.3)$$

$$\sigma_m = -\frac{\phi_p}{\phi_m}\sigma_p \qquad (6.4)$$

where σ, ϕ, K, G are the stress, volume fraction, bulk modulus, and shear modulus and the subindices "p" and "m" denote platelet or matrix respectively. Utilizing the largest measured strains ε (either the measured SiC strain or the Al_2O_3 strain can be used) in equations 6.3 and 6.4, with $\sigma = \varepsilon E$, then the calculated change in temperature is approximately 1200°C. This temperature is less than the maximum possible ΔT, the processing temperature (1650°C) minus the RT (approximately 25°C). However, this is expected because of the relatively slow cooldown from the processing temperature (Figure 3.14) which allows the relaxation of stresses during the first stages of cooling. In addition, while the main origin of the measured strains is the difference in thermal expansion coefficient between the phases, there are other factors to consider such as the texture, the shape of the particles, the anisotropic thermal expansion coefficient of each phase, the elastic properties of the materials, and the particular cooling conditions from the processing temperature. These factors probably give place to the strong dependency of the SiC internal strains with the tilt angle, shown in Figures 5.30 and 5.31. In order to elucidate the internal strain values found in the composites, the influence of the texture was considered.

6.7.2. Modelling of internal strains in a textured material.

Assuming linear elastic behaviour, Kreher and Pompe (1989) and Kreher (1990) modelled the residual stresses in homogeneous polycrystals assuming isotropic elastic constants and, of course, anisotropic thermal expansion coefficients (i.e. α varies with crystal orientation). Kreher (1993) then generalized the theory by taking into account both anisotropic crystal orientation distributions (crystallographic texture) and anisotropic morphology of the microstructure. Kreher (1996) has recently modeled the internal strain and stress fields in anisotropic composites. As the material is anisotropic, the average strain in an inclusion depends on its orientation with respect to the rest of the composite. Based on this model the average strain in the SiC platelets of the 30% composites has been evaluated as a function of their tilt angle. The following considerations and assumptions were taken:

- The platelets are modeled as plate-like spheroids with axes $a_1 = a_2 \neq a_3$, constant aspect ratio $r = a_1/a_3$ and coefficients of thermal expansion $\alpha_1 = \alpha_2 \neq \alpha_3$ (Table 6.1). The alumina is an isotropic medium with a single coefficient of thermal expansion α (Table 6.2).

- The modeled strain was that perpendicular to the basal plane, ε_3. From the experimental results (Figure 5.30), this strain -equivalent to the strain in the (002) planes- is the least sensitive to the texture of the samples and thus the least sensitive to the way the texture is modeled.
- The composites were assumed to have cylindrical symmetry. Similarly to the work of Munson-McGee (1991) the texture was modeled by a normalized orientation distribution function, $n(\eta)$, that depends only on the platelet tilt angle, η. To simplify the mathematical expressions $n(\eta)$ is assumed to have the form:

$$n(\eta)= A\cos^{m}(\eta) \qquad (6.5)$$

where A is the normalization constant and the exponent m is used to describe the degree of texturing. A value of $m=0$ would describe a randomly oriented material and a value of $m=\infty$ would describe a material with all platelets perfectly aligned in one direction. These considerations have the implied assumption that the orientation distribution of the platelets is independent of their size.
- In the case of the SiC platelets, their larger surface corresponds to their basal plane. Thus there is a strong correlation between shape and crystal orientation, i.e. a fixed grain shape is attached to the crystallographic axes.
- As Al_2O_3 and SiC have similar and fairly isotropic elastic moduli (Table 6.1), and since this simplifies the mathematical expressions significatively, the matrix and reinforcement are assumed to have the same isotropic elastic properties.

As a visual aid, Figure 6.4 shows a schematic of the composite. The platelets have a preferential orientation distribution described by the distribution function $n(\eta)$. If the reference system is attached to the crystallography of the platelet, a platelet with $\eta=0°$ will have different surroundings than a platelet with a different tilt angle e.g. $\eta=45°$. Thus the strain perpendicular to the platelet basal plane, ε_3, will be a function of the same platelet tilt angle, η.

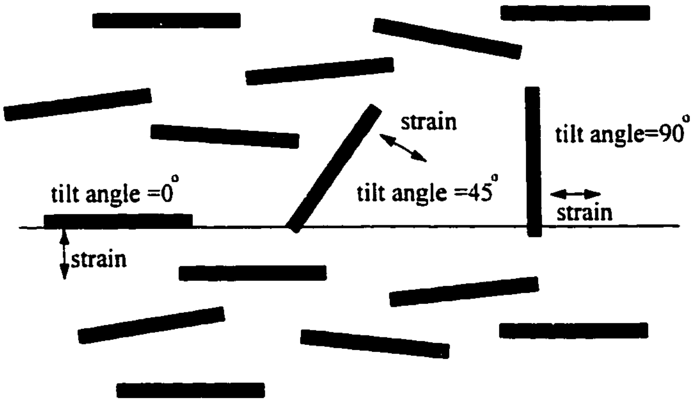

Figure 6.4. Schematic of platelets and the relation between texture and tilt angle. The direction of the strain indicated corresponds to ε_3.

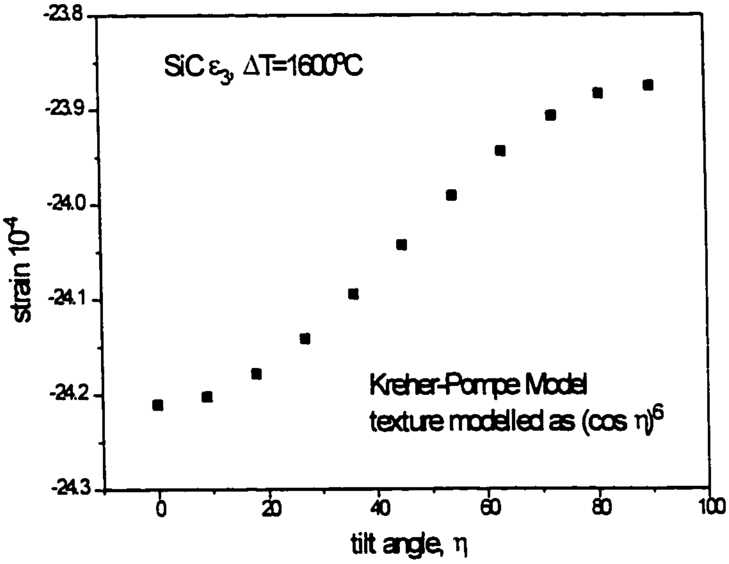

Figure 6.5. Calculated strain (perpendicular to the basal plane) according to Kreher-Pompe model.

The model results for ε_3, assuming $n(\eta)\propto\cos^6(\eta)$ are illustrated on Figure 6.5. The dependency of the internal strain on the tilt angle seems logical. The coefficient of thermal expansion of alumina is larger than the coefficients of silicon carbide. As $\alpha_{3SiC} > \alpha_{1,2SiC}$, when the material is textured, the overall composite would have a larger thermal expansion coefficient in the vertical direction of Figure 6.4 and a smaller one in the horizontal direction. A platelet with $\eta=0$ would have a larger difference of thermal expansion coefficient, with its surroundings, in the direction of a_3 (in this case the vertical direction of Figure 6.4). Thus the absolute value of the strain ε_3 imposed on the platelet would be relatively high. In the same way, a platelet with tilt angle 90° has a smaller difference in thermal expansion coefficient on its a_3 direction (in this case the horizontal direction of Figure 6.4) and thus a smaller absolute value of strain ε_3.

The calculated ε_3 would be equivalent to the (002) strains determined by neutron diffraction of Figure 5.30. However, the calculated and experimental strain values cannot be directly compared. Since the calculated ε_3 values depend on all the aforementioned assumptions. Nevertheless, the tilt angle dependency and general trends provide useful information. The shape of the experimental and model curves are similar. However, the calculated trend for ε_3 is opposite to the experimental data for (002). The lower (absolute) values of the $\varepsilon_{(002)}$ occur at low tilt angles and not at the higher tilt angles, as predicted by the model ε_3. Yet, the model results were easily rationalized taking into account the texture of the composites. Thus, the explanation for the reverse trend in the composites is likely to lie somewhere else. Doing a mental exercise, if a compressive strain of the order of 10^{-3} is added to the composite perpendicular to the HP direction, then the shape of the curve produced by the model changes to the experimental shape, as shown in Figure 6.6.

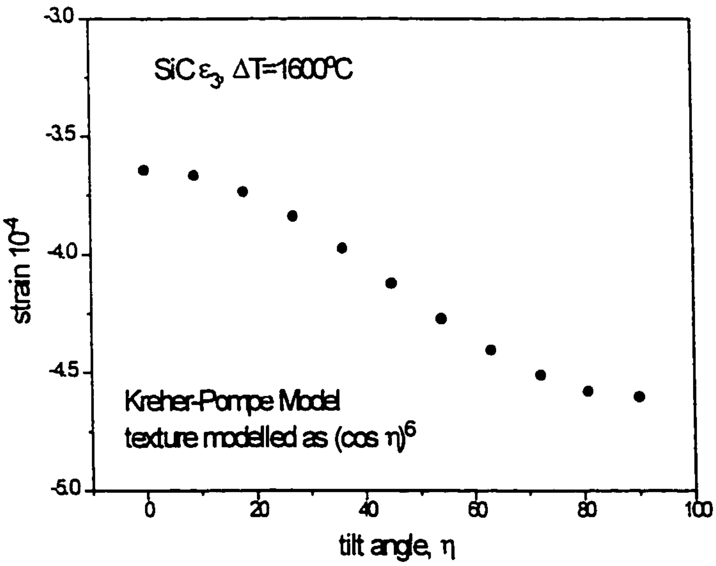

Figure 6.6. Adding a strain perpendicular to the HP direction to the composites changes the model curve to a trend similar to the experimental curve.

Thus the composite must have unaccounted effects whose net result is equivalent to adding a strain perpendicular to the HP direction (horizontal in Figure 6.4). One of the possible sources of strain are the cooling conditions after sintering of the composites. The composites were sintered in a die with load applied through lower and upper rams, Figure 6.7a. After sintering was considered complete, the load was removed and the composite was no longer constrained in the HP direction, Figure 6.7b. The cooling cycle began after removing the load. When cooling down, the sample is still constrained by the graphite die in the horizontal direction (equivalent to $\eta=0°$). The coefficient of thermal expansion of graphite is approximately $\alpha_{g3}=3\times10^{-5}$ (perpendicular to the basal plane) and $\alpha_{g1,2}=1\times10^{-6}$ (parallel to the basal plane). In polycrystalline graphite with no porosity, the coefficient of thermal expansion would be approximately $\alpha_g\approx1\times10^{-5}$. In the case of the composite, $\alpha_c\approx7.5\times10^{-6}$. Thus the graphite die will put the composite under compression when cooling. It is possible to calculate an approximate value of the creep strain while cooling (the calculation is explained in Appendix A). Assuming, as an upper bound, that all the creep strain is accommodated elastically by the platelets while the alumina deforms plastically, the resulting strain is of the order of 10^{-5}. This is two orders of magnitude lower than the necessary strain to obtain a behaviour of ε_3 similar to that of the experimental results.

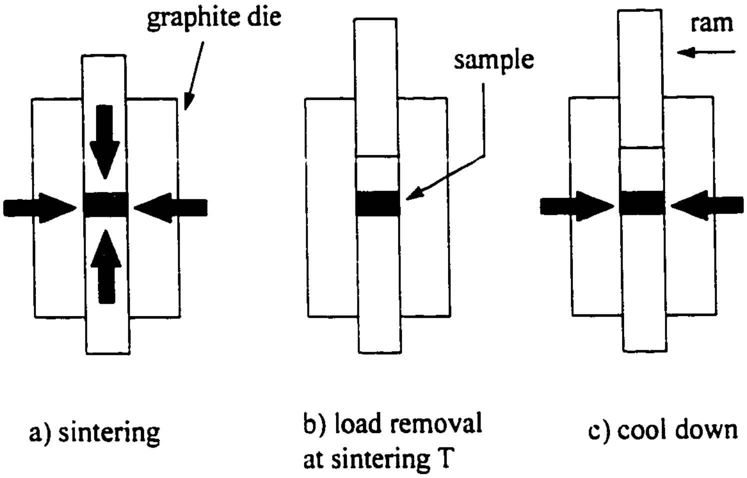

Figure 6.7. Schematic of cooldown after processing.

Another source of inaccuracy is the assumption that all platelets have an aspect ratio λ=10 and consequently, that their tilt angle is independent of the aspect ratio. However, this is not the case: platelets with a large aspect ratio will tend to lie perpendicular to the HP direction and thus have low tilt angles; platelets with low aspect ratio will be more likely to have large tilt angles. Thus Figure 6.4 could be redrawn as Figure 6.8 with the platelet at each tilt angle representing the expected aspect ratio for the given tilt.

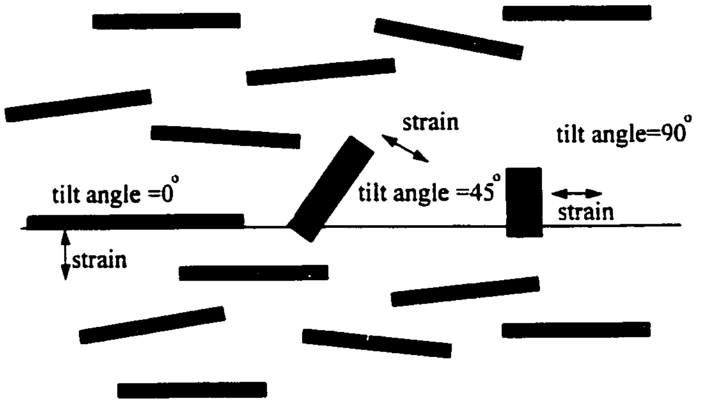

Figure 6.8. Schematic of platelets and the relation between aspect ratio and tilt angle. The direction of the strain indicated corresponds to ε_3.

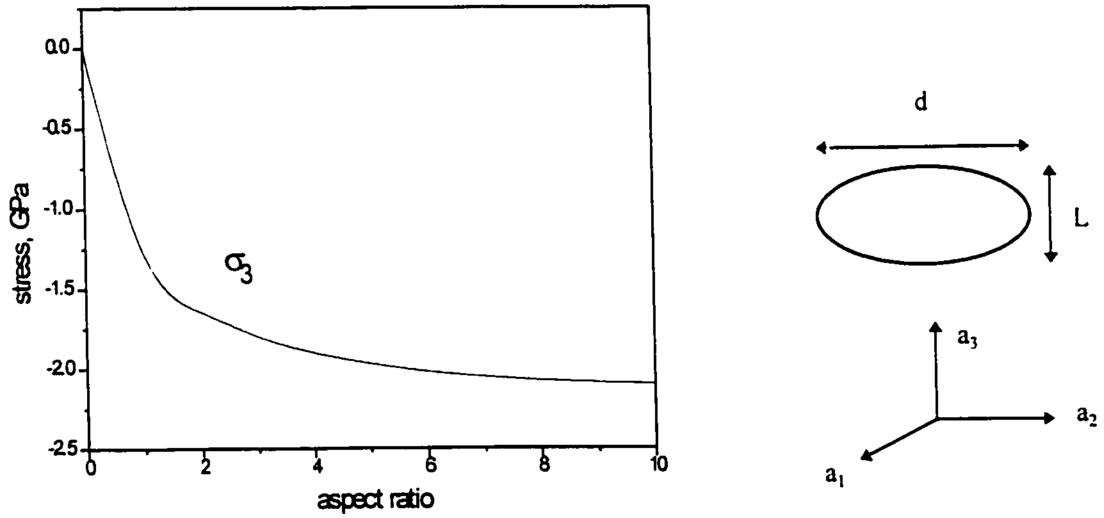

Figure 6.9. Internal stresses within a single SiC inclusion as a function of its aspect ratio L/d in an alumina matrix for ΔT=1000°C (Li and Bradt 1989). N.B. In this graph the aspect ratio is the inverse of the previously defined, i.e. λ=d/L.

The stress in a platelet within a composite will be larger in its longer direction (Li and Bradt 1989, Kreher and Janssen 1992, Pompe and Wilkinson 1993). This is illustrated on the graph of Figure 6.9 where the stress vs aspect ratio of a SiC particle in an alumina matrix has been plotted. If the strain in the particle increases with the stress then, because of the change in average aspect ratio with tilt angle, the average strain ($\varepsilon_{(002)}$):

- in platelets with large tilt angles (average $\lambda<10$) will be larger, and
- in platelets with low tilt angle (average $\lambda>10$) will be lower

than that predicted by the model (Figure 6.5). Thus the model overestimates the strains at low tilt angles and underestimates them at high. It is not possible to estimate the extent of this effect on the measured strains as there is no information available on the dependency of the aspect ratio with tilt angle. However, Figure 6.9 indicates that factors of 2 or 3 could be involved, enough to change the model tilt angle dependency results (Figure 6.5). Hence, to fully explain the experimental results, it would be necessary to incorporate into the model other characteristics of the composite, which affect the spatial distributions of stress and strain, such as the cooling conditions and the particles aspect ratio distribution as a function of the tilt angle.

6.7.3. Influence of annealing and creep on the internal strains.

The internal strains of S30 and Q30 samples were measured in the as-processed, annealed (1250°C, 42h) and crept conditions (1250°C, 1 week). These results are shown in Figure 5.31. The strains are similar in the as-processed, annealed, and ε=5% (Q30) crept material. However, the strains in the ε=16% (S30) deformed material are lower. This is due to the relatively important damage that such a large strain must have been accompanied by. As cavities and cracks were formed, the internal stresses and strains were relieved.

It is interesting that the strains are practically the same in the as-processed, annealed, and 5% crept material. Nevertheless, the hot-pressing of the composites occurred at 1650°C and the annealing and the creep were done at 1250°C. It would not be unreasonable to expect strains proportional to the difference between heat treatment temperature and RT, as the origin of these strains is the thermal expansion mismatch between the phases. However, as mentioned before, cooling from the processing temperature was relatively slow giving the opportunity for significant relaxation to occur. On the other hand, cooling from the annealing or creep temperature was fast, taking a few minutes to cooldown to less than 1000°C. The outcome is that the internal strains in the composites -as processed, annealed, and crept- are associated with a similar change of temperature. It is noteworthy that the calculated $\Delta T=1200°C$ (section 6.7.1) for the as-processed composites, essentially corresponds to the annealing temperature, thus confirming the possible relaxation of strains during cooling from sintering.

After acknowledging the constancy of the strain values in the composites (with the exception of the crept $\varepsilon=16\%$ one), it is remarkable that the SiC diffraction peaks FWHM show clear variations. The full width half maximum (FWHM) of a peak scales with the magnitude of the strain and can give a measure on the distribution of strains (distortion) within a crystal lattice. The more distorted the lattice, the larger the scatter in the diffraction angle and thus the larger the FWHM (Figure 6.10). A strain distribution within a crystal can arise, among other reasons, from the presence of dislocations, voids or by subjecting the crystal to an uneven stress field.

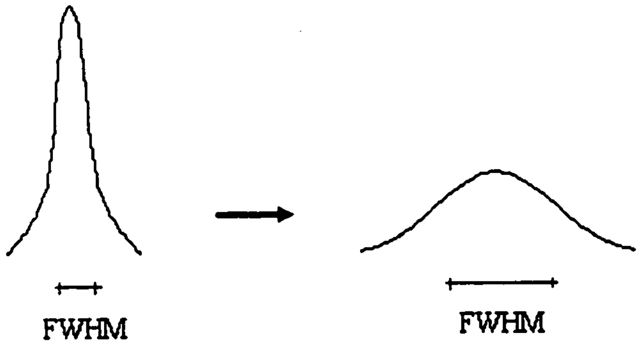

undistorted lattice distorted lattice

Figure 6.10. The distortion of the crystal lattice results in an increase in the FWHM.

The two bottom graphs of Figure 5.31a show the FWHM of the SiC (002) peak as a function of the tilt angle. In the S30 composite, the as-processed FWHM is larger than in the annealed or in the deformed sample ($\varepsilon=16\%$). Also, from Figures 5.30a and 5.30c the same FWHM (SiC (002)) in the as-processed S30 is larger than in the as-processed Q30, T30 and P30 composites. Thus there are strain variations within each platelet in the as-processed S30 composite which are not found in the other Q, T, and P composites. In addition these strain variations seem to decrease with heat treatment. In the case of the Q30 samples, the FWHM remains unchanged in the as-processed, annealed and deformed (ε=5%) conditions. No evidence was found in this composite of a strain variation similar to that of S30. Table 6.3. summarizes these observations.

FWHM (002) SiC	as-processed	annealed	crept
S30	larger	decrease	decrease
Q30	smaller	no change	no change

Table 6.3. Comparison of SiC (002) FWHM, see Figures 5.30 and 5.31.

No evidence of dislocation activity was found in the platelets by electron microscopy techniques (section 5.4) and the platelets phase was found to be stable under heat treatments (section 3.2). In addition, no other composite (Q, T or P) showed a similar dependence of the FWHM on heat treatment. Then the decrease in FWHM of the SiC peak in the S30 composites cannot be attributed to a decrease in dislocation density or to a phase-transition type of transformation. Since the texture and high volume fraction of the reinforcement network in the S30 composite promote platelet-platelet interactions, it is likely that these interactions provoke the bending and distortion of the SiC lattice. These platelet-platelet interactions are less likely to happen in the aligned materials as the angles between platelets tend to be smaller (Figure 6.3). Thus the as-processed aligned materials show no increase in (002) FWHM. It is then possible that the bending strains in the S30 platelet network are relaxed during exposure to high temperatures. Section 6.6 discussed the effects of annealing in the creep behaviour of the S30 composites and the occurrence of a stress relaxation process during annealing was suggested. This relaxation process then likely consists of the lessening of bending strains within the platelets.

The relaxation time of a bent platelet in a viscous matrix can then be calculated based on the Wilkinson-Pompe model for the anelastic creep response of whisker-reinforced ceramics (Wilkinson and Pompe 1997). The detailed calculation is shown in Appendix B. Assuming no interaction between a bent platelet and its neighbours, and using the calculated viscosity for the S30 composite as the viscosity of the surrounding matrix, the approximate relaxation time, τ_r, is:

$$\tau_r = 2.5\text{x}10^4 \text{ s}$$

The experimental time, $t=1.5\times10^5$s, for the slow creep regime onset in the S30 composites is approximately six times the calculated relaxation time. Any interactions between neighbouring platelets will hinder the relaxation process and make it slower, since the model considers an unbending platelet free of interactions, the apparent underestimation of the relaxation time was expected. The agreement between model and experiment supports platelet unbending as a possible relaxation mechanism.

This relaxation process has been found to aid the stress (whether compressive or tensile) in the deformation of the composite (section 6.6). It is possible to imagine a bent platelet whose tilt angle is any but perpendicular or parallel to the applied stress. Then, the elastic energy of the platelet can be used to enhance deformation biased by the stress, schematically shown in Figure 6.11. Obviously the process in the composite is complicated by the platelet-platelet interactions, as it pertains to a network of platelets rather than a single platelet. However, the essence of the phenomenon is the same: the use of stored elastic energy to aid in the deformation of the composite.

This type of stress-biased behaviour has not been observed in whisker-reinforced composites. However, this is not surprising. The relaxation time will generally scale as the inverse of the third power of the diffusion distance: $\tau_r \sim d^{-3}$. The diffusion distance for a whisker will be of the order of its own diameter, i.e. 1μm, for a platelet it will be of the order of 10μm. Thus, the relaxation time for a whisker will be three orders of magnitude smaller than for a platelet. Taking the experimental $\tau_{rp}=1.5\times10^5$s (almost 2 days) for a platelet, then the relaxation time for a whisker in similar conditions will be $\tau_{rw}=2.5$ minutes. In a creep experiment, the relaxation would take place while reaching the testing temperature, certainly before the application of the load.

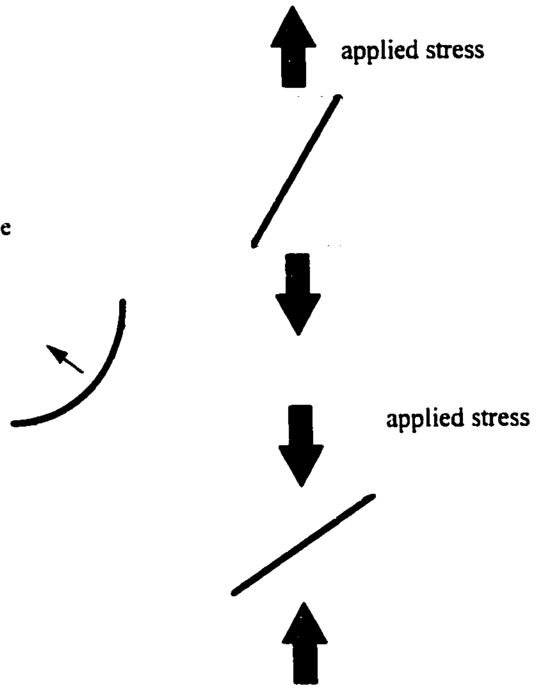

Figure 6.11. The relaxation of bending strains in a platelet can enhance deformation in the direction of the applied stress.

6.8. Summary.

This chapter was divided according to different characteristics of the composites and their effects on the creep properties. The processing of the composites was found to strongly affect their creep behaviour. The larger quantity of impurities, in the tape cast samples, increased the quantity of amorphous phase, facilitated deformation and increased the creep rates. In addition, evidence of cavitation as an important creep deformation mechanism was found. In the case of the slip cast composites, generally lower creep rates and low creep exponents were found ($n<2$), which suggested diffusion as the main creep deformation mechanism.

The addition of SiC platelets to an alumina matrix has two main effects during deformation of the composites: 1) a mechanical influence, which decreases the creep rate, and 2) a non-mechanical effect due to the occurrence of oxidation reactions and the resulting formation and/or growth of an amorphous phase, which increases the creep rate. Based on the Wilkinson-Pompe (1997) model for creep of ceramic composites, an estimation of the platelets non-mechanical effect could be made.

Similarly to SiC-whisker reinforced alumina, the 15% and 30% SiC platelet aligned composites displayed essentially the same creep rates. Suggesting that further additions than 15% platelets have no effect on the creep rates. However, the total strain in the 30% composites was lower than in the 15%. This was rationalized by considering that as the platelet volume fraction increases, the platelet network becomes more rigid

The texture effects in the creep behaviour were best seen when comparing the Q and S or the T and P composites. The creep exponents of the S and Q composites were found to be essentially the same. Yet, the strain rates in Q were higher. Experimental evidence of the occurrence of platelet rotation during creep was presented. The texture results, on crept samples, suggested the platelets in Q30 are freer to rotate. This was attributed to relatively weak platelet-platelet interactions in the aligned material. On the other hand, the strong interactions between platelets in the more random S30 probably accounted for its lower creep rates. However, the more rigid network also predisposed the composite to cavitation at higher loads.

The P30 and T30 composites presented almost exactly the same behaviour in creep even though the texture data indicated an important difference in platelet orientation distribution. However, in P30, the majority of the platelets are in domains forming low angles with each other, suggesting the interaction between platelets and not the angle of the platelets with the far field stress as the important factor in determining the creep resistance. Nevertheless, any effect from the platelet network morphology could have been masked by the propensity to cavitation in these composites.

From the ε vs t S30 creep curves, a transition from a rapid strain rate to a slow strain rate was found. The phenomenon was attributed to the occurrence of an initial process, approximately during the first $1.5\text{x}10^5$s of exposure to high temperatures, which does not depend on the sign of the stress applied, and appears to be strain independent, time dependent, and stress biased. This was associated to a stress relaxation process by a stress free dwell experiment in the S30 composites. Neither the direction nor the magnitudes of the strains or the strain rates during the dwell were comparable in magnitude to the ones in the first rapid strain rate stage of creep. However, the suggested relaxation time of S30 from the stress-free dwell experiment matched with the one required for the onset of the slow creep regime.

The magnitude of the internal strains measured in the as-processed 30% SiC composites could be rationalized using the equation obtained by Pompe and Wilkinson (1993) for internal strains due thermal expansion mismatch. However, the dependency of the internal strains on the tilt angle could not be fully explained. Texture, platelet aspect ratio distribution, and cooling conditions were suggested as possible sources of this strong dependency of the strain on the tilt angle.

In the S30 composite, the as-processed FWHM of the SiC (002) diffraction peak was found to be larger than in the annealed (S30), crept (S30), or aligned samples. The decrease in FWHM of the SiC peak in the S30 composites with heat treatment was attributed to platelet-platelet interactions, provoking the bending and distortion of the SiC lattice. The platelet bending in the aligned materials was suggested as not being significant since the platelet-platelet interactions tend to be weaker. The approximate relaxation time of a bent platelet in a viscous matrix was calculated based on the Wilkinson-Pompe (1997) model for the anelastic creep response of whisker-reinforced ceramics. The calculated relaxation time was in agreement with the experimental time for the slow creep regime onset.

Finally, the unbending of platelets in the S30 composite was proposed as a viable relaxation mechanism. This hypothesis was strongly supported by the neutron diffraction measurements of the FWHM, the model calculations for the relaxation time which coincide with the time of slow creep onset, and the possibility of using the platelets elastic energy to enhance deformation biased by the stress.

7. SUMMARY AND CONCLUSIONS.

The objective of this work was to fabricate SiC-platelet reinforced alumina composites with different network morphologies and to study their creep behaviour. In order to obtain distinct platelet network morphologies, different colloidal processing techniques were used. The approaches involved tape casting using organic solvents or slip casting using aqueous solvent. The following volume fraction composites were fabricated: *0 vol%* as a reference material, *5 vol%* -a low volume fraction where interactions between platelets were expected to be minimal, *15 vol%* where platelet-platelet interactions were likely to happen, and *30 vol%* for which strong interaction between reinforcement particles were expected. All samples were hot-pressed so as to have the same average matrix grain size and near-full density. The experimental techniques used to characterise the samples include optical and electron microscopy, densitometry, flexure and compression creep testing, dimensional measurements during heat treatment, and neutron diffraction.

The creep behaviour of the composites varied greatly with their impurity content. Larger quantities of impurities, in the tape cast samples, increased the quantity of amorphous phase at the SiC/Al_2O_3 interfaces, facilitating deformation. As a result, the composites showed increased creep rates and large creep exponents ($n>2$) associated with cavitation processes. In the case of the slip cast composites, generally lower creep rates and low creep exponents were found ($n<2$). In these composites, diffusion was suggested as the main creep deformation mechanism.

The addition of SiC platelets to an alumina matrix was shown to have two main effects during deformation of the composites: 1) a mechanical influence, which decreased the creep rate, and 2) a non-mechanical effect due to the occurrence of oxidation reactions and the resulting formation and/or growth of an amorphous phase, which increased the creep rate. In order to properly asses the mechanical influence of platelets additions it was necessary to estimate the properties of the composite matrix material. Thus, rather than using the characteristics of the monolithic alumina as those of the composites matrix, a better alternative was to use the characteristics of a matrix alumina which included the non-mechanical effect due to platelet additions.

Similarly to SiC-whisker reinforced alumina, the 15% and 30% SiC platelet aligned composites displayed essentially the same creep rates, suggesting that further additions than 15% platelets have no effect on the creep rates. However, the total strain in the 30% composites was lower than in the 15%. This was rationalised by considering that as the platelet volume fraction increases, the platelet network becomes more rigid

The texture effects in the creep behaviour were best seen when comparing the Q and S (slip cast) or the T and P (tape cast) composites. The creep exponents of the S and Q composites were found to be essentially the same. Yet, the strain rates in Q (more aligned material) were higher. Experimental evidence of the occurrence of platelet rotation during creep was presented. The texture results, on crept samples, suggested the platelets in Q30 as freer to rotate. This was attributed to relatively weak platelet-platelet interactions in the aligned material. On the other hand, the strong interactions between platelets in the more random S30 probably accounted for its lower creep rates. However, it was found that a more rigid network also predisposed the composite to cavitation. The tape cast P30 and T30 composites presented almost exactly the same behaviour in creep even though the texture data indicated an important difference in platelet orientation distribution. This suggested that the ability of interaction between platelets and not the angle of the platelets with the far field stress as the important factor in determining the creep resistance. In addition, the rotation, translation, and sliding (past each other) of platelets were suggested as possible creep deformation mechanisms.

The magnitude of the internal strains measured in the as-processed 30% SiC composites could be rationalised using the model of Pompe and Wilkinson (1993) for internal strains due to thermal expansion mismatch. However, the dependency of the internal strains on the tilt angle could not be fully explained. The importance of texture, platelet aspect ratio distribution, and platelet-platelet interactions were suggested as the main possible sources of the strong dependency of the strain on the tilt angle.

A transition from a rapid creep strain rate to a slow strain rate was found only in the S30 composites. From various experiments, the phenomenon was attributed to the occurrence of a relaxation process, approximately during the first $1.5x10^5$s of exposure to high temperatures, which does not depend on the stress applied, and appears to be strain independent, time dependent, and stress biased. Moreover, in the S30 composite, the as-processed FWHM of the SiC (002) diffraction peak was found to be larger than in the annealed (S30), crept (S30), or aligned samples. The decrease in FWHM of the SiC peak in the S30 composites with heat treatment was attributed to platelet-platelet interactions, provoking the bending and distortion of the SiC lattice. The platelet bending in the aligned materials was suggested as not being significant since the platelet-platelet interactions tend to be weaker. The approximate relaxation time of a bent platelet in a viscous matrix was calculated based on the Wilkinson-Pompe (1997) model for the anelastic creep response of whisker-reinforced ceramics. The calculated relaxation time was in agreement with the experimental time for the slow creep regime onset. Based on the experimental evidence, the model calculations, and the possibility of using elastic energy of the platelets to enhance deformation biased by the stress, the unbending of platelets in the S30 composite was proposed as a viable relaxation mechanism.

The platelet composites achieved none or modest reductions in creep rates as compared to the monolith. However, this should not detract from the implications of the information acquired.

-The impurity content and the associated glass formation can determine the creep properties of SiC-platelet/Al_2O_3 composites. Thus characteristics of the reinforcement/matrix interface are of significant importance at high temperatures. If the creep resistance of Si_3N_4 has increased by five orders of magnitude through tailoring of the grain boundaries (Wiederhorn et al. 1994), similar approaches can be taken to improve the lifetime of alumina/SiC composites.

-Future work on platelet reinforced ceramics should include the properties of the interface and the longer diffusion paths imposed by the platelets. The use of coatings to inhibit SiC oxidation should be considered as a strong possibility to enhance creep properties.

-Texture, particle shape, and interparticle interactions play a very important role in the determination of the internal strains in two-phase materials. Models based on homogeneous materials should be carefully applied to anisotropic composites.

-Experimental evidence of a strong dependency of the creep behaviour on the morphology of reinforcing particle networks of ceramic/ceramic composites was found.

-Platelet-reinforced composites do not benefit from the elastic loading of the particle network during creep deformation.

-Not only their high aspect ratio but the low stiffness of whiskers, as compared with platelets, might play a very important role in their ability to form elastically deforming networks and thus inhibit creep deformation.

APPENDIX.

APPENDIX A. Estimate of stress build-up due die wall constraint while cooling.

Assume that hot pressing occurs at the temperature $T=T_o$, following which the load is removed and cooling occurs at a rate $dT/dt=\dot{T}$, the composite and graphite die have coefficients of thermal expansion α_c and α_g, respectively. Assuming that the composite is stress free at time $t=0$ and $T=T_o$ and that the graphite die is rigid (which gives an upper bound solution), then the imposed excess strain on the composite by the die is,

$$\varepsilon^{xs} = \varepsilon_g - \varepsilon_c = \Delta\alpha\, \dot{T}\, \Delta t \quad \text{(compressive)}$$

Assuming the composite obeys the constitutive law:

$$\dot{\varepsilon} = \dot{\varepsilon}_0 \exp\left(-\frac{Q}{RT}\right)\left(\frac{\sigma}{\sigma_0}\right)^n \qquad \text{(A1)}$$

where $\dot{\varepsilon}_0$, n and Q can be obtained from creep data and σ_o=1MPa is assumed.

For the case of isothermal relaxation, a constant excess strain ε^{xs} is imposed and the fixed displacement is initially elastic:

$$\varepsilon^{xs} = \varepsilon^{el} = \frac{\sigma}{E} \qquad \text{at } t=0 \qquad \text{(A2)}$$

creep occurs with time,

$$\varepsilon^{xs} = \varepsilon^{el} + \varepsilon^{cr} \qquad \text{at } t\neq 0 \qquad \text{(A3)}$$

$$\dot{\varepsilon}^{el} + \dot{\varepsilon}^{cr} = 0 \qquad \text{(A4)}$$

$$\frac{\dot{\sigma}}{E} + \dot{\varepsilon}_0 \exp\left(-\frac{Q}{RT}\right)\left(\frac{\sigma}{\sigma_0}\right)^n = 0 \qquad \text{(A5)}$$

Integrating,

$$\frac{d\sigma}{\sigma^{n}} = -E\frac{\dot{\varepsilon}_{o}}{\sigma_{o}}\exp\left(-\frac{Q}{RT}\right)dt \qquad \text{(A6)}$$

or

$$-\frac{1}{n+1}\frac{1}{\sigma^{n+1}}\bigg|_{\sigma(t=0)}^{\sigma} = -E\frac{\dot{\varepsilon}_{o}}{\sigma_{o}^{n}}\exp\left(-\frac{Q}{RT}\right)t \qquad \text{(A7)}$$

Thus

$$\left(\frac{\sigma_{o}}{\sigma}\right)^{n+1} - \left(\frac{\sigma_{o}}{E\varepsilon^{xs}}\right)^{n+1} = (n+1)\frac{E\dot{\varepsilon}_{o}}{\sigma_{o}}\exp\left(-\frac{Q}{RT}\right)t \qquad \text{(A8)}$$

We can use a similar approach for when the excess strain is a function of temperature,

$$\varepsilon^{xs} = f(T) \qquad \text{(A9)}$$

Then, in the time interval Δt there is a change in excess strain and in creep strain given by:

$$\Delta\varepsilon^{xs} = \Delta\alpha\cdot\dot{T}\,\Delta t \qquad \text{(A10)}$$

and

$$\Delta\varepsilon^{cr} = \dot{\varepsilon}_{o}\exp\left(-\frac{Q}{RT}\right)\left(\frac{\sigma}{\sigma_{o}}\right)^{n}\Delta t \qquad \text{(A11)}$$

Moreover,

$$\Delta\varepsilon^{xs} = \Delta\varepsilon^{el} + \Delta\varepsilon^{cr} \qquad \text{(A12)}$$

or

$$\dot{\varepsilon}^{xs} = \dot{\varepsilon}^{el} + \dot{\varepsilon}^{cr} \qquad \text{(A13)}$$

From (A10),

$$\Delta\alpha\,\dot{T} = \frac{\dot{\sigma}}{E} + \dot{\varepsilon}_{o}\exp\left(-\frac{Q}{RT}\right)\left(\frac{\sigma}{\sigma_{o}}\right)^{n} \qquad \text{(A14)}$$

Similarly for ε^{cr},

$$\Delta\varepsilon^{cr} = \dot{\varepsilon}_{o}\exp\left(-\frac{Q}{RT}\right)\left(\frac{\sigma}{\sigma_{o}}\right)^{n} \qquad \text{(A15)}$$

We assume that,

$$\alpha_{c} = (1-\phi)\,\alpha_{matrix} + \phi\,\alpha_{platelet} \qquad \text{(A16)}$$

$$E_c = (1-\phi)\, E_{matrix} + \phi\, E_{platelet} \qquad \text{(A17)}$$

where ϕ is the platelets volume fraction and E is the Young's modulus.

Taking the creep activation energy Q=585 kJ/mol from measurements on SiC whisker-reinforced ceramics (Arellano-Lopez et al. 1993), the cooling rate as the numerical derivative of the T vs t curve of Figure 3.14, the creep exponent n=1.1 from creep data on the S30 composite, then equations (A14) and (A15) can be evaluated numerically.

Thus the creep strain in the composite due to the die wall constraint is approximately:

$$\varepsilon^{cr} \approx 9\mathrm{x}10^{-6}$$

APPENDIX B. Calculation of the relaxation time for a platelet in a viscous matrix.

The calculation is based on the Wilkinson-Pompe (Wilkinson and Pompe 1997) model for creep and anelastic recovery of whisker- and platelet- reinforced ceramics. The geometry of a platelet is modeled as indicated in Figure B.1.

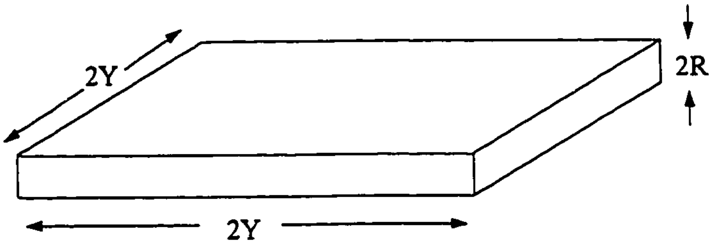

Figure B.1. Assumed platelet geometry.

Assuming the platelet is symmetrically bent, the distance between the platelet and a reference plane is u as shown on Figure B.2.

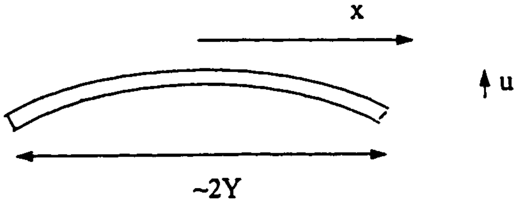

Figure B.2. Schematic of bent platelet.

For a beam embedded in a viscous matrix momentum equilibrium gives (Wilkinson and Pompe 1997):

$$EI\frac{\partial^4 u(x,t)}{\partial x^4} = -2\eta\frac{\partial u(x,t)}{\partial t} \qquad \text{(B1)}$$

where E is the platelet Young Modulus at the relaxation temperature, I=4/3 (R^3Y) and η is the viscosity of the surrounding material.

Let A=EI and B= -2η then,

$$A\frac{\partial^4 u(x,t)}{\partial x^4} = B\frac{\partial u(x,t)}{\partial t} \qquad \text{(B2)}$$

Assuming,

$$u(x,t)=u_x(x)u_t(t) \qquad \text{(B3)}$$

and the boundary conditions, for any t:

$$\frac{du_x}{dx} = 0, \quad \text{at } x = 0 \qquad \text{(B4)}$$

$$u_x = 0, \quad \text{at}\begin{cases} x = \frac{Y}{2} \\ x = -\frac{Y}{2} \end{cases} \qquad \text{(B5)}$$

From B3,

$$\frac{1}{u_x}\frac{d^4 u_x}{dx^4} = \frac{B}{A}\frac{1}{u_t}\frac{du_t}{dt} = K_1 \qquad \text{(B6)}$$

where K_1 is a constant. Solving the temporal part,

$$\frac{du_t}{u_t} = \frac{A}{B}K_1\,dt \qquad \text{(B7)}$$

we get

$$u_t = K_2 \exp\left(\frac{A}{B}K_1 t\right) \qquad \text{(B8)}$$

Solving the spatial part,

$$\frac{d^4 u_x}{dx^4} = K_1 u_x \qquad \text{(B9)}$$

the solution is of the form,

$$u_x = K_3 \cos(K_4 x) + K_5 \qquad \text{(B10)}$$

Substituting B10 into B9,

$$K_3 K_4^4 \cos(K_4 x) = K_1(K_3 \cos(K_4 x) + K_5) \qquad \text{(B11)}$$

Therefore, $K_5=0$ and $K_4^4=K_1$. From the boundary conditions,

$$K_4 = \frac{\pi}{Y} \text{ and } K_1 = \left(\frac{\pi}{Y}\right)^4 \qquad \text{(B12)}$$

Then, the relaxation time is given by:

$$\tau_r = \frac{2\eta Y^4}{EI\pi^4} = \frac{3}{2}\frac{\eta Y^3}{\pi^4 ER^3} = \frac{3\eta\lambda^3}{2\pi^4 E} \qquad \text{(B13)}$$

where $\lambda \cong 10$ is the platelet aspect ratio, extrapolating E for a temperature of 1250°C from the data of Li and Bradt (1988) for E of hexagonal SiC at 1000°C, $E_{1250} \cong 380$GPa. Considering the viscosity of the matrix as that of the calculated glass-bonded alumina, $\eta_{GB} \cong 6\text{x}10^8$ MPa s, the calculated relaxation time is:

$$\tau_r = 2.5\text{x}10^4 \text{ s.}$$

BIBLIOGRAPHY

Alexander, K.B., Angelini, P., Becher, P.F., 1990. Mat.Res.Soc.Symp.Proc., 183, 273-278

Arellano-Lopez, A.R., Cumbrera, F.L., Dominguez-Rodriguez, A., Goretta, K.C., Routbort, J.L., 1990, J.Am.Ceram.Soc., 73, 5, 1297-1300

Arellano-Lopez, A.R., Dominguez-Rodriguez, A., Goretta, K.C., Routbort, J.L., 1993, J.Am.Ceram.Soc., 76, 6, 1425-1432

Bacon, G.E., 1975, Neutron Diffraction, Oxford University Press, London

Baril, D., Jain, M.K., 1991, Ceram.Eng.Sci.Proc., 12, 1175-1192

Becher, P.F., Angelini, P., Warwick, W.H., Tiegs, T.N., 1990, J.Am.Ceram.Soc., 73, 1, 91-96

Becher, P.F., Tiegs, T.N., 1988, Adv.Cer.Mat., 3, 2, 148-153

Becher, P.F., Wei, G.C., 1984, J.Am.Ceram.Soc., 67, 12, C267-C269

Birchall, J.D., Stanley, D.R., Mockford, M.J., Pigott, G.H., Pinto, G.J., 1988, J.Mater.Sci.L., 7, 350-352

Bloyce, D., 1993, Tape Casting and Mechanical Properties of SiC Platelet Reinforced Alumina, Master of Engineering, McMaster University, Hamilton, ON, Canada

Boch, P., Chartier, T., Huttepain, M., 1986, J.Am.Ceram.Soc., 69, 8, c191-c192

Burger, G., Lemay, R., Lloyd, D.J., Shaw, T., Apte, P.S., 1990, Microstructure-Mechanical Property Relations in Al2O3 Laminates, Proceedings of the 11th Riso International Symposium, Structural Ceramic Processing, Microstructure and Properties, eds., Riso National Laboratory, Roskilde, Denmark, 217-224

Cannon, R.M., Langdon, T.G., 1983, J.Mater.Sci., 18, 1-50

Carroll, D.F., Wiederhorn, S.M., Roberts, D.E., 1989, J.Am.Ceram.Soc., 72, 9, 1610-1614

Chartier, T., Besson, J.L., Boch, P., 1988, Mechanical Properties of ZrO2-Al2O3 Laminated Composites, Science and Technology of Zirconia III, eds., American Ceramic Society, Westerville, OH, 1131-1138

Chokshi, A.H., Porter, J.R., 1985, J.Am.Ceram.Soc., 68, 6, c144-c145

Chokshi, A.H., Porter, J.R., 1986, J.Mater.Sci., 21, 705-710

Chou, Y.S., Green, D.J., 1992, J.Am.Ceram.Soc., 75, 12, 3346-3352

Chou, Y.S., Green, D.J., 1993, J.Am.Ceram.Soc., 76, 6, 1452-1458

Chowdhury, K.D., Carpenter, R.W., Braue, W., Liu, J., Ma, H., 1995, J.Am.Ceram.Soc., 78, 10, 2579-2592

Chuang, T.J., 1986, J.Mater.Sci., 21, 165-175

Claussen, N., 1990, Ceramic Platelet Composites, Structural Ceramics- Processing, Microstructure and Properties, eds., Riso National Laboratory, Roskilde, Denmark, 1-12

Dayton, G.O., Shulze, W.A., Shrout, T.A., Swartz, S., Biggers, J.V., 1984, Fabrication of Electromechanical Transducer Materials by Tape Casting, Advances in Ceramics, eds., American Ceramic Society, Ohio, 115-139

De Portu, G., Fiori, C., Sbaizero, 1988, Fabrication, Microstructure and Properties of ZrO2-Toughened Al2O3 Substrates, Science and Technology of Zirconia III, eds., American Ceramic Society, Westeville, OH, 1063-1073

Derjaguin, B.V., Landau, L.D., 1941, Acta Physicochim, 14, 633-652

Donaldson, K.Y., Venkateswaran, A., Hasselman, D.P.H., 1989, Ceram.Eng.Sci.Proc., 10, 1191-1211

Ettre, K., Castles, G.R., 1972, Am.Ceram.Soc.Bull., 51, 3, 482-485

Everett, D.H., 1989, Basic Principles of Colloid Science, Royal Society of Chemistry Burlington House, London

Gharghouri, M., 1997, Study of the Mechanical Properties of Mg-8.5wt%Al by In-Situ Neutron Diffraction, Ph.D., McMaster University, Hamilton, ON

Grathwol, G., 1988, Mechanical testing of Engineering Ceramics at High Temperatures, eds., Elsevier Applied Science, London, 31-50

Gu, W., Porter, J.R., Langdon, T.G., 1994, J.Am.Ceram.Soc., 77, 6, 1679-1681

Hamaker, H.C., 1937, Phys.IV, 10, 1058-1072

Hiemenz, P.C., 1977, Principles of Colloid and surface Chemistry, Marcel Dekker, Inc., New York

Hollenberg, G.W., Terwilliger, G.R., Gordon, R.S., 1971, J.Am.Ceram.Soc., 54, 4, 196-199

Horn, R.G., 1990, J.Am.Ceram.Soc., 73, 5, 1117-1135

Huang, X.N., Nicholson, P.S., 1993, J.Am.Ceram.Soc., 76, 5, 1294-1301

Israelachvili, 1992, Intermolecular and Surface Forces, Academic Press, San Diego, CA

Jakus, K., Nair, S., 1990, Comp.Sc.Tech., 37, 279-297

Jakus, K., Wiederhorn, S.M., Hockey, B.J., 1986, J.Am.Ceram.Soc., 69, 10, 725-731

Janssen, R., Heussner, K.H., 1991, Powder Met.Int., 23, 241-245

Kingery, W.D., Bowen, H.K., Uhlmann, D.R., 1976, Introduction to Ceramics, John Wiley & Sons, USA

Knippenburg, W.F., 1963, Philips Res.Rept., 18, 161-274

Kreher, W., 1990, J.Mech.Phys.Solids, 38, 1, 115-118

Kreher, W., 1996, Internal Report MPG/DD1/961030

Kreher, W., Molinari, A., 1993, J.Mech.Phys.Solids, 41, 12, 1955-1977

Kreher, W., Pompe, W., 1989, Internal Stresses in Heterogeneous Solids, Akademie Verlag, Berlin

Lange, F.F., 1987, J.Mat.Res., 2, 1, 59-65

Lange, F.F., 1989, J.Am.Ceram.Soc., 72, 1, 3-15

Li, Z., Bradt, R.C., 1989, J.Am.Ceram.Soc., 72, 1, 70-77

Lin, F., Marieb, T., Nutt, S., 1988, Thermal Oxidation of Al2O3-SiC whisker Composites:Mechanisms and Kinetics, High Temperature/High Performance Composites, eds., Materails Research Society, Pittsburgh, Pennsylvania, 323-332

Lin, H.T., Alexander, K.B., Becher, P.F., 1996, J.Am.Ceram.Soc., 79, 6, 1530-1536

Lin, H.T., Becher, P.F., 1990, J.Am.Ceram.Soc., 73, 5, 1378-1381

Lin, H.T., Becher, P.F., 1991, J.Am.Ceram.Soc., 74, 8, 1886-1893

Lipetzky, P., Nutt, S.R., Becher, P.F., 1988, Creep Behavior of an Al2O3-SiC Composite, Materials Research Society Symposium Proceedings, eds., Materials Research Society, Pittsburgh, Pennsylvania, 271-277

Lipetzky, P., Nutt, S.R., Koester, D.A., Davis, R.F., 1991, J.Am.Ceram.Soc., 74, 6, 1240-1247

Liu, D.S., Parvizi-Majidi, A., 1990, Ceram.Eng.Sci.Proc., 11, 745-753

Liu, J., Ownby, P.D., Weaver, S.C., 1992, Ceram.Eng.Sci.Proc., 13, 696-703

Luthra, K.L., Park, H.D., 1988, General Electric Research and Development Technical Report, 88CRD262, 26

Luthra, K.L., Park, H.D., 1990, J.Am.Ceram.Soc., 73, 4, 1014-1023

Macdowell, J.F., Beall, G.H., 1969, J.Am.Ceram.Soc., 52, 1, 17-25

MacKinnon, R.J., Blum, J.B., 1984, Particle Size Distribution Effects on Tape Casting Barium Titanate, Advances in Ceramics, Forming of Ceramics, eds., The American Ceramic Society, Ohio, 150-157

Malghan, S.G., Pei, P., Wang, P.S., 1991, Ceram.Eng.Sci.Proc., 12, 2115-2123

Mendelson, M.I., 1969, J.Am.Ceram.Soc., 52, 8, 443-446

Mistler, R.E., Shanefield, D.J., Runk, R.B., 1978, Tape Casting of Ceramics, Ceramic Processing Before Firing, eds., Wiley-Interscience, New York, 411-448

Mistler.RE, 1990, Am.Ceram.Soc.Bull., 69, 6, 1022-1026

Mitchell, T.J., De Jonghe, L.C., MoberlyChan, W.J., Ritchie, R., 1995, J.Am.Ceram.Soc., 78, 1, 97-103

Munson-McGee, S.H., 1991, Phys.Rev.B, 43, 4, 3331-3336

Nischik, C., Seibold, M.M., Travitzky, N.A., Claussen, N., 1991, J.Am.Ceram.Soc., 74, 2464-2468

Nutt, S.R., 1984, J.Am.Ceram.Soc., 67, 6, 428-431

Nutt, S., 1988, J.Am.Ceram.Soc., 71, 3, 149-156

Nutt, S.R., Lipetzky, P., Becher, P.F., 1990, Mater.Sci.Eng., A126, 165-172

Pan, Y., Baptista, J.L., 1996, J.Am.Ceram.Soc., 79, 8, 2017-2026

Park, C.H., Cheong, B.H., Lee, K.H., Chang, K.J., 1994, Phys.Rev.B, 49, 7, 4485-4493

Pashley, R.M., Israelachvili, J.N., 1984, J.Colloid Interface Sci., 101, 511-523

Passmore, E.M., Duff, R.H., Vaslos, T., 1966, J.Am.Ceram.Soc., 49, 11, 594-600

Ploehn, H.J., Russel, W.B., 1990, Adv.Chem.Eng., 15, 137-228

Plucknett, K.P., Caceres, C.H., Hughes, C., Wilkinson, D.S., 1994, J.Am.Ceram.Soc., 77, 8, 2145-2153

Plucknett, K.P., Caceres, C.H., Wilkinson, D.S., 1994, J.Am.Ceram.Soc., 77, 8, 2137-2144

Pompe, W., Wilkinson, D.S., 1993, Journal de Physique IV, 3, 1889-1894

Porter, J.R., 1988, Proceedings of an International Conference, Whisker- and Fiber-Toughened Ceramics, ASM, 147-152

Porter, J.R., 1989, Mater.Sci.Eng., A107, 127-132

Porter, J.R., Chokshi, A.H., 1987, Creep Performance of Silicon Carbide whisker-Reinforced Alumina, Ceramic Microstructures '86, Role of Interfaces, eds., Plenum Press, New York, 919-928

Porter, J.R., Lange, F.F., Chokshi, A.H., 1987, J.Am.Ceram.Soc., 66, 2, 343-347

Reed, J.S., 1988, Introduction to the Principles of Ceramic Processing, John Wiley & Sons, Inc., New York, USA

Ring, T.A., 1987, A Model of Tape Casting Bingham Plastic and Newtonian Fluids, Ceramic Substrates and Packages for Electronic Applications, eds., The American Ceramic Society, Ohio, 569-576

Roosen, A., 1988, Basic Requirements for Tape Casting of Ceramic Powders, Ceramic Powder Science II, eds., American Ceramic Society, Westerville, Ohio, 675-692

Routbort, J.L., Goretta, K.C., Dominguez-Rodriguez, A., Arellano-Lopez, A.R., 1990, J.Hard Mat., 1, 4, 221-232

Sacks, M.D., Khadilkar, C.S., Scheiffele, G.W., Shenoy, A.V., Dow, J.H., Sheu, R.S., 1987, Dispersion and Rheology in Ceramics Processing, Advances in Ceramics, eds., The American Ceramic Society, Ohio, 495-515

Sacks, M.D., Lee, H.W., Rojas, O.E., 1988a, J.Am.Ceram.Soc., 71, 5, 370-379

Sacks, M.D., Lee, H.W., Rojas, O.E., 1988b, Mat.Res.Soc.Symp.Proc., 120, 175-184

Sandlin, M.S., Bowman, K.J., Root, J., 1997, Acta Mater., 45, 1, 383-396

Scheiffele, G.M., Sacks, M.D., 1988, Pyrolysis of Poly(vinyl butyral) Binders: II, Effects of Processing Varaibles, Ceramic POwder Science II, eds., American Ceramic Society, Westerville, Ohio, 559-566

Scherm, R., Fak, B., 1993, Neutrons, Neutron and Synchrotron Radiation for Condensed Matter Studies, eds., Springer-Verlag, New York, 113-143

Selçuk, A., Leach, C., Rawlings, R.D., 1995, J.Eur.Ceram.Soc., 15, 33-43

Shames, I.H., 1982, Mechanics of Fluids, McGraw-Hill, New York

Shanefield, D.J., 1986, Competing Adsorptions in Tape Casting, Multilayer Ceramic Devices, Advances in Ceramics, eds., American Ceramic Society, Westerville, Ohio, 155-160

Shanefield, D.J., Mistler, R.E., 1974, Am.Ceram.Soc.Bull., 53, 5, 416-420

Smith, S.M., Scattergood, R.O., Singh, J.P., Karasek, K., 1989, J.Am.Ceram.Soc., 72, 7, 1252-1255

Swan, A.H., Swain, M.V., Dunlop, G.L., 1992, J.Eur.Ceram.Soc., 10, 317-326

Tiegs, T.N., Becher, P.F., 1987, J.Am.Ceram.Soc., 70, 5, c109-c111

Todd, R.I., 1995, Brit.Ceram.Proc., 55, 225-238

Tuffe, S., Ham-Su, R., Bloyce, D.M., Plucknett, K.P., Wilkinson, D.S., 1993, Tape Casting of Platelet Reinforced Ceramics, Developments and Applications of Ceramics and New Metal Alloys, eds., Canadian Institute of Mining, Metallurgy and Petroleoum, Montreal, 377-386

Velamakanni, B.V., Chang, J.C., Lange, F.F., Pearson, D.S., 1990, Langmuir, 6, 1323-1325

Verwey, E.J.W., Overbeek, J.T.G., 1948, Theory of Stability of Lyophobic Colloids, Elsevier, Amsterdam, Netherlands

Watanabe, H., Kimura, T., Yamaguchi, T., 1989, J.Am.Ceram.Soc., 72, 2, 289-293

Wereszczak, A.A., Parvizi-Majidi, A., More, K.L., Frber, M.K., 1993, J.Am.Ceram.Soc., 76, 2, 2397-2400

Wiederhorn, S.M., Luecke, W.E., Hockey, B.J., Long, G.G., 1994, Creep Damage Mechanisms in Si3N4, Tailoring of Mechanical Properties of Si3N4 Ceramics, eds., Kluwer Academic Publishers, Boston, 305-326

Wilkinson, D.S., 1994, Creep Mechanisms in Silicon Nitride Ceramics, Tailoring of Mechanical Properties of Si3N4 Ceramics, eds., Kluwer Academic Publishers, Boston, 327-338

Wilkinson, D.S., 1997, J.Am.Ceram.Soc., to be published.

Wilkinson, D.S., Pompe, W., 1997, Acta Metall.Mater., to be published.

Williams, J.C., 1976, Doctor-Blade Process, Treatise of Materials Science and Technology, ed., Academic Press, New York, 173-198

Xia, K., Langdon, T.G., 1988, Microstruct. Sci., 16, 85-96

Zheng, X.Y., Zeng, F.P., Pomeroy, M.J., Hampshire, S., 1990, Brit.Ceram.Proc., 45, 187-198